DISSERTATION

Measurement and Analysis
of identified hadron production at LEP 2
and comparision with QCD predictions

ausgeführt zum Zwecke der Erlangung des akademischen Grades
eines Doktors der technischen Wissenschaften unter der Leitung von

Univ. Prof. Dr. Meinhard Regler
Institut für Kernphysik

eingereicht an der Technischen Universität Wien
Technisch Naturwissenschaftliche Fakultät

von

Dipl. Ing. Niko Neufeld

Matr. Nr. 9026783
Lederergasse 25/2
1080 Wien

Wien, am 12. August 1999

Zusammenfassung

Diese Dissertation behandelt Messungen der Produktionseigenschaften von geladenen Pionen, Kaonen, Protonen und Antiprotonen (symbolisch $\pi^{\pm}$. $\mathrm{K}^{\pm}$, und $\mathrm{p}(\overline{\mathrm{p}})$) unter Benutzung von Daten des DELPHI Experiments (DEtector with Lepton, Photon and Hadron Identification) am LEP Beschleuniger (Large Electron Positron collider). Die verwendeten Daten wurden von DELPHI in der sogenannten LEP 2 Phase aufgezeichnet, während der höhere Schwerpunktsenergien erforscht wurden.

Der erste Schritt nach dem Z^0-Pol war die Schwerpunktsenergie von 130 GeV die dann in den darauf folgenden Jahren schrittweise bis auf 189 GeV (1998) erhöht wurde. Alle diese Hochenergiedaten, eingeschlossen die bei 189 GeV gemessenen, wurden für die vorliegende Arbeit verwendet, für die zum ersten Mal diese Art von Messungen bei den höchsten verfügbaren Energien in $\mathrm{e}^+\mathrm{e}^-$ Beschleunigern durchgeführt wurde.

Im ersten Kapitel wird versucht, eine kurze phänomenologische Motivation für das Interesse an den vorliegenden Messungen zu geben. Die notwendigen Grundlagen der störungstheoretischen Quantenchromodynamik (QCD) werden diskutiert, um die Vorhersagen für die Produktion von geladenen Hadronen zu motivieren. Das Bild des Partonenschauers wird erklärt und die Hilfsmittel um die derzeitigen Grenzen des Verständnisses des nicht-störungstheoretischen Teils der QCD Dynamik zu überwinden, werden erläutert. Diese Hilfsmittel sind die Ereignisgeneratoren, komplexe Monte Carlo Computerprogramme, die versuchen die physikalischen Prozesse, die das Thema der vorliegenden Arbeit sind, zu simulieren (Kapitel 1).

Das Studium von $\pi^{\pm}, \mathrm{K}^{\pm}$ und $\mathrm{p}(\overline{\mathrm{p}})$ beinhaltet notwendigerweise Teilchenidentifikation. DELPHI ist mit seinen RICH (Ring Imaging CHerenkov) Detektoren besonders gut für eine solche Studie ausgerüstet.

Im zweiten Kapitel werden daher die elektro-dynamischen Grundlagen der Identifikation von Teilchen durch den spezifischen Energieverlust diskutiert. Zwei Modelle werden vorgestellt: der moderne Zugang über das Photonen-Absorptions-Ionisations (PAI) Modell von Allison und Cobb, und die klassische Ableitung nach Bethe. Čerenkov-Strahlung wird als integraler

Teil des totalen Energieverlusts eines geladenen Teilchens behandelt, und ihre eigenständige Nutzung zur Teilchenidentifikation wird besonders hervorgehoben. Zum Schluß wird noch der wichtige Aspekt der statistischen Verteilung des Energieverlusts erläutert.

Das dritte Kapitel beschreibt kurz die experimentellen Grundlagen der Teilchenidentifikation, wie sie in dieser Arbeit verwendet werden. Dies sind der Energieverlust in der Zeitprojektionskammer (TPC), die Rekonstruktion der Anzahl von Čerenkov-Photonen und der Emissionswinkel des Čerenkov-Lichts mit einem Ringabbildenden Cherenkov (RICH) Detektor.

Die spezifischen Eigenschaften des DELPHI Detektors sind das Thema des vierten Kapitels. Der ganze Detektor wird kurz beschrieben, und die für die Teilchenidentifikation wichtigen Aspekte werden hervorgehoben. Die Spurrekonstruktionsdetektoren werden detailliert dargestellt, weil die Impulsrekonstruktion ein essentieller Bestandteil der Teilchenidentifikation ist. Die DELPHI TPC und RICH Detektoren werden mit allen im gegebenen Zusammenhang wichtigen Details beschrieben. Darauf folgt eine Diskussion von Algorithmen zur Teilchenidentifikation, und eine eingehendere Behandlung der Clustermethode, die für diese Arbeit gewählt wurde.

Das fünfte Kapitel stellt die Messungen selbst vor. Das beinhaltet die Ereignisselektion, die, wegen der bei diesen Energien Vielzahl von möglichen Prozessen, ein wichtiges Problem bei LEP 2 ist. Einige von der angesprochenen Prozesse, wie zum Beispiel hadronische Zerfälle von Paaren von W-Bosonen und direkte Produktion von Quark-Antiquarkpaaren resultieren in ähnlichen Endzuständen, und müssen daher sorgfältig getrennt werden, ohne dabei die Messung zu verfälschen.

Hernach wird die Selektion von geladenen Spuren für die Identifikation erklärt, und im Anschluß die Rekonstruktion der beobachteten Anzahl von $\pi^{\pm}, \mathrm{K}^{\pm}$ und $\mathrm{p}(\overline{\mathrm{p}})$. Letztere wird mit einer Effizienzenmatrix durchgeführt, die mit Hilfe von simulierten Daten bestimmt wird. Die Kalibration dieser Matrix auf das tatsächliche Detektorverhalten mit Hilfe von Z^0-Poldaten wird erklärt.

Als erstes Resultat erhält man bei dieser Methode auf eins normalisierte relative Produktionsraten von $\pi^{\pm}, \mathrm{K}^{\pm}$ und $\mathrm{p}(\overline{\mathrm{p}})$. Von da geht man über zu den Verteilungen der absoluten Produktionsraten, die üblicherweise mit Hilfe der logarithmischen Variable $\xi_p = -\ln(2p/E_{\mathrm{Schwerpunkt}})$ dargestellt werden. Aus diesen Verteilungen kann man einerseits durch Integration die durchschnittliche Multiplizität der einzelnen Hadronspezies bestimmen, andererseits sind sie auch für sich genommen sehr interessant, weil es eine störungstheoretische QCD Vorhersage für die Entwicklung des Maximums dieser Verteilungen als Funktion der Schwerpunktsenergie gibt.

Diese Arbeit stellt in Kapitel 6 auch zum ersten Mal eine Studie zur Produktion von $\pi^\pm, K^\pm$ und $p(\overline{p})$ in Zerfällen von W-Bosonen vor. Die Selektion dieser Ereignisse vor dem Hintergrund von direkter $q\overline{q}$ Produtkion wird beschrieben. Danach wird eine Analyse analog zu der vorherigen durchgeführt. Die Resultate werden dann als Messung bei einer effektiven Schwerpunktsenergie, die der Masse eines W-Bosons entspricht, interpretiert. In dieser Form können sie sehr gut mit den anderen Messungen dieser Arbeit und ähnlichen Messungen aus früheren Experimenten verglichen werden. Dies stellt eine wichtige Erweiterung des aktuellen Wissens über die Eigenschaften der W-Bosonpaarerzeugung dar. Einige eher technische Aspekte der vorliegenden Arbeit werden im Anhang behandelt.

Im letzten Kapitel werden die wichtigsten originären Aspekte dieser Arbeit zusammengefaßt, und es wird versucht aufzuzeigen, wo sie zum tieferen Verständnis der Phänomenologie der Quantenchromodynamik beiträgt.

Die vorliegenden Resultate wurden auf mehreren Konferenzen vorgestellt [1, 2, 3, 4] und werden in naher Zukunft als DELPHI-Publikation erscheinen.

Overview

This dissertation presents a comprehensive description of measurements of the production properties of charged pions, kaons, protons (and anti-protons), for short ($\pi^{\pm}, \mathrm{K}^{\pm}$ and $\mathrm{p}(\overline{\mathrm{p}})$), using data from the DELPHI (DEtector with Lepton Photon and Hadron Identification) experiment at LEP (Large Electron Positron collider). These data have been recorded by DELPHI in the so-called LEP 2 phase of the experiment, where higher and higher centre of mass energies have been explored.

The first energy step after the Z^0 pole was at 130 GeV and this has been increased until the year 1998 up to 189 GeV. The ultimate energy of LEP, 200 GeV, has been recently reached. All these high energy data including the 189 GeV energy point have been used in the present work, which for the first time performs these kind of measurements at the highest available energies in $\mathrm{e}^+\mathrm{e}^-$ collisions.

The first chapter tries to give a short phenomenological motivation for the interest in the present measurements. The necessary basics from perturbative Quantum Chromodynamics (QCD) are discussed to motivate the predictions for the production of identified hadrons. The picture of the parton shower is explained and the tools to overcome the present limitations of our understanding of the non-perturbative part of QCD dynamics are presented. These are the event generators, complex Monte Carlo programs, which attempt to simulate the physics processes, which are the topic of the present dissertation.

The study of $\pi^{\pm}, \mathrm{K}^{\pm}$ and $\mathrm{p}(\overline{\mathrm{p}})$ necessarily involves particle identification. DELPHI with its RICH (Ring Imaging CHerenkov) detectors is especially well equipped for such a study.

In the second chapter the electro-dynamical basis of particle identification using the specific energy loss is discussed. Two models are presented: The modern approach using the Photon Absorption Ionization model by Allison and Cobb, and the classic derivation by Bethe. Čerenkov radiation is treated as integral part of the total energy loss of a charged particle and its specific use for particle identification is emphasised. Finally the important aspect of the distribution of the energy-loss is briefly reviewed.

The third chapter describes shortly the experimental basics of particle identification used in this study. These are the energy-loss in the Time Projection Chamber (TPC), the reconstruction of the number of Čerenkov photons and the emission angle of the Čerenkov light using a Ring Imaging Cherenkov detector.

The specifics of the Delphi detector are the topic of the fourth chapter. The whole detector is described briefly and the important characteristics for particle identification are stated. The tracking detectors are discussed in somewhat more detail, because momentum reconstruction is an essential ingredient in the process of particle identification. The Delphi TPC and RICH detectors are described with the details necessary in the present context followed by a discussion of the particle identification algorithms available and a closer look on the clustering method which has been chosen for this work.

The fifth chapter presents the measurements. This includes the event selection, which is an important aspect at LEP 2 due to the numerous possible processes possible at these energies. Some of these like hadronic WW decays and direct $q\overline{q}$ production result in similar final states and have to be separated with great care, so as not to bias the measurement.

The selection of charged tracks for identification is then explained as well as the reconstruction of observed rates of $\pi^{\pm}, K^{\pm}$ and $p(\overline{p})$. This is achieved by means of an efficiency matrix which is established using simulation. The calibration of this matrix to the true detector response using Z^0 data is explained. The first immediate result of this procedure are normalised production rates, or particle fractions. From this one moves on to inclusive rate distributions which are conventionally shown in terms of the logarithmic variable $\xi_p = -\ln(2p/E_{\mathrm{cms}})$. These distributions serve on the one hand to extract the average multiplicities via integration and on the other hand they are interesting in themselves because the evolution of the peak of these distributions as a function of centre of mass energy is predicted by perturbative QCD.

This work for the first time presents a study of the production properties of identified hadrons originating from the production of W boson pairs. The selection of these events against a background of $q\overline{q}$ events is described. An analysis similar to the one just described is performed and the results are compared to the QCD predictions to the $q\overline{q}$ measurements at LEP 2 energies and to results from previous lower energy experiments. Some important but rather technical parts of the analysis are described in the appendix.

The final chapter summarises the main original points of this work and shows where they contribute to the deeper understanding of the phenomenology of QCD.

The present results have been presented at various conferences [1, 2, 3, 4] and will be published as a DELPHI paper in the very near future.

Acknowledgements

It is a pleasure to take this opportunity to express my gratitude to all the many people, who have given me the opportunity to perform this work.

First and foremost I want to thank Dietrich Liko, my friend and supervisor at CERN. The better part of what I know about experimental particle physics (and about computers) I learnt from him. Dietrich accompanied me at nearly every step to this work.

Then I am greatly indebted to my advisor in Vienna, Prof. Meinhard Regler from the Institute for High Energy Physics of the Austrian Academy of Sciences, who supported me throughout this work, and beyond it, with advise and interest.

I am also very grateful to Prof. Walter Majerotto, the director of the Institute for High Energy Physics, co-advisor of my thesis for his support and encouragement.

Prof. Valeri Khoze from Durham University was so friendly to read through the QCD chapter and gave valuable comments. I learned also a lot about QCD from him in a number of very interesting and stimulating discussions.

Niels Kjaer aided me a lot with his criticism and good ideas. I hope this work can at least partially meet his high standards of a physics analysis.

I got many good hints from Peter Kluit, especially in understanding the many details of the RICHes.

Emile Schyns helped me to get started, encouraged me with his constant interest and let me into many details of his analysis of $\pi^{\pm}, \mathrm{K}^{\pm}$ and $\mathrm{p}(\overline{\mathrm{p}})$ production at LEP 1.

Pedro Abreu helped me with the event-generators. I want to thank him, Alessandro de Angelis, Nuno Anjos and Lorenzo Vitale for the good collaboration in the work of our common paper, of which this thesis is a part.

The people in the Delphi RICH group, of which I am happy to be a part, will for me ever remain a shining example of good and friendly spirit and collaboration. I want to mention here Valerio Gracco and Christian Joram who provided me also with a wealth of information on particle identification detectors.

I am especially grateful to Olav Ullaland, for his friendship and support and for having always an open ear for me, during and (especially) after working-hours.

Fredrik Tegenfeldt and Mario Alemi, my fellow-students, added to the great fun, which this work has also been.

Special thanks go to my friend Andrew Maier for a last-minute fix on the title page.

I am grateful to Marco Battaglia for encouraging me, by his confidence in my abilities from the beginning on. Marco also did very much to make Geneva a new home for me.

The present work is the result of a two and a half years stay at CERN, as a member of the DELPHI collaboration. This was made possible by the Austrian CERN-PhD programme, for which I am very grateful. The time here has been a tremendous intellectual and scientific joy for me, which still continues.

My family back in Austria, my grandparents, my parents and my brother: I want to thank them for their good thoughts, care, encouragements, their trust and their ever warm welcome, when I am coming back.

As is wont with these kind of acknowledgements, at last I come to my dear Inge, my wife, who not only delayed her personal career for me but who also endured with patience, humour and love the live at the side of an enthusiastic physicist. She almost never complained about long working hours, week-ends and nights spent at CERN. I wouldn't know what I could wish for more.

Contents

Chapter 1

Multihadron production and Quantum Chromodynamics

Multihadron production in e^+e^- collision is described by Quantum Chromodynamics (QCD). The initial short distance production processes are quark pair production (possibly with hard gluon radiation) or a WW pair production like in Figure 1.1, where at least one W decays hadronically.

The subsequent production of partons can be described by perturbative QCD. This chapter profited mostly from [5, 6, 7].

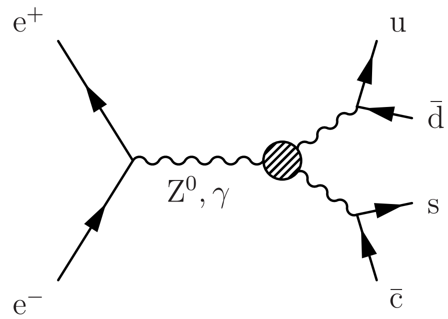

Figure 1.1: WW pair production at LEP 2. Both W bosons decay hadronically.

1.1 Quantum Chromodynamics

Quantum Chromodynamics (QCD) is *the* universally accepted theory of strong interactions. It is formulated in terms of elementary fields (quarks and gluons), whose interactions obey the principles of a relativistic Quantum Field Theory, with a non-abelian gauge invariance SU(3). The charge associated with this gauge group is called *colour*. Hadrons are made up of spin $\frac{1}{2}$ quarks which are colour-triplets. Quarks interact via exchanging spin 1 colour-octet bosons, the gluons. In principle every perturbative prediction of QCD can be derived from the Lagrangian:

$$\mathcal{L} = -\frac{1}{4}F^A_{\alpha\beta}F^{\alpha\beta}_A + \sum_{\text{flavours}} \overline{q}_a(i\not{D} - m)_{ab}q_b - \frac{1}{2\lambda}(\partial^\alpha \mathcal{A}^A_\alpha)^2 + \partial_\alpha \eta^{A\dagger}(D^\alpha_{AB}\eta^B) \tag{1.1}$$

Here, as everywhere in this chapter, summation over double indices is tacitly assumed (Einstein summation convention). The capital indices A, B run from $1 \dots 8$ corresponding to the eight types of gluons. The lower case roman indices a, b run over the three colours of the quarks, $1 \dots 3$. Greek indices $\alpha, \beta, \dots$ are Lorentz indices. For the sake of clarity the Lorentz indices and the spinor indices of the quarks have been suppressed. The first term is the kinetic term of the gluons, the second is an incoherent sum over all the quark flavours (and the three colours), of which 6 are currently known. From the point of view of QCD all quark-flavours are equal[1]. This is often referred to as the "flavour blindness" of QCD. The covariant derivative

$$(D_\alpha)_{ab} = \partial_\alpha \delta_{ab} + i g_s (t^C \mathcal{A}^C_\alpha)_{ab} \tag{1.2}$$

includes the interaction of quarks and gluons. Here g_s is the strong coupling. The capital indices A, B again run over the 8 gluons. The third term is the so called gauge-fixing term, which is necessary for the definition of the gluon propagator[2]. The last term is the ghost term needed in any non-abelian theory to compensate the unphysical degrees of freedom. From the Lagrangian the Feynman rules can be derived. The complete set is shown in Figure 1.2.

The running of the coupling α_s

In the course of evaluating loop diagrams such as the self energy of the quark:

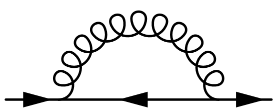

$$= iC_F \int \frac{d^4\ell}{(2\pi)^4} \frac{1}{\ell^2(p+\ell)^2} \tag{1.3}$$

[1]That is to say, the gluons "see" only the colour charge, not the flavour of the quarks they couple to. Of course the different masses of the different flavours influence the results strongly via the kinematics.

[2]The gauge fixing chosen here parametrises the class of *covariant* gauges characterised by λ.

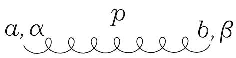

$$= \delta^{ab}\frac{-i\,g^{\alpha\beta}}{p^2+i\epsilon} \quad \text{(Feynman gauge)}$$

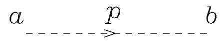

$$= \delta^{ab}\frac{i}{p^2+i\epsilon}$$

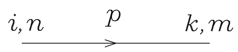

$$= \delta^{ik}\,\frac{i}{\not{p}-m+i\epsilon}\bigg|_{mn}$$

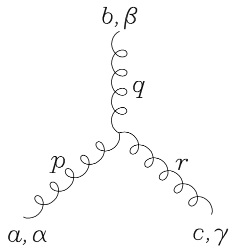

$$= gf^{abc}\left[g^{\alpha\beta}(p-q)^\gamma + g^{\beta\gamma}(q-r)^\alpha + g^{\gamma\alpha}(r-p)^\beta\right]$$

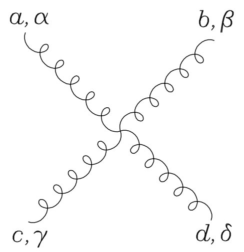

$$\begin{aligned} = \; & -ig^2 f^{xac} f^{xbd}\left(g^{\alpha\beta}g^{\gamma\delta} - g^{\alpha\delta}g^{\beta\gamma}\right) \\ & -ig^2 f^{xad} f^{xbc}\left(g^{\alpha\beta}g^{\gamma\delta} - g^{\alpha\gamma}g^{\beta\delta}\right) \\ & -ig^2 f^{xab} f^{xcd}\left(g^{\alpha\gamma}g^{\beta\delta} - g^{\alpha\delta}g^{\beta\gamma}\right) \end{aligned}$$

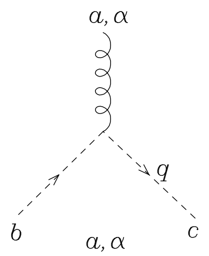

$$= -gf^{abc}\,q^\alpha$$

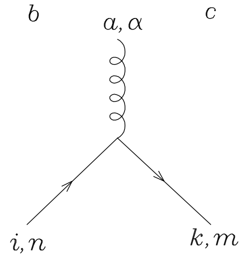

$$= ig\,\lambda^a_{ki}\,\gamma^\alpha_{mn}$$

Figure 1.2: Feynman rules of QCD (in Feynman gauge).

one encounters infinities such as the integral to the right of eq. (1.3). The mathematical techniques to deal with these kind of infinities are *regularisation* and *renormalization*. Without going into any details only the results which are relevant in the following discussion are quoted here.

The infinities are compensated by so-called counter terms. Another way of expressing the latter is the transformation of the original wave-functions and couplings[3] in the Lagrangian (1.1).

$$\psi_{bare} = Z_2^{\frac{1}{2}} \psi_R \tag{1.4}$$

$$A^\mu_{bare} = Z_3^{\frac{1}{2}} A^\mu_R \tag{1.5}$$

$$g_{bare} = Z_g \mu^\epsilon g_R \tag{1.6}$$

Here μ is an arbitrary mass parameter, the renormalization scale, which has been introduced in regularising the integrals[4]. The counter-terms are fixed by demanding that the 1-loop green functions remain finite. For the coupling this leads to:

$$Z_g = 1 - \frac{1}{\epsilon}\left(\frac{b_0}{2}\right)\alpha_s \tag{1.7}$$

where $\alpha_s = g^2/4\pi$ has been introduced and b_0 contains factors from the group algebra, the number of colours and active flavours.

As has been said, the parameter μ is arbitrary and measurable observables must not depend on it. In particular the bare coupling g_{bare} is independent of μ:

$$\frac{dg_{bare}}{d\mu} = 0 \tag{1.8}$$

This leads to

$$\frac{d\alpha_s}{d\log\mu^2} = -b_0\alpha_s^2 + O(\alpha_s^3, \epsilon) \tag{1.9}$$

Solving this differential equation leads to the famous prediction of the *running of* α_s:

$$\alpha_s(\mu^2) = \frac{1}{b_0 \log(\mu^2/\Lambda^2)} \tag{1.10}$$

[3]Quarks are assumed to be massless. The mass terms do not introduce a qualitatively different behaviour.

[4]ϵ arises in the widely used *dimensional regularisation* where integrals are calculated in non-integer dimensions.

The parameter Λ enters when solving the first order differential equation (1.9) describing the running of α_s. It corresponds to the scale where the coupling becomes infinite. Since

$$b_0 \overset{N_c=3}{=} \frac{1}{12\pi}(33 - 2n_f) \tag{1.11}$$

where n_f is the number of active quark flavours in the process at hand, eq. (1.10) shows that α_s becomes smaller with higher scales μ. This is called asymptotic freedom. The observation of this phenomenon is one of the great successes of QCD. Figure 1.3 shows a current DELPHI measurement of the running of α_s.

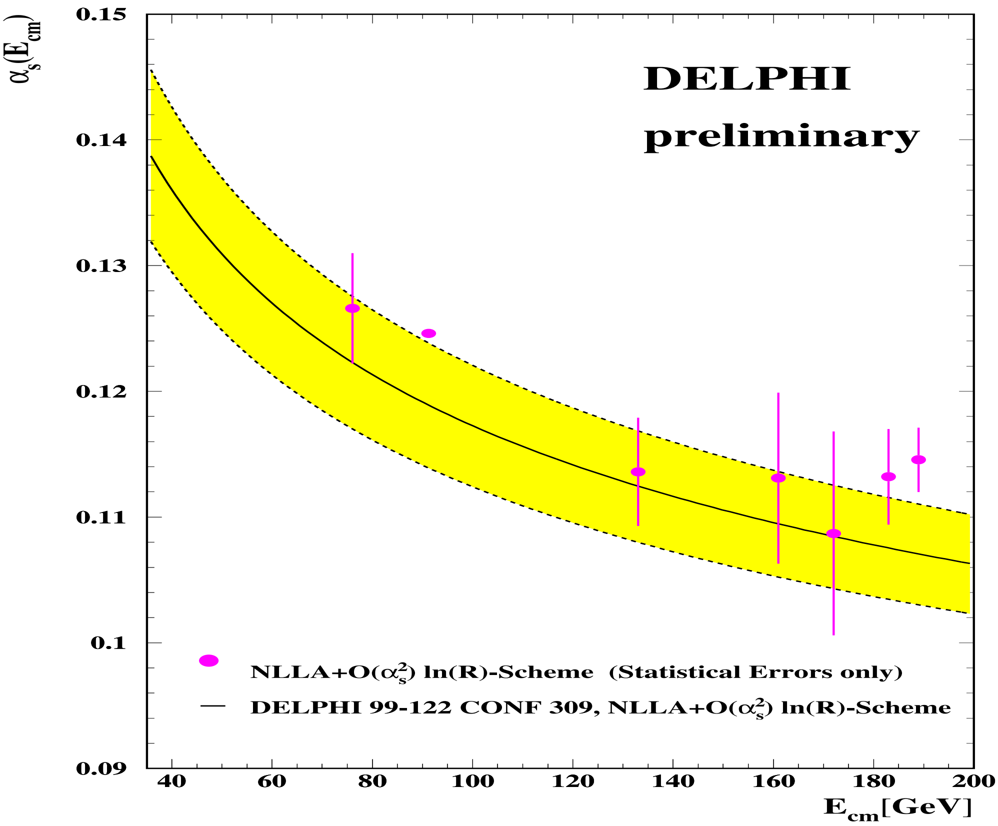

Figure 1.3: Energy dependence of α_s measured by the average of event shape variables. The yellow band shows the Next-to-Leading order (NLO) QCD prediction using the value of α_s at M_{Z^0}.

1.2 QCD in e^+e^- collisions

Although e^+e^- collisions are a very clean point like source of quarks and gluons, it is not straightforward to predict the final states observed at LEP. These do not consist of quark pairs and they are also not a simple collection of gluons and quarks. One may well wonder how QCD achieves the trick of ending up with a multitude of charged and neutral colour-singlet hadrons, while the starting point of all this is the production of two quarks which have colour and fractional charge and are flying in opposite directions at almost the speed of light.

The solution to this puzzle is intimately connected to the time evolution of the process and the different energy scales involved. When the $q\overline{q}$ pair is produced, the binding force is proportional to α_s. The latter is small at this scale so the particles can be treated as free to a good approximation. Also the first gluon radiations are perturbative and they continue to be so until a time after the creation of 1/1 GeV, when gluons with wavelengths $\geq$ 1/1 GeV are emitted. At this scale the coupling constant has become large, non perturbative phenomena start to be important. What is important is that the radiation during the perturbative phase organises itself in a way so as to form colour-neutral, low mass, parton clusters, which are concentrated in small areas of the phase space.

Therefore the complete neutralisation of colour and also the *hadronisation* need not involve any long range interactions between objects which are now far away in phase space. At this time scale these forces would be enormous and completely upset the structure of the final state. In addition as a result of this evolution before "confinement" the memory of the clusters is wiped out. They do not know where they came from. This leads to the assumption that the properties of hadronisation are universal. Properties measured at one energy should also hold at other energies. Also the total hadron production rate should not much be influenced by the hadronisation phase [8].

Soft gluon emission

Emission of soft gluons plays a fundamental rôle in the evolution of the final state [7]. Soft gluons are emitted with large probability since the emission spectrum behaves like $dE/E\, dk_\perp^2/k_\perp^2$, typical for bremsstrahlung. Soft gluons are insensitive to the details of the very-short-distance dynamics. They can not resolve features of interactions which take place at time scales shorter than their wave length. They also do not care about the spin of partons, they are only sensitive to the colour charge. The Feynman rule for soft gluon emission is simply:

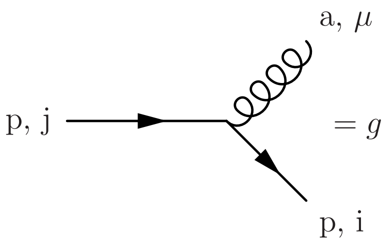

$$= g\lambda^a_{ij} 2p^\mu \tag{1.12}$$

A key property of soft gluon emission is *angular ordering* [7] . This is the continuous reduction of the opening angle at which soft gluons are emitted. As a result this radiation is confined to a smaller and smaller cone around the quark direction and the final state looks like collimated jets of partons. Moreover the colour flow during the jet evolution forces the $q\overline{q}$ pairs which can form a colour singlet to stay close in phase space. This leads to the later confinement of the clusters.

If one looks at the emission of soft gluons from the original pair one finds that soft gluons are emitted in cones of phase space. These cones are defined by rotating the quark axis around the anti-quark axis and vice versa. The two fermions can be seen as indendent emitters and the quantum coherence is accounted for by constraining emission to the cones.

If one now emits an additional gluon one will find a similar angular constraint. This time the emitters are the two colour lines flowing from the gluon to the quark and from the anti-quark to the gluon respectively. The emission will take place in the cone formed by the gluon and the quark or anti-quark. In either case the opening angle is smaller than the original. The effective strong coupling for such an emission is

$$\alpha_s(k_\perp) = 2\pi / b \ln(k_\perp/\Lambda) \tag{1.13}$$

The fact the colour always flows from the emitting parton to the emitted one, the collimation of the jet and the softening of the radiation ensures that partons forming a colour singlet cluster are close in phase space. Thus hadronisation (which will bind the singlet clusters into hadrons) takes place locally inside the jet and is not a collective process. The inclusive properties of jets such as particle multiplicity, jet mass, jet broadening are independent of hadronisation, up to corrections of order $(\Lambda/\sqrt{s})^n$, with $\Lambda \simeq 1$ GeV.

Some inclusive results

The most inclusive and simple quantity is the total hadronic cross section $R = \sigma(e^+e^- \to q\overline{q})$, which has been calculated up to $O(\alpha_s^3)$

$$R = K_{QCD} 3 \sum_q Q_q^2$$

$$K_{QCD} = 1 + \frac{\alpha_s(s^2)}{\pi} + \sum_{n \geq 2} C_n(1) \left(\frac{\alpha_s(s^2)}{\pi} \right)^n \tag{1.14}$$

The coefficients C_2 and C_3 can be found e.g. in ref. [6].

Often used are also so called *event shape* variables. These should be *infrared safe*, that is insensitive to the emission of soft gluons. A widely used such quantity is the thrust

$$T = \max_{\mathbf{n}} \frac{\sum_i |\mathbf{p}_i \cdot \mathbf{n}|}{\sum_i |\mathbf{p}_i|} \tag{1.15}$$

Here $\mathbf{n}$ is the thrust axis, defined to maximise T. In lowest order the average value is given by

$$\langle 1 - T \rangle = \frac{\alpha_s C_F}{\pi} \tag{1.16}$$

Figure 5.5 on page 53 shows the distribution of the thrust variable for hadronic events at LEP 2.

Another interesting observable is the average multiplicity which is given

$$\langle n_{\text{part}} \rangle \sim \exp \sqrt{\frac{2C_A}{\pi b} \log \frac{s}{\Lambda^2}} \tag{1.17}$$

This equation is a prediction for the evolution of the multiplicity as a function of the centre of mass energy. Figure 1.4 shows the latest DELPHI measurement for this evolution compared to low energy results from ref. [4].

1.3 Single particle spectra and Local Parton Hadron Duality

To this day perturbative QCD gives directly measurable results only for inclusive quantities such as the hadronic cross section, the thrust and others. More detailed observables such as single particle spectra need some additional assumptions. The impressive success of these techniques has strengthened the present confidence in QCD.

The question arises whether the "duality" between partons and hadrons showing itself in quantities like thrust, can not be carried a little bit further

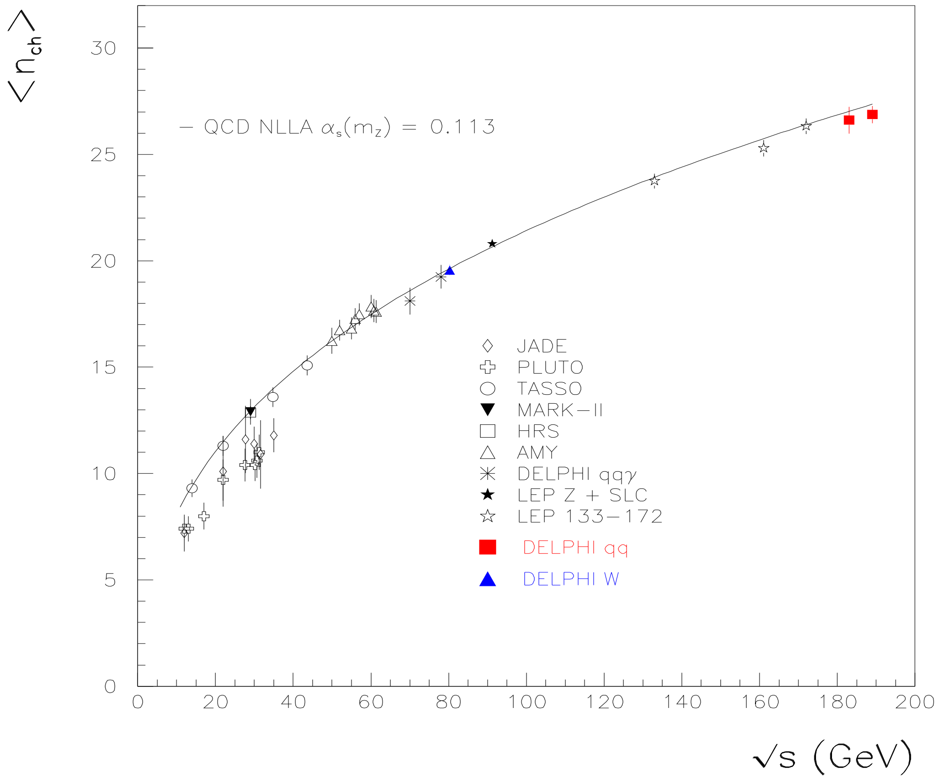

Figure 1.4: Measured average charged particle multiplicity in $e^+e^- \rightarrow q\bar{q}$ events as a function of centre-of-mass energy $\sqrt{s}$. DELPHI high energy results are compared to experimental results from lower energy experiments ([9, 10, 11, 12, 13, 14]) and to a fit to a prediction from QCD in Next-to-Leading Order. The average charged multiplicity in W decays is also shown at an energy corresponding to the W mass. The measurements have been corrected for the different proportions of $b\bar{b}$ and $c\bar{c}$ events at the various energies.

to the level of single partons and hadrons themselves. In the course of these considerations one is led to the introduction of an additional parameter Q_0 where $Q = p\Theta$ in general is the energy scale involved in the emission of a new parton. Θ is the opening angle of the phase-space cone just described and p the momentum. Q_0 is simply the energy scale where our perturbative techniques begin to fail. Above this scale perturbation theory can in principle predict everything, below one has to resort to other techniques such as Monte Carlo modelling, which is described later.

It is clear thus that quantities like particle multiplicities, inclusive spectra and other observables which count individual particles depend explicitly on the cut-off Q_0. The smaller the cut-off the higher the multiplicity.

The Local Parton Hadron Duality (LPHD) [15, 16] hypothesis maintains that the hadronic spectra are proportional to the partonic ones if the cut-off Q_0 of the parton cascade is decreased to a value which is of the order of the hadron mass itself. Generally the idea is to compute hadronic observables from partonic final states:

$$O(x_1, x_2, \dots)|_{hadrons} \sim O(x_1, x_2, \dots; \Lambda; Q_0)|_{partons} \tag{1.18}$$

Q_0 is an effective mass scale which for charged particles can be chosen as $Q_0 \simeq \Lambda \simeq 250$ MeV.

It has been emphasised by the creators and it shall be restated here that LPHD is in fact a hypothesis which can not be strictly deduced from QCD. It is a powerfull tool which allows one to carry perturbative predictions to areas where infrared safety is not guaranteed.

In the following the basic results for single particle distributions will be stated. The derivations will not be given as they can be found in the literature [7, 17]. Some frequently used notations will be collected here:

$$\begin{aligned}
\lambda &= \ln \tfrac{Q_0}{\Lambda} \\
\xi_p &= \ln \tfrac{1}{x_p} \\
Y &= \tfrac{E\Theta}{Q_0} \\
a &= \tfrac{11}{3} N_C + \tfrac{2n_f}{3N_C^2} \\
x_p &= \tfrac{p}{E_{jet}} \\
\tau &= Y = \ln \tfrac{E}{\Lambda} \\
b &= \tfrac{11N_C - 2n_f}{3} \\
C &= \tfrac{a^2}{16 N_C b} = 0.2915\,(0.3513) \text{ for } n_f = 3\,(5)
\end{aligned} \tag{1.19}$$

The full expression for the inclusive distribution of partons in terms of the variable ξ_p is [15, 16]

$$D_i^f(\xi_p, Y, \lambda) = \frac{4N_C(Y+\lambda)}{bB(B+1)} \int\limits_{\epsilon - i\infty}^{\epsilon + i\infty} \frac{d\omega}{2\pi i} x^{-\omega} \Phi(-A+B+1, B+2, -\omega(Y+\lambda))\mathcal{K} \tag{1.20}$$

Here Φ denotes the confluent hypergeometric function.

Eq. (1.20) can be solved numerically, analytic expressions exist in the extreme case of $\lambda = 0$, the "limiting spectrum" [15, 16]. This equation

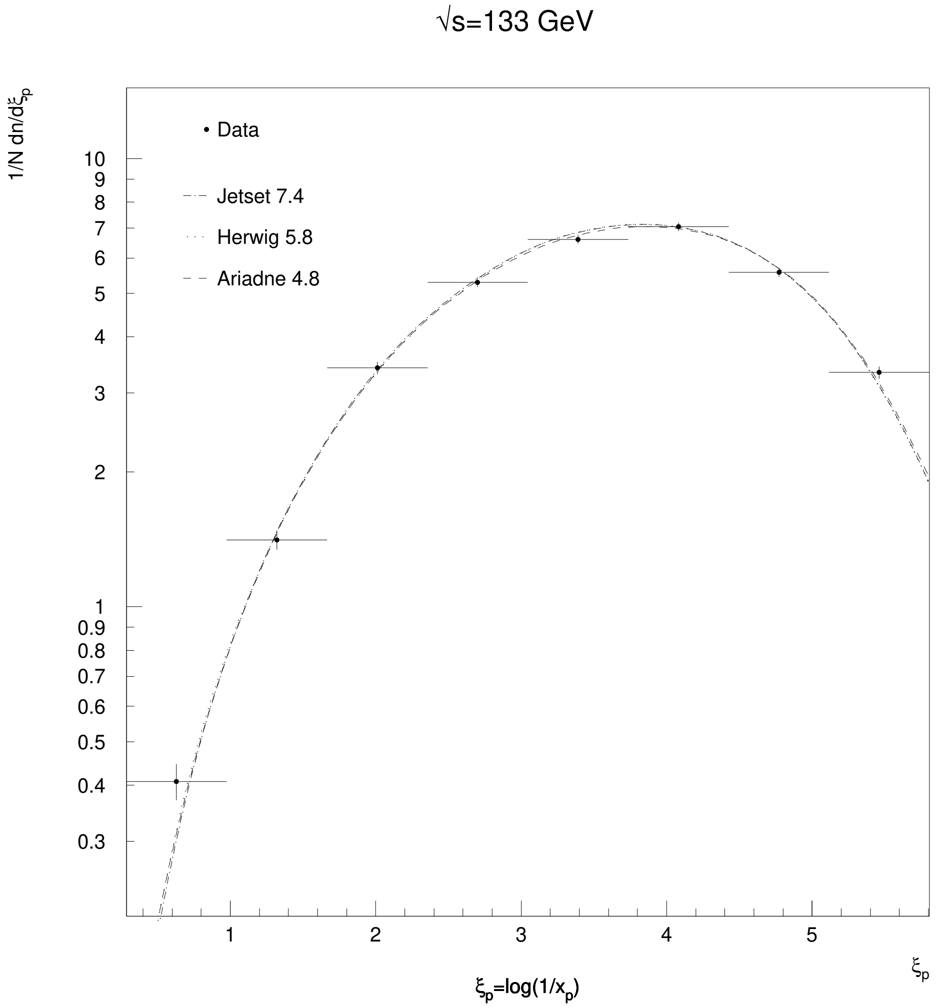

Figure 1.5: ξ_p distribution of charged hadrons at 130 and 136 GeV. Delphi data superimposed to the predictions from Jetset, Herwig and Ariadne shows the Hump Backed plateau. Also shown is a fit to equation (1.21). Chapter 5 describes the experimental methods used for obtaining this figure.

displays the famous humped back plateau as illustrated by the Figure 1.5. It can be approximated by the more convenient form of a distorted Gaussian

$$D(\xi_p) \simeq \frac{N}{\sigma\sqrt{2\pi}} \exp\left(\frac{1}{8}k - \frac{1}{2}s\delta - \frac{1}{4}(2+k)\delta^2 + \frac{1}{6}s\delta^3 + \frac{1}{24}k\delta^4\right) \qquad (1.21)$$

where $\delta = (\xi - \bar{\xi})/\sigma$.

The coefficients $\bar{\xi}, \sigma, s, k$ have been calculated for the case of the limiting spectrum in [18].

An interesting aspect of this distribution is the "typical" value of the quantity ξ_p. Two definitions are of special interest in the following (first discussed in ref. [19]).

1. The *mean* value, $\bar{\xi} = \int_0^\infty d\xi\, D(\xi)\xi$
2. The *modal* or *peak* value, ξ^* at which $D(\xi)$ reaches its maximum.

Predictions for massive hadrons

When dealing with particle heavier than pions the simplifications brought about by the "limiting spectrum" can not be applied. The partonic formulae are truncated at different values Q_0 ($Q_0(m_h) > \Lambda$). There is no prescription of how to relate m_h to Q_0. In ref. [20] the shape parameters $\bar{\xi}, \sigma, k, s$ for the distorted Gaussian of eq. (1.21) have been calculated for the case $Q_0 \neq \Lambda$. The main effect of truncating the scale, going to the high energy approximation, is:

$$\bar{\xi} = \frac{1}{2}Y + \frac{a}{4\sqrt{bN_c}}(\sqrt{Y+\lambda} - \sqrt{\lambda}), \tag{1.22}$$

$$\sigma^2 \approx \frac{1}{12}\sqrt{\frac{b}{N_C}}\left((Y+\lambda)^{\frac{3}{2}} - \lambda^{\frac{3}{2}}\right) - \frac{b}{32N_C}\left((Y+\lambda) - \lambda\right), \tag{1.23}$$

the limiting spectrum corresponding to $\lambda = 0$. One expects a stiffening of the spectrum for the truncated spectrum, i.e. the average and the width become smaller with λ increasing.

For the position of the maximum one can see that the non-zero skewness leads to a calculable splitting between ξ^* and $\bar{\xi}$, namely

$$\xi^* - \bar{\xi} \approx \frac{3a}{32N_C} = 0.351\,(0.355) \text{ for } n_f = 3\,(5). \tag{1.24}$$

Here n_f is the number of active flavours. This result is independent of $\sqrt{s}$ and of Q_0 [20]. Furthermore

$$\xi^* \approx \tau\left(\frac{1}{2} + \sqrt{\frac{C}{\tau}} - \frac{C}{\tau} + O(\tau^{\frac{-3}{2}})\right) + F(\lambda) \tag{1.25}$$

with $F(0) = 0$. Based on results in ref. [20] it was proposed in ref. [21] to fit both $F(\lambda)$ and its inverse $\lambda(F)$ to polynomials as

$$F(\lambda) \quad = -1.46\lambda + 0.207\lambda^2 \pm 0.06 \tag{1.26}$$

$$\lambda(F) \quad = -0.614F + 0.153F^2 \pm 0.06 \tag{1.27}$$

In chapter 5 these prediction will be compared to LEP 2 data.

1.4 Monte Carlo generators

In the last section of this chapter an indispensable tool for any detailed QCD study will be shortly discussed. The parton shower described in the previous sections can be conveniently implemented in a computer program. Using angular ordering, this embodies a good part of the true QCD dynamics which can not be calculated to its full extent[5]. A QCD event generator combines this with a non-perturbative model of the hadronisation process at energy scales below Q_0. A good review is ref. [22]. These programs start from initial

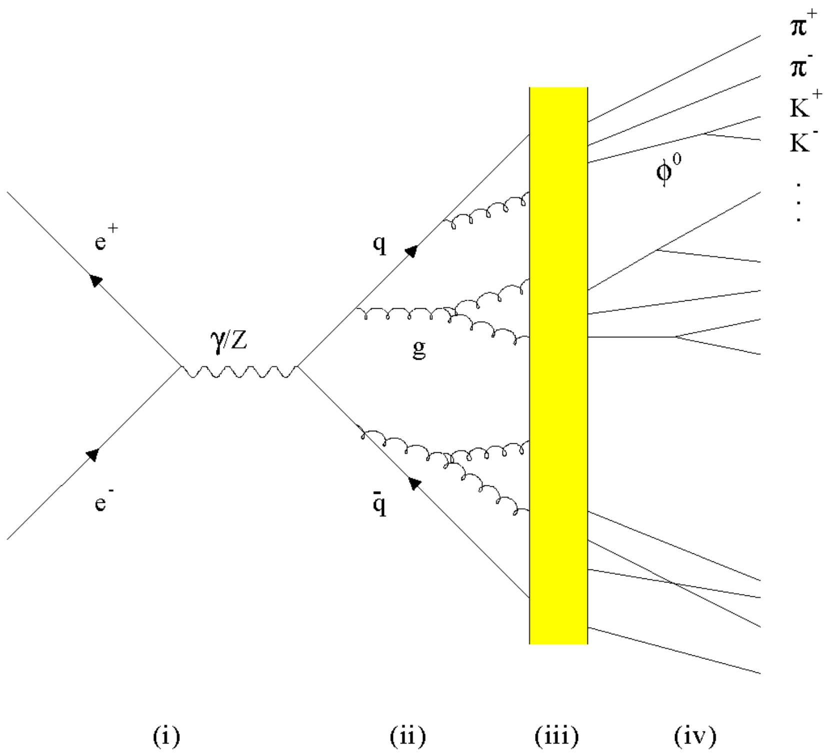

Figure 1.6: Sketch of the stages of a typical hadronic process. Annihilation of a e^+e^- pair into a gauge boson which decays into a primary quark anti-quark pair (i); radiation of gluons from the pair according to the perturbative parton shower model described (ii); non-perturbative transformation of partons into hadrons (iii); decay of the short lived hadrons (iv). Figure taken from ref. [23].

partons and generate successive branching, a parton cascade as in Figure 1.6

[5] The number of diagrams to calculate increases roughly factorially with orders of α_s.

evolves which stops as soon as the program reaches the cut off scale. Different models have been proposed for the subsequent step of converting the partons to hadrons:

1. Independent fragmentation
2. String model
3. Cluster model

In the first model which was originally proposed by Field and Feynman [24] each parton fragments individually. As long as there is enough energy new quark anti-quark pairs are created out of the vacuum and the anti-quark is combined with a quark. Gluons are first split in $q\overline{q}$ pairs. The model has been relatively successful in describing the broad features of two-jet and three-jet final states in e^+e^- annihilation at moderate energies. It has weaknesses however since it violates momentum conservation that has to be restored afterwards by rescaling. It also artificially separates jets which are very close in phase space.

In the string model [25, 26, 27, 28] the quark and anti-quark are supposed to move outwards in opposite directions, loosing energy in the colour field, which is modelled as a string-like configuration between them. The string has a uniform energy per unit length, corresponding to a linear quark confining potential. The string breaks up into hadron-sized pieces through spontaneous $q\overline{q}$ pair production in the intense colour field. Gluons are represented as kinks in the string, each carrying localised energy and momentum of its parent gluon. The fragmentation leads to an angular distribution which is in good agreement also for multi-jet events. There is an ambiguity how strings should be connected between the various quarks, anti-quarks and gluons. In most cases it is however possible to arrange the partons in a planar configuration, so that they have equally strong and opposite colour charge with respect to their neighbours. It is similar in the case where the parton cascade is modelled by radiating colour dipoles. The string segments, the segments then break up into hadrons; the exact mechanism is described by the *fragmentation function*.

The cluster models take up the concept of *preconfinement* described in the previous section. Preconfinement describes the mechanism how colour remains locally compensated between partons which are close to each other in phase space. This suggests a *cluster hadronisation* model, in which colour-singlet clusters of partons form after the perturbative phase of jet development and then decay into observed hadrons. Gluons are split into $q\overline{q}$ pairs. Neighbouring quarks and anti-quarks are combined into singlets. The resulting mass spectrum is universal and determined by the QCD scale Λ, Q_0, and the gluon splitting mechanism. The decay of clusters into hadrons is determined by the phase space and the density of possible states. This reproduces the observed hadronic energy and transverse momentum distribution without the need to introduce any adjustable fragmentation functions.

The two latter models are used in very popular QCD event generator programs which are widely used to compare the theory to the data. JETSET [29] and ARIADNE [30] use the string model, ARIADNE uses the before-mentioned colour dipole model for the perturbative cascade. HERWIG [31] on the other hand, while having also a coherent parton shower algorithm for the cascade uses the cluster fragmentation for the hadronisation. In general, as will be seen also in this work, JETSET and ARIADNE describe the data a little bit better than HERWIG, it should be kept in mind though, that HERWIG has approximately only half the number of adjustable parameters.

Chapter 2

Specific energy loss, Identification of charged particles

In this chapter the theoretical basis of the identification of charged particles shall be reviewed. One can discern two classes of methods for measuring the mass of a particle, that is to establish its identity.

1. After the absolute value of the momentum p has been measured, a second observable is used, which does not have a homogeneous, linear functional dependence on p. Examples of such observables include a measurement of the *time of flight* t. Together with a measurement of the momentum p it allows to calculate the velocity β and hence the invariant mass m_0. The time difference between two species of masses m_1 and m_2 is

$$t_1 - t_2 \sim (d/2c)\left(\sqrt{1+\frac{m_1^2c^4}{p^2c^2}} - \sqrt{1+\frac{m_2^2c^4}{p^2c^2}}\right) \tag{2.1}$$

   where d is the (known) distance between two measurement points and p is the (measured) momentum. Assuming a time resolution of a fraction of a nanosecond, a path length of roughly p^2 meters is required to separate π and K mesons at a momentum p [GeV/c]. For the present study this is therefore not a useful approach

   For stable or long lived charged particles the (mass-)specific energy loss is the method par excellence for particle identification. This energy loss causes a variety of detectable phenomena: specific ionization loss, Čerenkov radiation and transition radiation.

2. Kinematical reconstruction of particle decays can be a powerful tool for identification of particles but it is not applicable for relatively long lived or stable particles like π's, K's and protons which are the main interest of this work. Furthermore difficulties arise when the kinematical problem is under-constrained, which is the case in the presence of neutral decay products, or reconstruction inefficiencies.

2.1 Energy loss by relativistic particles traversing a medium

This section describes the electrodynamic basis of the theory of energy loss, it follows closely refs. [32] and [33, 34]. The starting point are the Maxwell equations in matter[1]:

$$\nabla \mathbf{H} = 0, \nabla \times \mathbf{E} = -\frac{1}{c}\frac{\partial \mathbf{H}}{\partial t}, \tag{2.2}$$

$$\nabla \epsilon \mathbf{E} = 4\pi\rho, \ \nabla \times \mathbf{H} = \frac{1}{c}\frac{\partial \epsilon \mathbf{E}}{\partial t} + \frac{4\pi}{c}\mathbf{j}. \tag{2.3}$$

Here the charges and currents are given by:

$$\rho = e\delta(\mathbf{r} - \mathbf{v}t), \ \mathbf{j} = e\mathbf{v}\delta(\mathbf{r} - \mathbf{v}t) \tag{2.4}$$

One introduces as usual a scalar and a vector potential

$$\mathbf{H} = \nabla \times \mathbf{A}, \ \mathbf{E} = -\frac{1}{c}\frac{\partial \mathbf{A}}{\partial t} - \nabla\phi \tag{2.5}$$

and imposes a generalised Lorentz condition

$$\nabla \mathbf{A} + \frac{1}{c}\frac{\partial \epsilon\phi}{\partial t} = 0 \tag{2.6}$$

Inserting (2.5) in (2.3) results in the following equations for the potentials:

$$\mathbf{\Delta A} - \frac{\epsilon}{c^2}\frac{\partial^2 \mathbf{A}}{\partial t^2} = -\frac{4\pi}{c}e\mathbf{v}\delta(\mathbf{r} - \mathbf{v}t) \tag{2.7}$$

$$\epsilon\left(\mathbf{\Delta}\phi - \frac{\epsilon}{c^2}\frac{\partial^2 \phi}{\partial t^2}\right) = -4\pi e\delta(\mathbf{r} - \mathbf{v}t) \tag{2.8}$$

[1] The magnetic permeability μ is set to 1, since magnetic properties are irrelevant at the frequencies involved in ionization.

It should be noted that ϵ, the dielectric constant, is in general a tensor. These equations are solved by expressing all fields in terms of their Fourier components leading to:

$$\phi(\mathbf{k}, \omega) = 2e\delta(\omega - \mathbf{k} \cdot \beta)/k^2\epsilon \tag{2.9}$$

$$\mathbf{A}(\mathbf{k}, \omega) = 2e\frac{(\omega\mathbf{k}/k^2c - \beta)}{(-k^2 + \epsilon\omega^2/c^2)}\delta(\omega - \mathbf{k} \cdot \beta c) \tag{2.10}$$

The mean energy loss per unit length, i.e. the force of the emitted field acting on the electron, known conventionally as $\langle \mathrm{dE/dX} \rangle$, is due to the longitudinal component of $\mathbf{E}$ at the point $\mathbf{r} = \boldsymbol{\beta}ct$. Inserting everything yields:

$$\begin{aligned}\mathrm{dE/dX} = \frac{e\mathbf{E}(\beta ct, t)\boldsymbol{\beta}}{\beta} = \\ \frac{ie^2}{2\pi^2\beta}\iint d^3k d\omega \left(\frac{\frac{\omega}{c}\left(\frac{\omega\mathbf{k}\cdot\beta}{k^2} - \beta^2\right)}{\left(-k^2 + \frac{\epsilon\omega^2}{c^2}\right)} - \frac{\mathbf{k}\cdot\boldsymbol{\beta}}{k^2\epsilon} \right) \times \\ \delta(\omega - \mathbf{k}\cdot\beta c)\exp(i(\mathbf{k}\cdot\boldsymbol{\beta}c - \omega)t) = \\ \frac{ie^2}{\beta\pi}\int dk \int_{-\infty}^{\infty} d\omega \frac{k}{\beta}\left(\frac{\omega\left(\frac{\omega^2}{k^2c^2} - \beta^2\right)}{-k^2c^2 + \epsilon\omega^2} - \frac{\omega}{k^2\epsilon c^2} \right).\end{aligned} \tag{2.11, 2.12}$$

In the last step the $d^3k = 2\pi k^2 dk d(cos\theta)$ integration has been done assuming that ϵ is isotropic. Now using that $\epsilon(-\omega) = \epsilon^*(\omega)$ one obtains the final expression:

$$\begin{aligned}\langle \mathrm{dE/dX} \rangle = -\frac{2e^2}{\pi\beta^2}\int_0^{\infty} d\omega \int_{\omega/v}^{\infty} dk \Bigg(\omega k \left(\beta^2 - \left(\frac{\omega}{ck}\right)^2\right) \times \\ \mathrm{Im}\left(\frac{1}{-k^2c^2 + \epsilon\omega^2}\right) - \frac{\omega}{kc^2}\mathrm{Im}\left(\frac{1}{\epsilon}\right)\Bigg)\end{aligned} \tag{2.13}$$

The lower limit of the integral over k depends on the particle velocity v. The averaging $\langle\rangle$ is an expression of the homogeneity of the medium. The energy loss is determined by the manner in which the complex dielectric constant ϵ depends on the wave number k and the frequency ω. Once $\epsilon(k, \omega)$ is known, $\langle \mathrm{dE/dX} \rangle$ can be calculated for every β. $\epsilon(k, \omega)$ is determined by the atomic structure of the medium. For practical purposes simplified models can be used.

The Photo-Absorption Ionization Model

The Photo-Absorption Ionization (PAI) Model has been introduced by Allison[2] and Cobb in [34] and will be discussed here briefly. This model attempts to calculate $\epsilon(k, \omega)$ from the measured photo-absorption cross-section $\sigma_\gamma(\omega)$. A plane light wave travelling through a medium is attenuated if the imaginary part of the dielectric constant is non-vanishing. The wave number k is related to the frequency ω by

$$k = \sqrt{\epsilon}\omega/c \; (\epsilon = \epsilon_1 + i\epsilon_2) \tag{2.14}$$

It causes a damping factor $e^{-\alpha x}$ in the intensity where

$$\alpha = 2(\omega/c)\mathrm{Im}\sqrt{\epsilon} \approx (\omega/c)\epsilon_2 \tag{2.15}$$

The second approximation is valid if $\epsilon_1 - 1, \epsilon_2 \ll 1$ as for example in gaseous media. In terms of free photons traversing a medium that has electron density N and atomic charge Z, the attenuation is given by the photo-absorption cross-section $\sigma_\gamma(\omega)$:

$$\sigma_\gamma(\omega) = \frac{Z}{N}\alpha \approx \frac{Z}{N}\frac{\omega}{c}\epsilon_2(\omega). \tag{2.16}$$

Here α is the electric fine structure constant. The cross-section $\sigma_\gamma(\omega)$ and therefore $\epsilon_2(\omega)$ are known, for many gases, from measurements using synchrotron radiation. The real part of ϵ can be reconstructed using the Kramers-Kronig relation:

$$\begin{aligned}\epsilon_1(\omega) - 1 &= \frac{2}{\pi}\,\mathrm{Pr}\int_0^\infty dx \frac{x\epsilon_2(\omega)}{x^2 - \omega^2} \\ &= \frac{2}{\pi}\frac{Nc}{Z}\,\mathrm{Pr}\int_0^\infty dx \frac{\sigma_\gamma(x)}{x^2 - \omega^2}\end{aligned} \tag{2.17}$$

Here Pr indicates that the principal value of the integral must be taken. Quantum mechanically the (ω, k) plane represents the kinematic domain of energy and momentum exchanged between the incident particle and the medium. The exchanged photons are not free, that is they are not on the mass shell and hence relation (2.14) does not hold. The kinematic constraints

[2]W. W. M. Allison built the first large scale successful device for $\langle dE/dX \rangle$ measurements, the ISIS-detector at the EHS (European Hybrid Spectrometer), which achieved almost single electron resolution.

can be easily understood. For a free electron the constraint between transferred energy E and momentum p is simply $E = p^2/2m$, where m is the electron momentum. For bound electrons the constraint is

$$E = E_1 + \frac{(\mathbf{p}+\mathbf{q})^2}{2m} \tag{2.18}$$

Here E_1 is the binding energy and $\mathbf{q}$ is the momentum of the bound electron. In the E, p plane as shown in Figure 2.1 this traces out a rather broad region according to the magnitude an direction of $\mathbf{q}$. The band between the two thick dashed-dotted lines in Figure 2.1 consists of parts: The resonance region where $p^2/2m$ is small compared to E_1, and the quasi-free region where the constituent electron behaves almost as if it were free and stationary (Rutherford scattering). Figure 2.1 illustrates this for the case of a single shell atom with binding energy of $E_1 = 30$ MeV.

The minimum momentum transfer depends at each energy E on the velocity β, $p_{\min} = E/\beta c$, corresponding to zero degree recoil angle. This limits the kinematical domain. As β tends to one the kinematical limit almost approaches the real photon condition giving the cross section increase. At finite densities the photon condition is given by $p = E\epsilon^{\frac{1}{2}}/c$. If ϵ is greater than one the physical region may cross the photon line and Čerenkov radiation results. If ϵ is less than one, the increase of the cross section with β saturates since the physical cross section never reaches the photon line.

The PAI model consists in extending the knowledge of ϵ in the free photon case to the whole kinematical region. For small k in the resonance region below the electron line they take

$$\epsilon_2(k,\omega) = \epsilon_2(\omega) = \frac{Nc}{\omega Z}\sigma_\gamma(\omega) \tag{2.19}$$

for all k. On the free electron line, they take a δ function to represent a point-like scattering in the absorption:

$$\epsilon_2(k,\omega) = C\delta(\omega - k^2/2m). \tag{2.20}$$

The normalising constant is determined by satisfying the Bethe sum rule ([35]) for every k:

$$\int d\omega\omega\epsilon_2(k,\omega) = \frac{2\pi^2 Ne^2}{m} \tag{2.21}$$

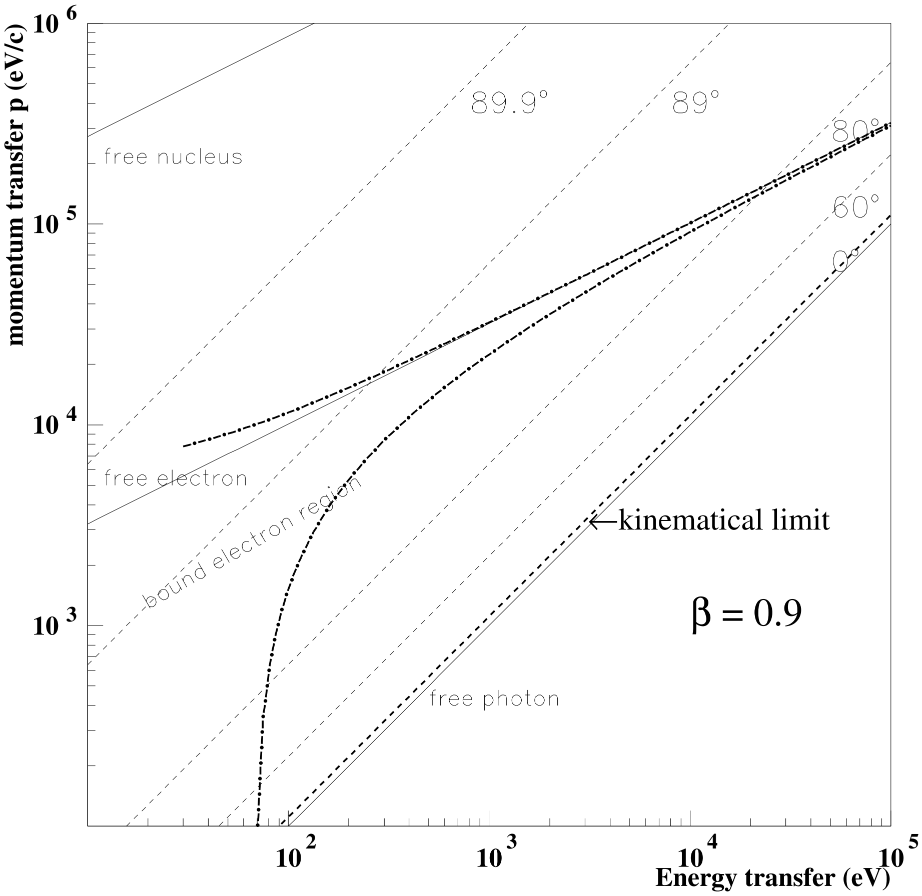

Figure 2.1: The kinematic region for soft energy and momentum transfer in natural units for $\beta = 0.9$. Dashed lines indicate the recoil angle ψ. Elastic conditions with a free stationary electron or nucleus ($A = 4$) follow the solid lines. The area between the dashed-dotted thick lines indicates qualitatively the region for collisions with a bound electron, binding energy 30eV. The energy-momentum condition for the absorption of free photons in the low density limit ($\epsilon = 1$) is also shown. The kinematical limit for the momentum transfer (at zero recoil angle) follows the thick dashed line.

The integration over k can now be performed and yields:

$$\begin{aligned}\langle \mathrm{dE/dX} \rangle = -\int_0^\infty d\omega \frac{e^2}{\pi c^2 \beta^2} \Bigg(& \frac{Nc}{Z} \sigma_\gamma(\omega) \ln \left((1-\beta^2\epsilon_1) + \beta^4 \epsilon_2^2 \right)^{-\frac{1}{2}} \\ & + \omega \left(\beta^2 - \frac{\epsilon_1}{|\epsilon|^2} \right) \Theta + \frac{Nc}{Z} \sigma_\gamma(\omega) \ln \left(\frac{2m\beta^2 c^2}{\hbar\omega} \right) \\ & + \frac{1}{\omega} \int_0^\infty d\omega' \frac{\sigma_\gamma(\omega')}{Z} \Bigg)\end{aligned} \tag{2.22}$$

where $\Theta = \arg(1 - \epsilon_1 \beta^2 + i\epsilon\beta^2)$ and in the first, third and fourth term factors proportional to $1/|\epsilon|^2$, which are unimportant for low density media have been dropped.

Finally eq. (2.22) is reinterpreted quantum mechanically in terms of the number of discrete collisions with energy transfer $E = \hbar\omega$. With N as the number of electrons per unit volume, $d\sigma/dE$ the differential cross section per electron unit energy loss, the average energy loss is given by

$$\begin{aligned}\langle \mathrm{dE/dX} \rangle &= -\int_0^\infty d\omega N E \hbar \frac{d\sigma}{dE} \\ \frac{d\sigma}{dE} &= \frac{\alpha}{\pi\beta^2} \frac{\sigma_\gamma(E)}{EZ} \ln((1-\beta^2\epsilon_1)^2 + \beta^4\epsilon_2^2)^{-1/2} \\ &+ \frac{\alpha}{\pi\beta^2} \frac{1}{N\hbar c} \left(\beta^2 - \frac{\epsilon_1}{|\epsilon_2|^2} \right) \Theta \\ &+ \frac{\alpha}{\pi\beta^2} \frac{\sigma_\gamma(E)}{EZ} \ln \left(\frac{2mc^2\beta^2}{E} \right) + \frac{\alpha}{\pi\beta^2} \frac{1}{E^2} \int_0^E dE' \frac{\sigma_\gamma(E')}{Z}\end{aligned} \tag{2.23}$$

where α is the fine structure constant. In making this substitution single photon exchange (per collision) has been assumed. This is valid for incident velocities much greater than electron orbital velocities.

The first two terms of eq. (2.23) are commonly referred to as the transverse cross section. They come from the magnetic vector potential term for which the electric field transverse to the direction of the 3-momentum transfer $\hbar\mathbf{k}$. The first term (with $\epsilon_2 = 0$) can be recognised as the factor $\ln\gamma^2$ responsible for the relativistic rise. The second term will be discussed in the next subsection.

The third and fourth terms are know as the longitudinal cross section. They come from the electrostatic term which has the electric field parallel to the momentum transfer. In the non relativistic theory these are the only terms. Their sole dependence on velocity is through the $1/\beta^2$ factor common to all terms and so they are effectively constant in the relativistic region.

Čerenkov radiation

In the limit of vanishing ϵ_2, which means that the medium is transparent, the second term of eq. (2.23) describes the emission of Čerenkov radiation; Θ jumps from near zero below Čerenkov threshold to almost π above:

$$N\left(\frac{d\sigma}{d\omega}\right)_C = \frac{\alpha}{c}\left(1 - \frac{\epsilon_1}{\beta^2|\epsilon|^2}\right) \simeq \frac{\alpha}{c}\sin^2\theta_{\check{C}} \tag{2.24}$$

This is the familiar result for the Čerenkov flux in terms of the Čerenkov angle, $\theta_{\check{C}}$. The behaviour of the intensity as a function of γ is plotted in Figure 2.2. Here the threshold expressed as $\gamma_0^2 = \epsilon_1/(\epsilon_1 - 1)$ is clearly visible.

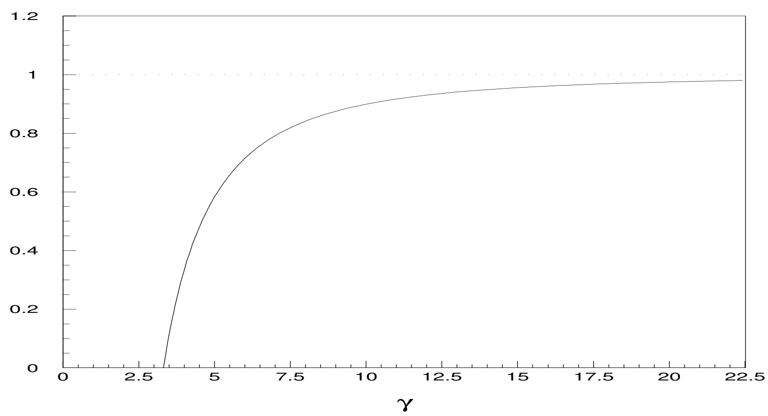

Figure 2.2: Intensity of Čerenkov radiation as a function of γ. The threshold effect is shown at the critical value $\gamma_0^2 = \epsilon_1/(\epsilon_1 - 1)$.

2.2 The Bethe Bloch formula

Historically, Bethe was the first to calculate the average energy loss using the correct quantum mechanical picture. He did this for a particle colliding with a single atom. Starting from eq. 2.13 he uses a $\epsilon(\omega)$ from a quantum-electrodynamical model to perform the integration over k. Adding the energy lost to all the atoms in the vicinity of the particle the energy loss per unit length is [35]:

$$\langle \mathrm{dE/dX} \rangle = K \left(\frac{\mathrm{MeV}}{g/\mathrm{cm}^2} \right) z^2 \frac{Z}{A} \frac{1}{\beta^2} \left(\frac{1}{2} \ln \frac{2m_e c^2 \beta^2 \gamma^2 T_{\max}}{I^2} - \beta^2 - \frac{\delta}{2} \right) \quad (2.25)$$

where

$$T_{\max} = \frac{2m_e c^2 \beta^2 \gamma^2}{1 + 2\gamma m_e/M + (m_e/M)^2} \quad (2.26)$$

is the maximum energy transfer from an incident particle of mass M to an electron. The constant $K = 2(2\pi r_e^2) m_e c^2 N_A$, where $r_e = e^2/m_e c^2$ is the classical electron radius and N_A is Avogadro's constant[3].

$T_{\max}$ can be easily understood in the ultra-relativistic limit for heavy particles, $m_e \ll M$: in the rest frame of the incident particle the electron moves with velocity $-\beta$. When the mass M is considered infinite, the change in velocity is $\Delta\beta = 2\beta$. Classically the energy transfer therefor would be $\Delta E = \frac{m_e 4c^2\beta^2}{2}$. Obviously relativistic treatment leads to $\Delta E = 2m_e c^2 \beta^2 \gamma^2$. Eq. 2.25 has been slightly rewritten from the original form. As $\beta\gamma$ increases $\langle \mathrm{dE/dX} \rangle$ first falls as $1/\beta^2$ the well know non-relativistic "Rutherford" like behaviour, then goes through a minimum and rises again for larger values of $\beta\gamma$. The logarithmic term again describes the relativistic rise. Its strength is given by the mean excitation energy I. There are two physical origins to this effect: One is the time behaviour of the electro-magnetic field carried by the travelling particle. In the rest frame of the atom, the field components of short duration become stronger as γ goes up, increasing the cross-section for the excitation and ionization. The other reason is kinematic. As $\beta\gamma$ increases the maximal possible energy which can be transferred rises as well. A pion of 1 GeV can transfer 50 MeV while a pion of 10 GeV can transfer 3.3 GeV. Such large energy transfers are usually not observed and lead to a modification which will be discussed shortly. Before it shall be mentioned that I can be calculated analytically for simple atoms, Bloch was the first to do this. For complicated ones or compounds extensive tables of measurements exist. However, care has to be taken for a correct weighting of the particular contributions and special cases like semi-conductors must be taken into account.

[3] The electron density per cm is then given by $N_A Z\rho/A$, ρ being the density of the medium. Numerically $K \approx 0.3071 \mathrm{MeV}/(\mathrm{g/cm}^2)$ Here - contrary to eq. 2.13 - the energy loss is given in terms of energy lost per unit area mass density. This has to be multiplied by the density to agree with the previous definition.

As the particle energy increases, its electric field flattens and extends, so that the distant-collision contribution increases as $\ln \beta\gamma$. Real media, however, become polarised, limiting the field extension and effectively truncating this part of the logarithmic rise. At very high energies,

$$\frac{\delta}{2} \to \ln(\hbar\omega_p/I) + \ln \beta\gamma - \frac{1}{2} \tag{2.27}$$

where $\delta/2$ is the density effect correction introduced to eq. (2.25. This was first calculated by Fermi [36]. In the limit of $\beta \to 1$ the density correction goes to

$$\delta \to \ln \frac{\hbar^2\omega_p^2}{I^2}\gamma^2 - 1 \tag{2.28}$$

where ω_o is the plasma frequency of the medium. The correction is linear in $\ln \gamma$ so it cannot cancel all of the relativistic rise. In fact it limits only the dynamical part, stemming from the electric field, but the kinematical part continues to increase the total energy loss.

Fluctuations in the energy loss are mainly due to the production of a few high energy knock-on electrons. Practical detectors often measure the energy *deposited*, not the energy *lost* in a certain range around the particle. When energy is carried off by these electrons, it is more appropriate to consider the mean energy loss excluding energy transfers above a certain cutoff T_{cut}. The restricted energy loss rate is

$$\langle \mathrm{dE/dX} \rangle \bigg|_{T<T_{\text{cut}}} = Kz^2 \frac{Z}{A}\frac{1}{\beta^2}\left(\frac{1}{2}\ln \frac{2m_ec^2\beta^2\gamma^2 T_{\text{upper}}}{I^2} - \frac{\beta^2}{2}\left(1 + \frac{T_{\text{upper}}}{T_{\text{max}}}\right) - \frac{\delta}{2}\right) \tag{2.29}$$

where $T_{\text{upper}} = \min(T_{\text{cut}}, T_{\text{max}})$. This form smoothly joins the normal Bethe-Bloch formula (eq. (2.25) $T_{\text{cut}} > T_{\text{max}}$. A more detailed discussion can be found for example in [37].

In the limit of $\beta \to 1$ there is now complete cancellation of the γ dependencies and the restricted energy loss, brought about by T_{upper}, reaches the "Fermi plateau".

The ratio between the values of the restricted energy loss on the plateau and in the minimum is given by

$$R(E_{\text{max}}) = \frac{\langle \mathrm{dE/dX} \rangle^{\text{plateau}}_{\text{restricted}}}{\langle \mathrm{dE/dX} \rangle^{\text{minimum}}_{\text{restricted}}} = \frac{\ln \frac{\sqrt{2m_ec^2E_{\text{max}}}}{\hbar\omega_p}}{\ln \sqrt{\frac{2m_ec^2E_{\text{max}}}{I}(\beta\gamma)_{\text{min}} - \frac{\beta^2_{\text{min}}}{2}}} \tag{2.30}$$

For a gas this is usually $\sim 50\%$, depending on the pressure.

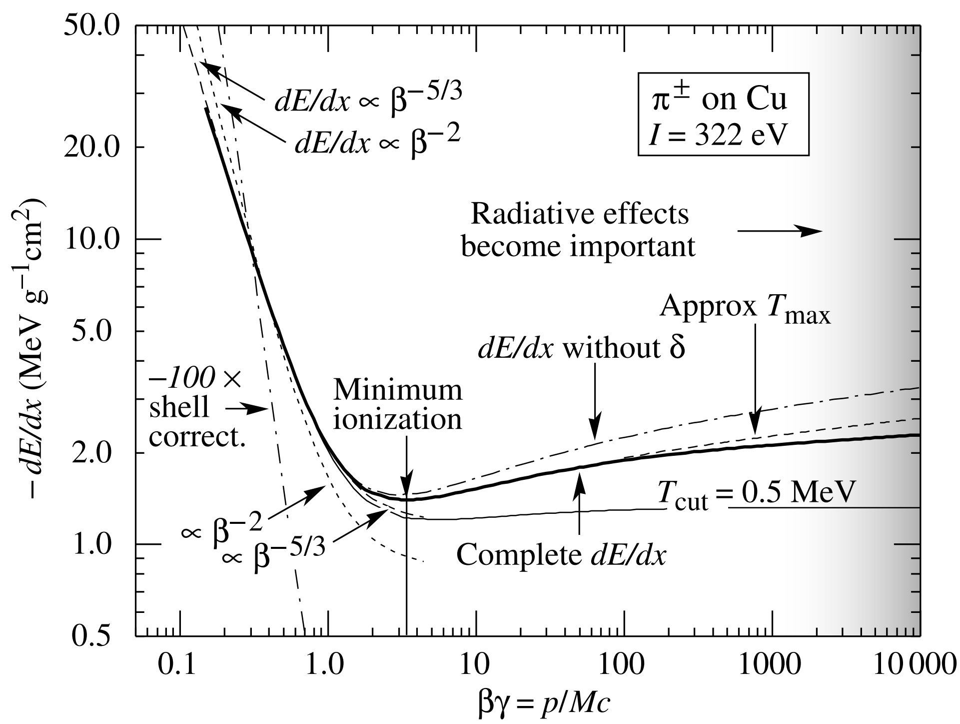

Figure 2.3: This figure from ref. [38] illustrates the various contributions of the terms in eq. (2.29) to the total energy loss. It is clear that the density correction lowers the relativistic rise and that the restricted energy loss brings about the plateau.

2.3 The energy-loss distribution

In this final section an important property of energy loss shall be briefly discussed: the statistical accuracy of the formulae for the energy loss presented before. The *average* energy-loss has large fluctuations whereas the *most probable* energy-loss is much more stable. The problem was first described by Williams in 1929 [39]: the probability density function $F(x, \Delta)$ of energy loss Δ by particles of given velocity traversing a thickness of material x is uniquely determined by the cross section $d\sigma/dE$ and the number of electrons in the layer Nx. N is the spatial density of electrons. Since $d\sigma/dE$ has a significant value over a wide range of E the distribution, $F(x, \Delta)$ is both broad and skew.

Two basic methods have been proposed to tackle this problem, the convolution method and the Laplace transform method.

The convolution method considers a very small thickness δx such that the chance of two collisions within δx is negligible. Then

$$F(\delta x, \Delta) = (1-\tau)\delta(\Delta) + N\delta x \frac{d\sigma}{dE}(\Delta) + O(\tau^2) \tag{2.31}$$

where τ, the probability of one collision, is $N\delta x \int_0^\infty dE d\sigma/dE$. From the result for an arbitrary thickness can be constructed by

$$F(2x, \Delta) = \int_0^\Delta dE F(x, \Delta - E) F(x, E) \tag{2.32}$$

where the fact that the energy loss in different layers is statistically independent has been used. Bichsel & Saxon follow this method [40]. The integral bounds come about by the fact that $F(x, -E) = 0$ for $E \geq 0$, since there can be only positive energy transfer. Alternatively the folding can be done by a Monte Carlo method.

The Laplace transform was introduced by Landau [41]. He considered the change in $F(x, \Delta)$ as a result of passing through a thin elemental layer δx:

$$F(x + \delta x, \Delta) - F(x, \Delta) =$$

$$= -N\delta x \int_0^\infty dE \frac{d\sigma}{dE}(E) F(x, \Delta) + N\delta x \int_0^\Delta dE F(x, \Delta - E) \frac{d\sigma}{dE}(E) \tag{2.33}$$

The absolute value of the first term describes the probability that the energy loss was already equal to Δ before entering δx where a further collision increased the energy beyond Δ. The second term corresponds to the case in which the energy loss at x was $\Delta - E$ but a collision with energy E occurred in the element δx. This may be cast in the form of a transport equation:

$$\frac{\partial F}{\partial x}(x, \Delta) = \int_0^\infty dE N \frac{d\sigma}{dE}(E)(F(x, \Delta - E) - F(x, \Delta)) \tag{2.34}$$

This may be solved by taking the Laplace transform of both sides with respect to Δ and solving for the transform $\bar{F}(x, s)$ of $F(x, \Delta)$. Inverting the Laplace transform yields

$$F(x, \Delta) = \frac{1}{2\pi i} \int_{-i\infty+\sigma}^{i\infty+\sigma} ds \exp\left(s\Delta - x \int_0^\infty dE N \frac{d\sigma}{dE}(E)(1 - e^{-sE}) \right) \tag{2.35}$$

Here σ is a small but positive constant.

This result is exact but suffers from the fact that the cross section in realistic models is far from simple and the integration has to be carried out numerically. Landau used a simplified ansatz for the cross section

$$\frac{d\sigma}{dE}(E) = \frac{2\pi r_e^2}{\beta^2}\frac{mc^2}{E^2}N \tag{2.36}$$

He was then able to show that the probability distribution was given by a universal function$\phi(\lambda)$:

$$F(x,\Delta)d\Delta = \phi(\lambda)d\lambda \tag{2.37}$$

where $\lambda = \frac{\Delta-\Delta_{\mathrm{mp}}}{\xi}$. Here Δ_{mp} is the most probable energy loss and ξ is a scaling factor for the energy loss proportional to x.

This function has the property:

$$F(x_1+x_2,\Delta) = \int_0^{\Delta} dE_2 F(x_1,\Delta-E_1)F(x_2,E_2) \tag{2.38}$$

which is required for universal functions. The price to be paid is that no moments exist any more. Thus there is no additivity of means. If one restricts the integral, the moments become finite, but the Laplace transform can not be performed any longer and hence the universality property is lost. This is discussed in ref. [42].

The assumption eq. (2.36) restricts the validity of the Landau curve description to a regime of large Δ (corresponding to $x \approx 170$ cm in argon). However it is often used to parametrise energy loss distribution with a two-parameter fit of ξ and Δ_{mp}, regardless of the theoretical implications.

Figure 2.4 shows a fit of the Landau curve to the energy loss distribution in the DELPHI silicon vertex detector.

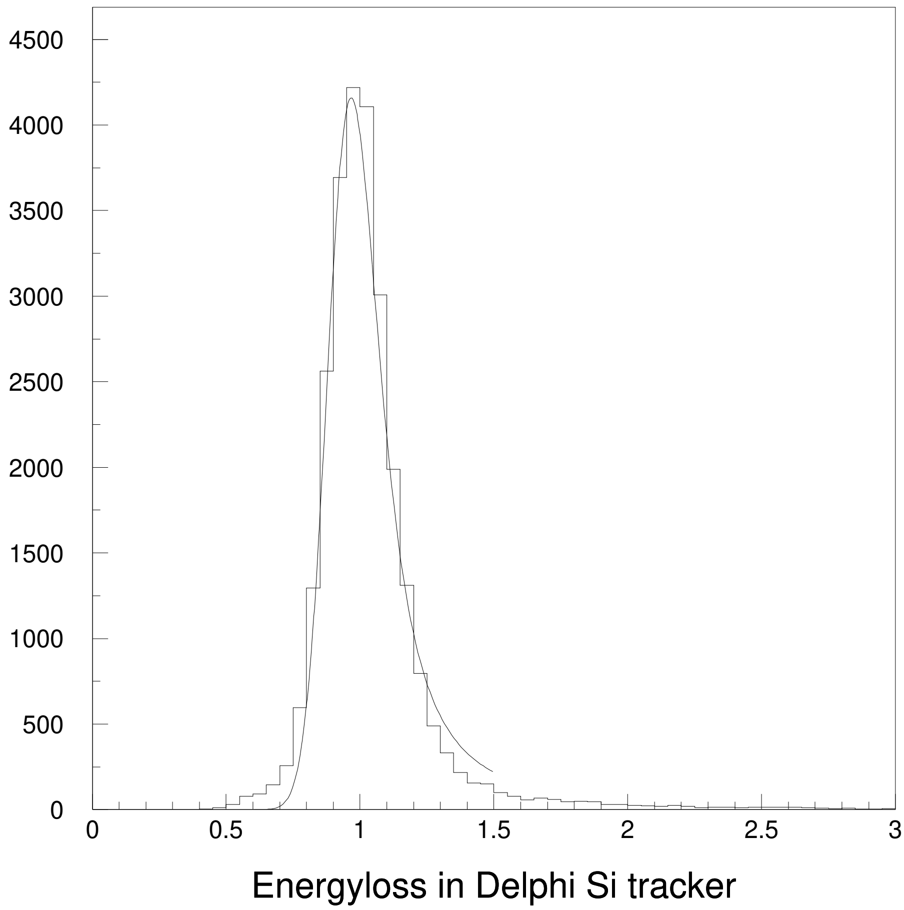

Figure 2.4: Landau distribution fitted to the energy loss distribution from the DELPHI silicon tracker (6 layers hit). Data from 1994 have been taken with 0.5 GeV/c $\leq p \leq$ 1 GeV/c

Chapter 3

Particle identification detectors

This chapter will briefly describe the general features of detectors used for hadron identification in this work, namely RICH and TPC. While this discussion will be general, the details for DELPHI will be given in the next chapter. More information and an extensive bibliography can be found in ref. [38]. There, also other methods like transition radiation detectors are discussed.

3.1 Čerenkov detectors

Čerenkov detectors utilise one or more properties of Čerenkov radiation discussed shortly in chapter 2.

1. The existence of a threshold for radiation
2. The dependence of the Čerenkov cone half angle $\theta_{\check{C}}$, on the velocity of the particle
3. The dependence of the number of emitted photons on the particle's velocity

The (energy dependent) refractive index is the main experimental parameter, which can be tuned by choice of the medium, pressure and temperature to fit a desired range for the measurement. The most important formula which, follows straight forward from eq. (2.24), is the number of photoelectrons (p.e.'s) detected in a given device or channel:

$$N_{\text{p.e.}} = L \frac{\alpha^2 z^2}{r_e m_e c^2} \int dE \epsilon_{\text{coll}}(E) \epsilon_{\text{det}}(E) \sin^2 \theta_{\check{C}}(E) \tag{3.1}$$

where L is the path length in the radiator, ϵ_{coll} is the efficiency for collecting the Čerenkov light, ϵ_{det} is the quantum efficiency of the transducer (photomultiplier or equivalent), and $\alpha^2/(r_e m_e c^2) = 370\ \text{cm}^{-1}\text{eV}^{-1}$. All terms in the integral are functions of the photon energy E; In many cases the energy dependence of n or equivalently of $\theta_{\check{C}}$ is small. Then eq. (3.1) simplifies to:

$$N_{\text{p.e.}} \approx L N_0 \langle \sin^2 \theta_{\check{C}} \rangle \tag{3.2}$$

with

$$N_0 = \frac{\alpha^2 z^2}{r_e m_e c^2} \int dE \epsilon_{\text{coll}}(E) \epsilon_{\text{det}} \tag{3.3}$$

In the following z, the charge of the incident particle is taken to be one.

Threshold Čerenkov detectors make a simple yes/no decision based on a particle being above/below the Čerenkov threshold velocity $\beta_t = 1/n$, which is the velocity of light in the medium.

Differential Čerenkov detectors try to exploit the dependence of $\theta_{\check{C}}$ on β, using optical focusing and/or geometrical masking to select particles, which have velocities in a specified range. A velocity resolution of $\sigma_\beta/\beta \approx 10^{-4}$ can be achieved.

Ring-Imaging Čerenkov detectors use all three velocity dependencies of Čerenkov radiation simultaneously. They are principally used as hypothesis testing rather than yes/no devices. The probability of various identification possibilities is established from $\theta_{\check{C}}$ and $N_{\text{p.e.}}$ for a particle of known momentum. In most cases they optically map the Čerenkov cone onto a circle on the photon detector. Thereby distortions can arise, which have to be understood.

The 4π devices operated nowadays at DELPHI and SLC typically have both liquid (i.e. high n) and gas (low n) radiators to cover the full momentum range. Figure 3.1 shows the principle of the mirror focusing. The details of the DELPHI detector will be discussed in the next chapter.

3.2 Time Projection Chambers

Of course a Time Projection Chamber (TPC) is not primarily a particle identification device. This short reminder on its principles will however focus on the properties relevant for this purpose. Clearly the excellent momentum reconstruction achieved by tracking devices like TPCs is a crucial input for particle identification with RICHes.

A TPC is a detector with a long drift distance perpendicular to a multi-anode proportional plane. It provides three-dimensional information, with one being he time projection, hence the name. A (usually strong) magnetic field parallel to the drift direction suppresses transverse diffusion ($\sigma = \sqrt{2Dt}$) by a factor

$$D(B)/D(0) = \frac{1}{1 + \omega^2 \tau^2} \tag{3.4}$$

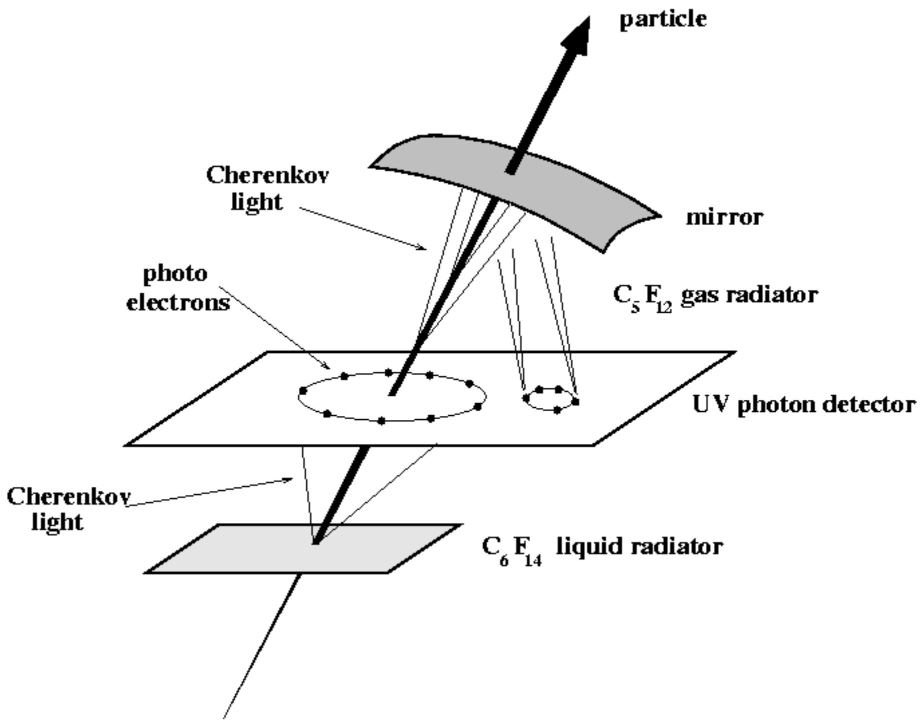

Figure 3.1: The principle of a ring imaging Čerenkov detector: A charged particle traverses a dielectric medium and emits Čerenkov photons on a cone given by $\cos(\theta_{\check{C}}) = 1/n\beta$. It passes a first radiator whose light is directly mapped to a photon detector plane, then traverses a second medium where light-cone is focused back onto the photon detector plane by means of a mirror. The famous $R/2$ condition states that a spherical mirror of radius R will focus the Čerenkov cone onto a sphere with $r = R/2$.

where D is the diffusion coefficient, $\omega = eB/m_e c$ is the cyclotron frequency, and τ is the mean time between collisions. It should be noted that it is only this effect which makes possible the operation of devices extending over several meters. A typical gas-filled TPC consists of a long uniform drift region (1-2 m) generated by a central high-voltage membrane and precision concentric cylindrical field cages with a uniform, parallel magnetic field. Signal shaping and processing using Flash ADC's allow excellent pattern recognition, track reconstruction and particle identification with the same detector. However, this is still quite far from single electron counting. Therefor one has to stay carefully in the proportional region, which requires the detailed understanding of a lot of subtle effects such as: angle w.r.t the sense wire, angular distorsion due to the magnetic field (which is not orthogonal to the electron cloud), linearity of read-out electronics, cut-off in the measurements by the pattern recognition, shape of the cathodes, etc.

Figure 3.2 is an example of the mass separation power achieved in modern TPCs[1].

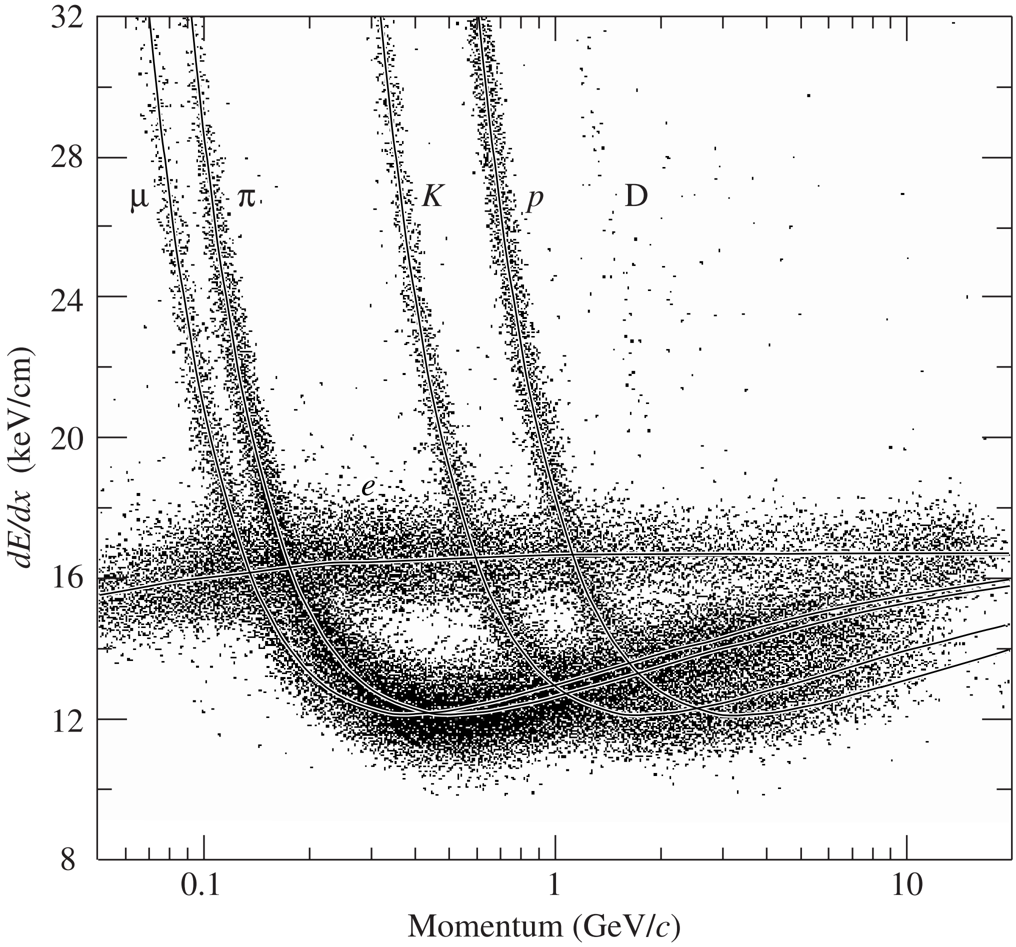

Figure 3.2: This figure shows the mass separation achieved with a modern Time Projection Chamber (from ref. [38]).

A drift chamber like the TPC usually provides multiple measurements of the ionization loss. The most straight forward estimator for the strength of ionization in each cell is the average of the n measurements. This is a bad choice because the separation becomes bad due to the large skewness of the

[1]It should be stressed here, that separation power can not be directly mapped to the purity of the particle identification, because of the very different primary populations.

ionization distribution. A better estimator is derived from a fit to the shape of the measured distribution or from a sub-sample excluding the very high measured values. This simplified method is also called the "truncated mean". It is characterised by a cut-off parameter η between 0 and 1. The estimator is then given by the average signal strength of the ηn lowest values among the n signals. The optimal choice can be obtained from Monte Carlo simulations. Typically η ranges between 0.35 and 0.75. In this region the shape of the ionization loss is almost Gaussian. Truncated $\langle \mathrm{dE/dX} \rangle$ resolution depends on the number and size of samples, and gas pressure

$$\sigma_{\langle \mathrm{dE/dX} \rangle} \approx N^{-0.43} \times (P\ell)^{-0.32} \tag{3.5}$$

Here N is the number of samples, ℓ is the sample size, and P is the pressure.

Because of its simplicity this is the method of choice in many experiments. In principle the *likelihood* method which directly differentiates between two hypothesis as

$$\mathcal{L} = \prod_{i}^{n} F_1(\Delta_i)/F_2(\Delta_i) \tag{3.6}$$

should give superior results. Here F_1 and F_2 are the theoretical pulse height distributions for masses m_1 and m_2 respectively and the Δ_i are the measurements. Allthough it is preferable in the case of limited number of measurements, in practice it does not give much better results, than the "truncated mean"[2].

[2] In addition to the requirement of a very detailed modelling and understanding of all the effects mentioned before, the evaluation becomes computationally much more expensive.

Chapter 4

The DELPHI experiment

DELPHI (DEtector with Lepton, Photon and Hadron Identification) is a detector for e^+e^- physics, designed to provide high granularity over a 4π solid angle aiming at full hermeticity, allowing an effective particle identification. It has been operating at the LEP (Large Electron-Positron) collider at CERN since 1989. This chapter will briefly review its design and performance. Special emphasis will be put on the parts which are necessary in the context of this work. A detailed description can be found in reference [43]. The discussion of the RICHes follows [44].

4.1 Overview

In the standard DELPHI coordinate system, the z axis is along the electron direction, the x axis points towards the centre of LEP, and the y axis is chosen to give a right-handed orthonormal system. The polar angle towards the z axis is called θ and the angle around the z axis is denoted by ϕ. The detector consists of a cylindrical section covering the so-called "barrel" region ($40° \leq \theta \leq 140°$) and two endcaps covering the "forward" region. Figure 4.1 shows a schematic layout of the barrel and one endcap. The superconducting[1] solenoid provides a uniform magnetic field of 1.23 T parallel to the z axis throughout the central tracking volume containing the barrel tracking detectors, the vertex detector (VD), the inner detector (ID), the Time Projection Chamber (TPC) and the Outer Detector (OD) and also the forward tracking chambers (Forward Chambers A and B). Electron and photon identification is provided primarily by the High density Projection Chamber (HPC) in the barrel region and by the Forward Electromagnetic Calorimeter (FEMC). The smaller polar angles are covered by the Small-

[1] The super-conductivity is required to avoid intolerable heat dissipation.

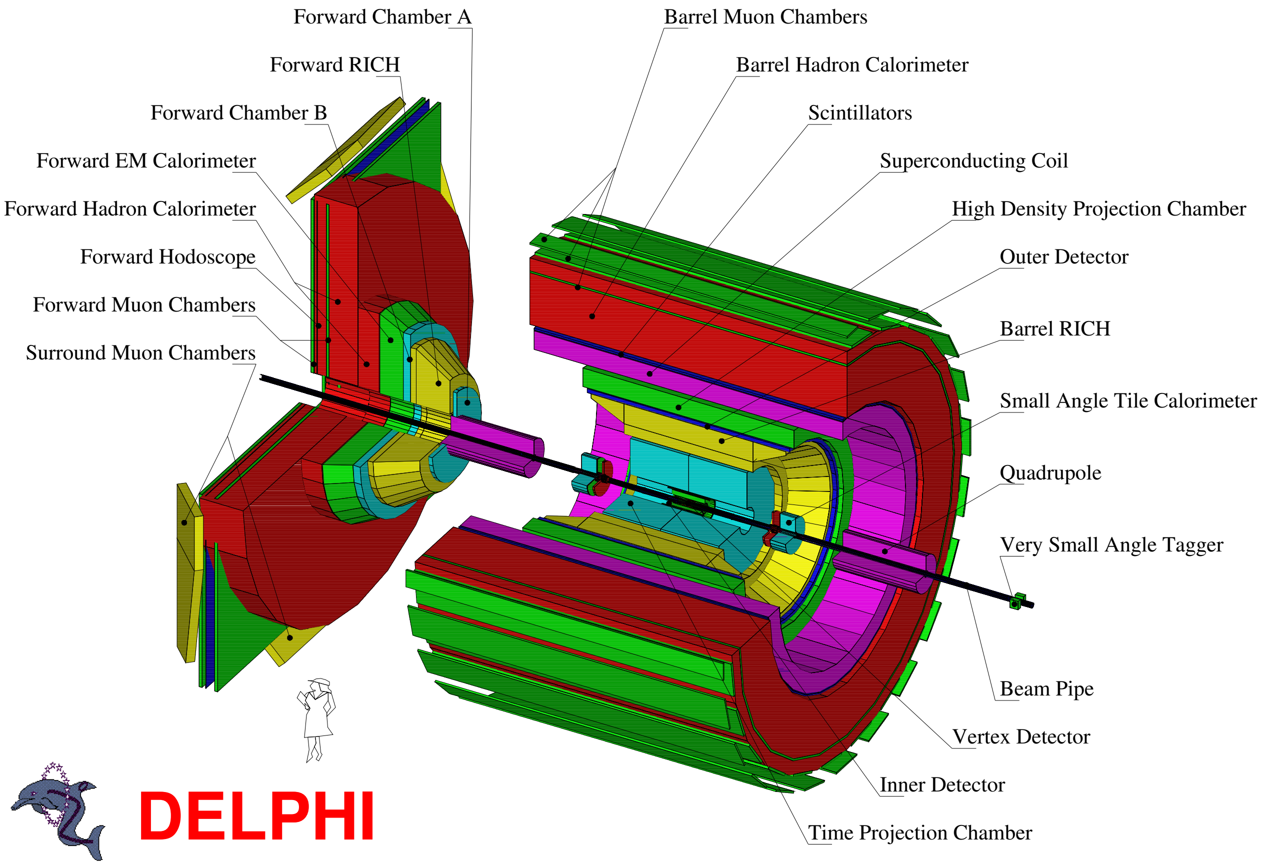

Figure 4.1: Schematic drawing of the DELPHI detector.

angle Tile Calorimeter (STIC) and the Very Small Angle Tagger (VSAT). In order to achieve complete hermeticity for high energy photon detection, additional scintillators have been installed in the cable duct regions between the barrel and the endcap and in the small gaps between the HPC modules. The iron return yoke of the magnet is instrumented with limited streamer mode detectors to create a sampling gas calorimeter, the Hadron Calorimeter (HAC). Muon identification is achieved by comparing extrapolations of the reconstructed tracks with the hits in the Barrel (MUB) and Forward (MUF) muon drift chambers. An additional system of limited streamer mode tubes was installed outside the endcaps to fill the gap between forward and barrel regions, these are called surround muon chambers (MUS).

DELPHI has a three level trigger system with a typical dead-time of $1-2\%$ for the first two stages and an average read-out time of 3 ms per event. The efficiencies for hadronic events is practically 1, and even for single charged tracks with $p > 1$ GeV/c exceeds in general 95%. For single photons the efficiency is energy dependent, rising from 50% for 1 GeV photons to 60% for photons with energies greater than 4 GeV.

4.2 Tracking

The tracking is achieved by a relatively large number of subdetectors whose main characteristics and performances shall be reviewed here.

Vertex Detector

The VD consists of three coaxial cylindrical layers of AC coupled silicon strip detectors at average radii of 6.3, 9.0 and 10.9 cm, respectively. Each layer covers the full azimuthal angle in 24 sectors with overlaps between adjacent sectors. There are four detectors along the beam direction in each section. For polar angle of $44° \leq \theta \leq 136°$, a particle crosses all three layers of the VD. The readout pitch is 50 μm in the $R\phi$ plane perpendicular to the beam direction. The resolution in the $R\phi$ plane is typically 10.3 μm and in the z plane 13 μm.

Inner Detector

The inner drift chamber of the ID has a jet-chamber geometry with 24 azimuthal sectors, each providing up to 24 $R\phi$ points per track. Surrounding the jet-chamber, there are 5 cylindrical layers of straw tube detectors measuring $R\phi$. The polar angle coverage is $15° \leq \theta \leq 165°$. The two track resolution is about 1 mm and the precision in $R\phi$ and ϕ are 40 μm and 0.89 mrad respectively.

Time Projection Chamber

Both end plates of the TPC are divided into six azimuthal sectors, which are slightly excentric[2] each with 192 sense wires and 16 circular pad rows with constant spacing. The detector thus provides up to 16 space points per particle trajectory at radii from 40 to 110 cm for polar angles $39^\circ \leq \theta \leq 141^\circ$. The detector is operated with a gas mixture of 80% Ar and 20% CH_4 stabilised to one atm with a drift field of 187 V/cm. The single point precision is about 250μm in the $R\phi$ plane and 880 μm in the Rz plane, for maximal z. The two point resolution is about 1 cm in both directions. The successfull operation depends crucially on the parallel B-field, as mentioned in the previous chapter.

Outer Detector

The OD consists of five layers of drift tubes, operated in limited streamer mode, located between radii of 197 and 206 cm. Successive layers are staggered and adjacent modules of 24 azimuthal sectors overlap, giving full azimuthal coverage. Three layers are equipped to read the z coordinate as well. The detector covers polar angle from 42° to 138°. The resolution obtained for single points is 110 μm in $R\phi$ and 3.5 cm in z.

Forward Chamber A

FCA is streamer tube matrix, consisting of three modules, which are mounted on each end of the TPC at a distance from the interaction point of about 160 cm in $|z|$. A module consists of two staggered layers of drift tubes, operated in limited streamer mode. There is a rotation of 120° between the wire orientations of the modules. The chamber covers polar angle $11^\circ \leq \theta \leq 32^\circ$ and $148^\circ \leq \theta \leq 169^\circ$. The resolutions in x and y are 290 μm and 240 μm respectively. The angular resolutions in θ and ϕ are 8.5 mrad and 24 mrad.

Forward Chamber B

FCB is a drift chamber at an average distance of 275 cm from the interaction point. The chamber consists of 12 readout planes, coordinates in each of three

[2] This is referred to by the beautiful name "géometrie de fleurs".

directions rotated by 120°. It covers the polar angle region $11° \leq \theta \leq 36°$ and $144° \leq \theta \leq 169°$ respectively. The precisions achieved on the reconstructed track elements are $\sigma(x, y) = 150\mu\mathrm{m}$, $\sigma(\theta) = 3.5$ mrad and $\sigma(\phi) = 4.0/\sin\theta$ mrad.

Performance

The momentum resolution for di-muon events has been measured to be

$$\sigma(1/p) = 0.57 \times 10^{-3}(\mathrm{GeV/c})^{-1}$$

in the barrel and

$$\sigma(1/p) = 1.31 \times 10^{-3}(\mathrm{GeV/c})^{-1}$$

in the endcap (forward) region. For high-momentum di-muons multiple scattering is small and $\sigma(1/p)$ is constant, that is $\sigma(p)/p = \mathrm{const}p$. The impact parameter resolutions obtained with the VD are

$$\sigma_{R\phi}^2 = \left(\frac{65}{p\sin^{\frac{3}{2}}\theta}\right)^2 + (20\mu\mathrm{m})^2 \sigma_z^2 = \left(\frac{71}{p\sin^{\frac{5}{2}}\theta}\right)^2 + (17\mu\mathrm{m})^2.$$

The impressive performance of the VD is illustrated in Figure 4.2, which shows the *significance*, that is the ratio of signed impact parameter and resolution, $S_R = \delta_R/\sigma_R$ and $S_Z = \delta_Z \sigma_Z$.

4.3 Charged Hadron Identification

Specific Ionization in the TPC

The sense wires of the proportional chambers of the Delphi TPC provide up to 192 ionization measurements per track. This amount of wires yields almost the quality of single electron counting, 30 primary electrons per cm being the (statistical) limit. The signals collected by the sense wires are associated to the tracks reconstructed by the TPC pads. This association is done by comparing the arrival times of the pad and sense wire signals. Hits too close in time to be correctly separated are not used for the $\langle \mathrm{dE/dX} \rangle$ calculation. This corresponds to a separation of at least 2 cm for tracks orthogonal to the drift direction. Sense wire signals with a width incompatible with a single track are removed. On average 5% of the signals are below electronic threshold. To reduce dependence on drift length and gap size (wire spacing as seen by the track) an effective threshold is applied. This results in a

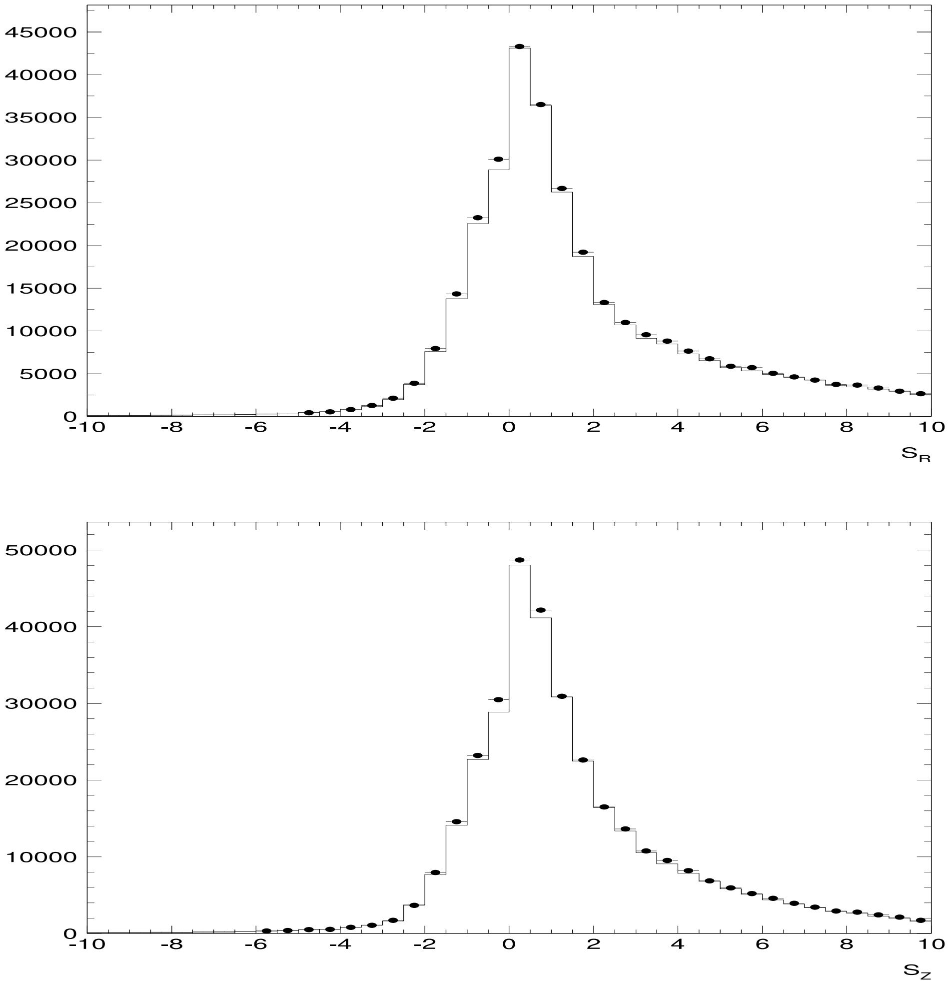

Figure 4.2: Signed significance S_R in $R\phi$ (upper) and S_Z in Rz (lower). B tagged events from 1994 DELPHI data compared to DELPHI tuned simulation. The agreement is excellent. The worse resolution in z is compensated by the effective cancelling of the curvature dependence for this direction. The details of the technique for obtaining the impact parameters and their calibration can be found in reference [45]. The figures are due to the courtesy of F. Tegenfeldt.

loss of the lowest $\sim 8\%$ of measurements. The highest 20% are removed to reduce the influence from the Landau tail. After this cuts only 2% of the signals produced by electrons on the plateau are still saturated. This cut also increases the relative height of the Fermi plateau, thus increasing by 10% the separation between particles on the Fermi plateau and minimum ionising particles. In the analysis only tracks with at least 30 contributing measurements are used. This results in an efficiency for tracks with $p < 1$GeV ($p > 1$GeV) in multi hadron events of 82% (61%) in the barrel and 78% (67%) in the endcap region. The value of the Fermi plateau, normalised to the minimum ionising particle, is found to be 1.52 units, where unity corresponds to the value for a minimal ionizing particle, and for particles in jets the average separation for π and K is above the 1σ level for momenta above 2 GeV/c.

From the last paragraph it is clear, that the particle identification by the TPC needs to be improved, especially for high momentum particles. This where the next detector system comes into play.

Ring Imaging Cherenkov Detectors

DELPHI comprises a system of RICHes for hadron identification. Generally a RICH system will be applied, when separation of charged particles over a wide momentum range is needed. For high momentum particles a thin medium is needed, which has a low photon yield per unit track length. Therefor the radiator has to be as large as possible and mirrors are needed to focus the image back onto the photon detector. For low momentum particles an optically dense medium is needed, which has naturally a high photon yield, but multiple scattering limits demands that this radiator is only a thin layer.

The two Forward RICH (FRICH) detectors cover the polar angular ranges $15° \leq \theta \leq 35°$ and $145° \leq \theta \leq 165°$, the Barrel RICH (BRICH) covers the central region between 42° and 138° . In this way 94% of the full solid angle are covered. In order to cover the full momentum range at LEP each of the detectors is equipped with a dual radiator system: a C_6F_{14} liquid radiator of 1 cm thickness and a gas radiator volume. In the Barrel RICH gaseous C_5F_{12} is used with an average path length of 45 cm. In the Forward RICH C_4F_{10} is used and the average path length is about 60 cm. The Čerenkov light is detected by TPC-type photo detectors in which TMAE (TetrakisdiMethylAminoEthylene) is used as the photosensitive agent. The total photo sensitive area is about 36.5 m^2. The reconstruction of the Čerenkov angle requires a precise knowledge of the trajectory of the charged particle , which is the reason that the RICHes are enclosed on both sides by tracking devices, as can been seen in Figure 4.1.

The Forward RICH Detectors

The two FRICHes (see left part of Figure 4.3) consist of 24 azimuthal sectors. A charged particle first traverses one of 3 liquid radiator trays of 1 cm thickness which are filled with C_6F_{14}. The exit windows consist of UV-transparent fused quartz plates. The emitted Čerenkov light cone is directly mapped to one of the TPC like photon detectors, this is called proximity focusing. An arrangement of 5 spherical mirrors focuses the Čerenkov light generated in the C_4F_{10} gas volume onto the same photo-detector. The TPC detectors consist of two tapered quartz boxes through which Ethane is circulated. TMAE is admixed at 24°C. The drift field ($E = 1$ kV/cm) inside the drift-boxes from the mid-plane towards the MWPC's is defined by a set of strips on the quartz plates and field-wires. The drift-field is orthogonal to the DELPHI magnetic field which results in a Lorentz angle of $\sim 50°$. The wire chambers, which are locate at the radial edges of the drift-boxes are equipped with anode wire and cathode strip readout. Both radiators and the drift volumes are operated at atmospheric pressure at a temperature of ~ 30°C.

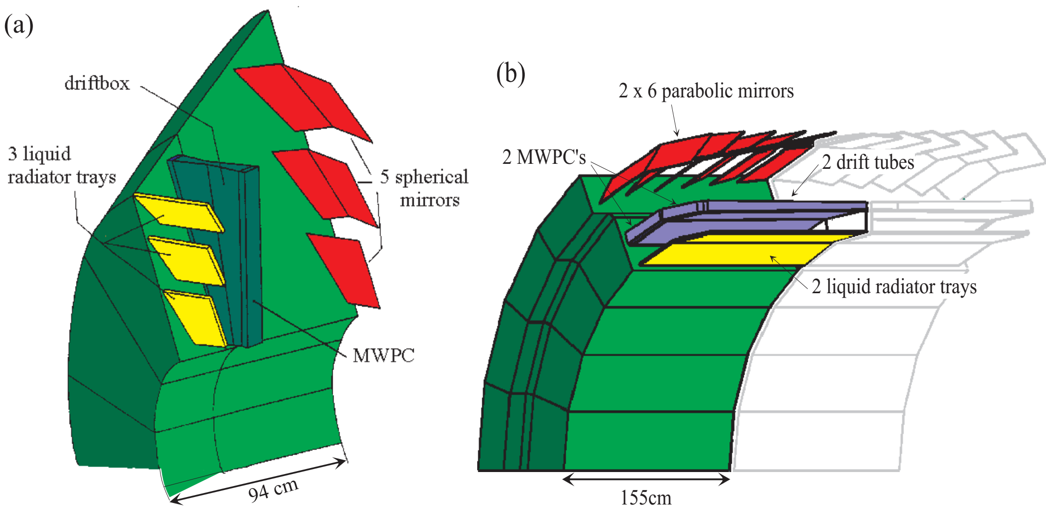

Figure 4.3: Main components of the RICH detectors as explained in the text. Left: Forward RICH. Right: Barrel RICH.

Barrel RICH Detector

The Barrel RICH detector (right-hand part of Figure 4.3) consists of a cylindrical arrangement of 2×12 azimuthal sectors. A full sector includes two liquid radiator trays of 1 cm thickness, filled with C_6F_{14}. Like in the Forward RICH, the Čerenkov light passes through the quartz exit windows and is detected by a TPC photo-detector using proximity focusing. Each sector is furthermore equipped with two rows of six parabolic mirrors, which focus the Čerenkov light generated in the gas radiator volume onto the photo-detector. The complete BRICH volume is heated to 40° to avoid condensation of the C_5F_{12} gas, which has a boiling point $T_b = 28°$C. The photo-detector consists of two tapered quartz drift-boxes and it is operated with a mixture of 75% Methane and 25% Ethane. TMAE is admixed at 28°C. All 24 sectors together form a single gas radiator volume of about 24m^3 and share a single mid-wall potential plane (-54 kV) for the drift voltage. The drift field ($\approx$ 360V/cm) from the mid-wall to the wire chambers is parallel to the DELPHI magnetic field. This reduces the transverse diffusion along drift path of the electrons, which can be up to 1.5 m long. The gas radiator volume is kept at a constant pressure of 1030 mbar. The liquid radiator trays are maintained at 45 mbar below this pressure, in order to compensate the maximum hydrostatic pressure of C_6F_{14}.

For good particle identification performance it is essential to have excellent stability and continuous monitoring of all these components. The long drift paths for example require a precise knowledge of the drift velocity and of the Lorentz angle in the case of the FRICH. An elaborate system of controls and calibrations is used to ensure this quality. This is described in greater detail in ref. [44].

The dedicated RICALI and RICFIX software-packages are used for the alignment of the RICHes and the improvement of the data/simulation agreement. RICFIX fine-tunes the simulation with a special emphasis on detector related effects, such as slight fluctuations in pressures and refractive indices, background arising from photon feedback, crosstalk between the MWPC readout strips, δ-rays, track ionization photoelectrons, etc.

4.4 Particle Identification Algorithms

Several particle identification algorithms have been developed for RICH detectors operated at SLC (Stanford Linear Collider) and DELPHI and also for the new RICH detectors planned in forthcoming B-physics experiments. Basically two methods may be discerned. First there are methods which treat a whole event using all availiable information to assign masses to all particles. This is usually done using a Likelihood based method. A continuous estimator of the observed Čerenkov photons and the background photons is needed. In principle this should give the most powerfull identification possible, if one has a very good modelling of the signal and background shape. A very general form of this approach has been developed in ref. [46].

In DELPHI the program package HADSIGN tries to fit a flat background and does not try to separated it from the signal. For each mass hypothesis, the expected signal is known. The flat background is then adjusted such as to maximise the likelihood. The likelihoods corresponding to the known particle types are then used for tagging.

Another approach which has been used in the present work tries, to assign photons to individual tracks and subsequently to reconstruct the corresponding Čerenkov angle. It works on the basis of a single charged track and tries to reconstruct a Čerenkov angle for the track.[3]

This is the method of the RIBMEAN package, which is described in [47]. In short, the algorithm proceeds as follows: Starting with a reconstructed charged particle track, ionization from the charged track itself and noisy cluster are removed. This reduces the background in the liquid radiator, where the number of photo-electrons is four times larger. Then the Čerenkov angles are sorted w.r.t. the five hypothesis $(el, \mu, \pi, \mathrm{K}, \mathrm{p})$. The first photon is taken as a seed and the other photons are iteratively tested against forming a cluster by requiring $|\theta^i_{\check{C}} - \theta_{\check{C}}| < 2.5\sigma_{\theta^i_{\check{C}}}$ where $\theta_{\check{C}}$ is the mean Čerenkov angle, $\theta^i_{\check{C}}$ is the Čerenkov angle for photon i and $\sigma_{\theta^i_{\check{C}}}$ is the expected error on the Čerenkov angle. The same procedure is repeated for all mass hypotheses. Finally, the cluster with the largest number of associated photons is selected. The *mean* Čerenkov angle and its error are calculated as:

$$\theta_{\check{C}} = \frac{\sum_{i=1}^{n} w_i \frac{\theta^i_{\check{C}}}{\sigma^2_{\theta^i_{\check{C}}}}}{\sum_{i=1}^{n} w_i / \sigma_{\theta^i_{\check{C}}}} \tag{4.1}$$

$$\sigma_{\theta_{\check{C}}} = \frac{1}{\sqrt{\sum_{i=1}^{n} w_i / \sigma^2_{\theta^i_{\check{C}}}}} \tag{4.2}$$

where n is the number of associated photons and w_i is the weight per photon. Weights are introduced to reduce the background and improve the resolution of the mean Čerenkov angle. They are computed as a function of the photon quality, the number of ambiguous photons and the liquid ring area. Ambiguous photons are photons which can be assigned to more than one track. These are resolved in two steps. First using the measured conversion depth they are assigned to either the liquid or the gas radiator. Secondly one uses the association to a selected cluster, the number of photons in the rings and the χ^2 contribution to each ring.

[3]The first class of methods is sometimes called “global” and the second “local”.

After this procedure the Čerenkov angle, its expected error and the number of photons are ready for use in particle identification algorithms.

The advantage of this per track methods lies in the improved understanding of the detector response. Subtle effect as time dependent shifts of the refractive index or the drift velocity can be well studied using the average angles and errors. These quantities are used to fine-tune the simulation of the RICH detectors.

After all these corrections have been applied particle identification is in principle straight forward. Likelihoods are defined for each mass hypothesis $i = \mathrm{e}, \pi, \mu, \mathrm{K}, \mathrm{p}$ as

$$P(i) = (n_i)^n \frac{\exp(-n_i)}{n!} \times \frac{1}{\sqrt{2\pi}\sigma_{\theta_{\check{C}}}} \exp\left(-\frac{(\theta_{\check{C}} - \theta^i_{\check{C}})^2}{2\sigma^2_{\theta_{\check{C}}}}\right)$$

where $P(i)$ is a product of Poissonian and Gaussian probability density functions respectively for n observed photons at a Čerenkov angle $\theta_{\check{C}}$ with an error of $\sigma_{\theta_{\check{C}}}$ and an expected number of photons n_i and Čerenkov angle $\theta^i_{\check{C}}$. In this formula the averaged angle and the averaged number of photons are used.

The combination of gas and liquid is achieved by simply multiplying the likelihoods for the two independent measurements. The information from the specific ionization loss, $\langle \mathrm{dE/dX} \rangle$ calculated from the truncated mean can also be incorporated using a Gaussian. From these total likelihoods *tags* are constructed, which are integer numbers between zero and three. They correspond to an increasing separation between neighbouring hypotheses.

Figure 4.4 demonstrates the separation power achieved by this method for $\mathrm{K}^{\pm}$ in high energy hadronic events. The measurements described in the rest of this work rely on this algorithm.

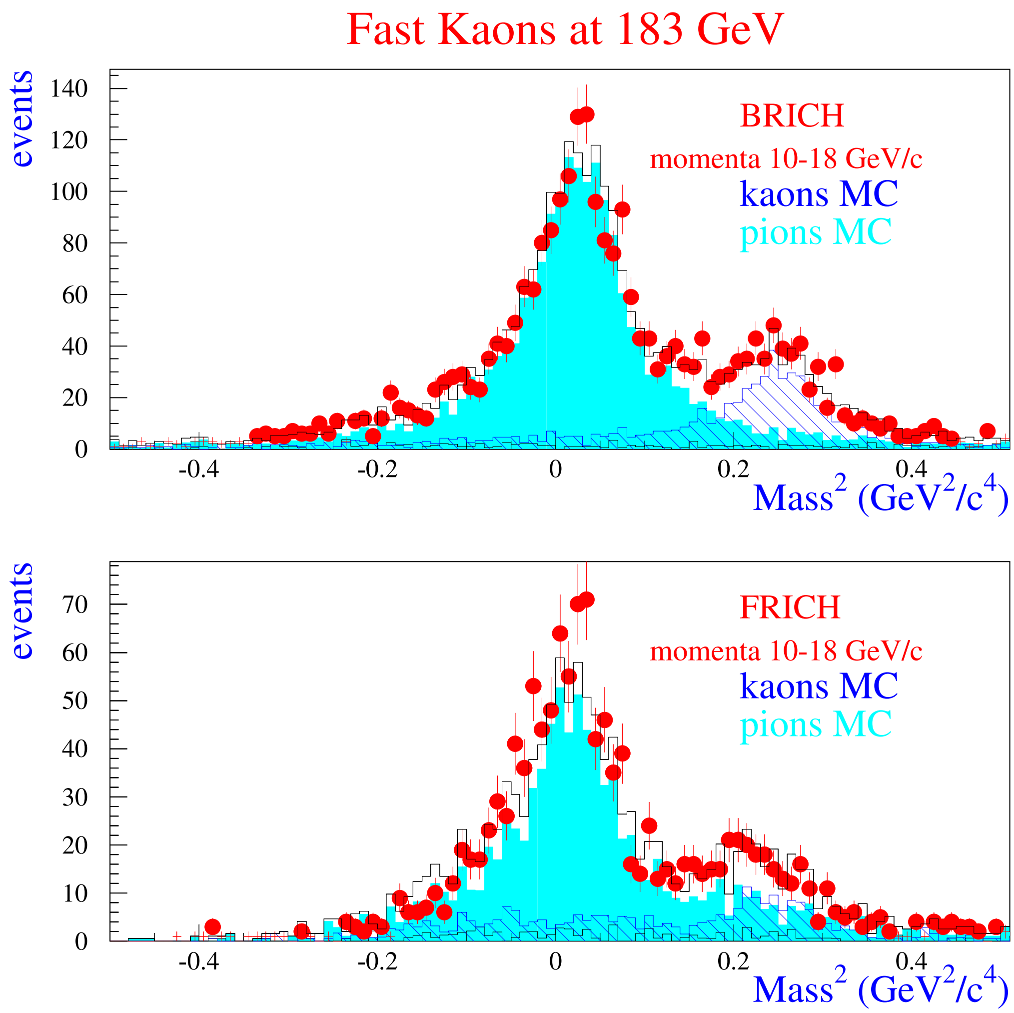

Figure 4.4: Invariant mass of identified pions and kaons from high energy collisions at 183 GeV demonstrates the powerfull separation using the RICH detectors. The mass hypothesis is assigned using the reconstructed and measured Čerenkov angle by RIBMEAN. The squared mass given by the hypothesis is then subtracted from the pion mass squared, 0.0195 GeV^2, corresponding to the peak around zero, while the smaller peak around 0.3 corresponds to kaons.

Chapter 5

Identified Particles from $e^+e^- \rightarrow q\overline{q}$

This chapter describes the results obtained for $\pi^\pm, K^\pm$ and $p(\overline{p})$ with data recorded by DELPHI at LEP 2. It discusses first the event selection for hadronic events above the Z^0 pole. Then the identification of charged particles is described in detail. The momentum spectra obtained are then converted to ξ spectra. The peak of the latter is extracted. The systematic uncertainties involved in this measurement are discussed and average multiplicities for $\pi^\pm, K^\pm$ and $p(\overline{p})$ are calculated. The influence of the detector on the analysis has been checked at all steps with the full DELPHI simulation program, DELSIM [43]. Events were generated with JETSET 7.4 [29], and PYTHIA 5.7 with parameters tuned to fit LEP 1 data as described in ref. [48]. The particles were followed through the detailed geometry of DELPHI, giving simulated digitizations in each sub-detector. These data were then passed through the same analysis and reconstruction chain as the real data.

5.1 Selection of hadronic events at LEP 2 energies

The aim of this chapter is to study the production of $\pi^\pm, K^\pm$ and $p(\overline{p})$ in $e^+e^- \rightarrow Z^{0*}/\gamma^* \rightarrow q\overline{q}(\gamma)$ events. Data recorded by DELPHI from 1995 to 1998 are used. These events are sometimes also referred to as "QCD" or "$q\overline{q}$" events. They are characterised by a usually high charged multiplicity (see Figure 5.1) and a large hadronic energy (see Figure 5.2). As the centre-of-mass energy increases the probability for one or more hard photons to be emitted is quickly rising. This initial state radiation (ISR) leads to an effective reduction of the centre-of-mass energy available for the quark

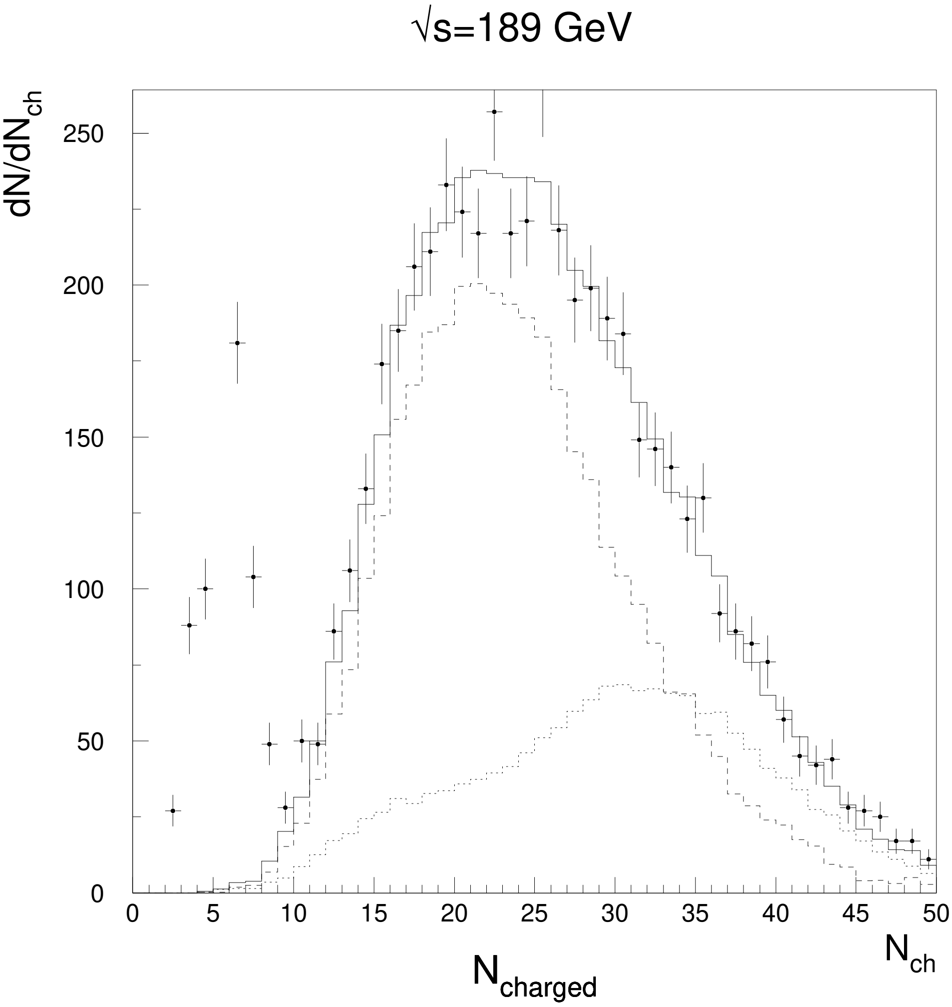

Figure 5.1: Average charged particle multiplicity for hadronic events at 189 GeV. Dots are data, dashed line is the simulation of the signal and the dashed dotted line is the simulation of the background, consisiting of hadrons from WW and Z^0Z^0 pair production. The solid line is the sum of signal- and background simulation.

pair production to the energy at the Z^0 pole. This phenomenon is called radiative return and it is necessary to suppress these events. It is illustrated in Figure 5.3.

Table 5.1 shows the integrated luminosities collected and the expected total hadronic $e^+e^- \rightarrow Z^{0*}, \gamma^* \rightarrow q\overline{q}(\gamma)$ cross sections. Also shown is the fraction of events which actually have more than 85% of their energy in

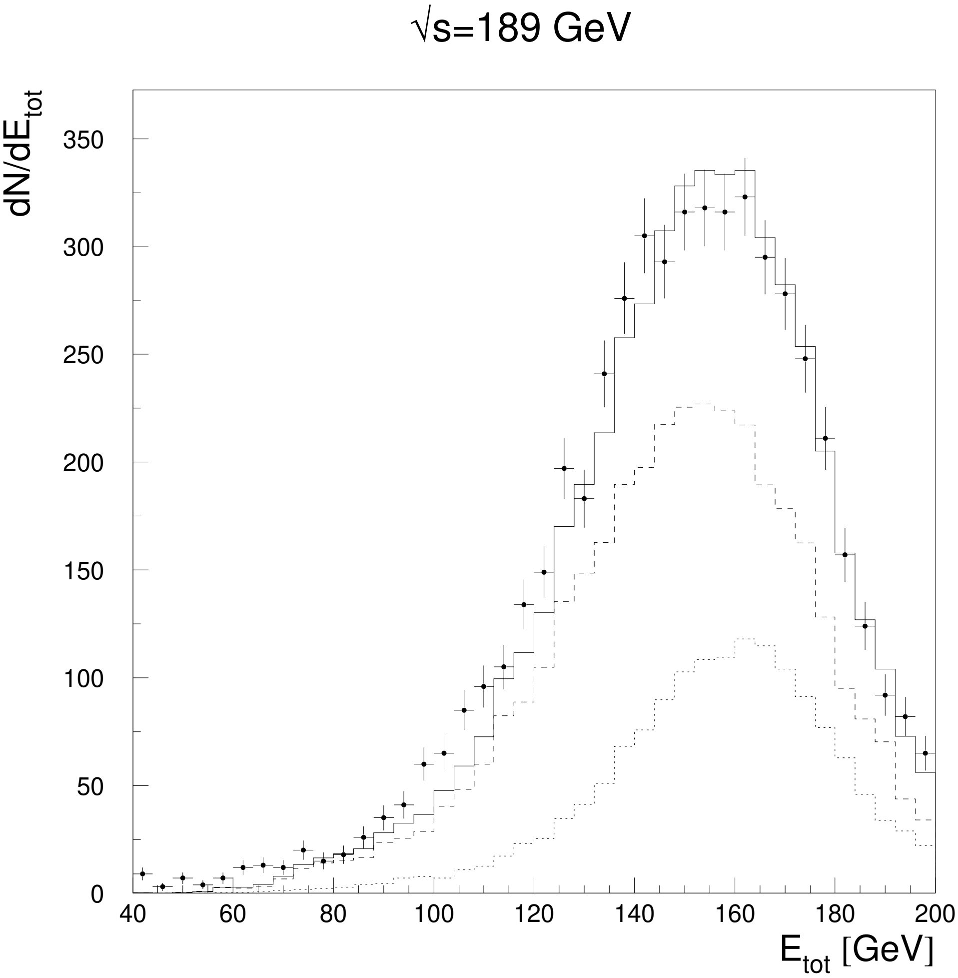

Figure 5.2: Total hadronic energy for hadronic events at 189 GeV. Dots are data, the dashed line is the simulation of the signal, the dashed dottet the simulation of the background (here WW and Z^0Z^0 pair production) and the solid line is the sum of both simulations.

the hard process. One can see that the cross-section is dominated by the radiative return.

In order to compute the effective centre-of-mass energy, the method described in [49] was used. The procedure clusters the particles into two jets using the Durham algorithm [50], excluding candidate ISR photons. Assuming an ISR photon along the beam pipe if no candidate ISR photon has been detected elsewhere, the energy of the ISR photon is computed from the jet directions assuming massless kinematics. The effective centre-of-mass energy

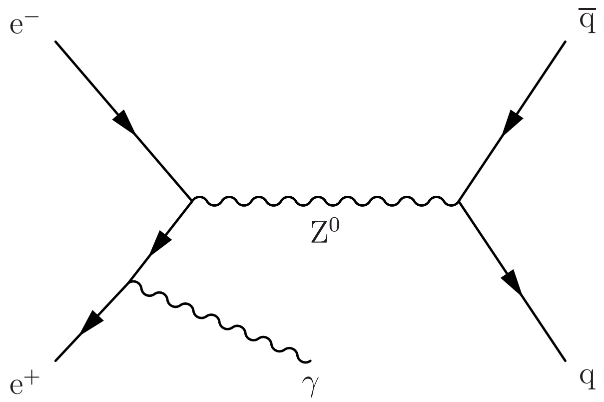

Figure 5.3: Feynman diagramm for the radiative return to the Z^0 pole by emission of a hard inital photon. The Z^0 is on-shell, and the photon vanishes most of the time in the beam pipe.

$\sqrt{s}$ [GeV]	$\sigma_{e^+e^-\to q\overline{q}(\gamma)}$ $[pb]$	$\int \mathcal{L}dt$ $[pb^{-1}]$	$\sigma_{e^+e^-\to q\overline{q}}$ [a]	$\sigma_{W^+W^-}$	year
130	321.2	2.85		0	1995
		2.98			1997
136	267	2.91		0	1995
		3.03			1997
161	147	9.93	35	3	1996
172	121	9.98	29	12	1996
183	100.37	53.46	25	16	1997
189	99.8	155.01	22	17.48 [b]	1998

Table 5.1: Collected luminosities by DELPHI and hadronic cross sections for centre of mass energies between 130 and 189 GeV.

[a] Hadronic cross section $\sigma_{qq}^{(h)}$ for effective centre-of-mass energy $> 0.85E_{cm}$ (from ZFITTER).

[b] Cross section from Excalibur generator. This includes all four fermion final states, in particular it includes also Z^0Z^0 pair production.

of the hadronic system, $\sqrt{s'}$, is calculated as the invariant mass of the system recoiling from the ISR photon.

The method used to obtain the effective centre-of-mass energy overestimates the true energy in the case of double hard radiation in the initial state. For instance, if the two ISR photons are emitted back to back, the remaining two jets may also be back to back, but with energy much smaller than the beam energy. Cutting on the total energy measured in the detector reduces the contamination from such events (see Figure 5.2).

This method is very effective and excellently describes the data as can be seen in Figure 5.4.

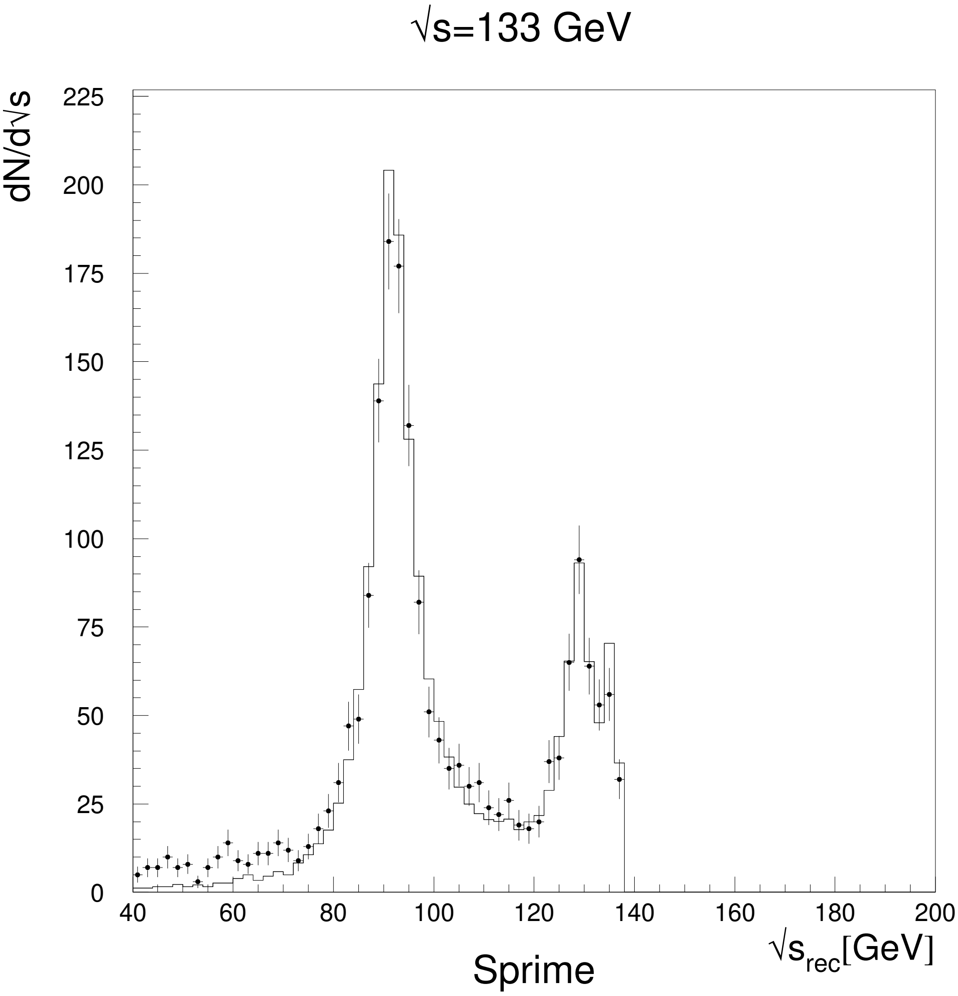

Figure 5.4: Reconstructed effective centre-of-mass energy, $\sqrt{s'}$, for hadronic events from 130 and 136 GeV. Dots are data and the solid line is the simulation of the signal.

Although the event selection varies with the centre-of-mass energy a common pre-selection consists of the following requirements: at least 5 charged particles with momentum p above 400 MeV/c, angle θ with respect to the beam direction between 20° and 160°, a track length of at least 30 cm, a distance of closest approach to the interaction point less than 4 cm in the plane perpendicular to the beam axis and less than 10 cm along the beam axis. The track selection criteria are summarised in table 5.2. Furthermore a total

distance to IP in $R\phi$	≤ 3 cm
distance to IP in Rz	≤ 6 cm
$\delta p/p$	$\leq 100\%$
p	≥ 0.2 GeV/c ≤ 50 GeV/c
tracklength	≥ 30 cm

Table 5.2: Preselection criteria for charged tracks.

energy of the charged particles above 0.15 times the centre-of-mass energy $\sqrt{s}$ is demanded. In the calculation of the energies E, all charged particles have been assumed to have the pion mass. In the following the performance of the event selection is always compared to the performance on simulated data produced with JETSET and PYTHIA.

The cut on the maximal charged multiplicity reduces the contribution from WW and Z^0Z^0 pair production. This can be seen in the right part of Figure 5.1. The cut on the minimal multiplicity almost completely eliminates contribution from $\gamma\gamma$ events and other, rare low multiplicity events, such as t-channel single W production. The influence is negligible, therefore they are not included in the background simulation, they account for the deviation between data and simulation in the left-most part of Figure 5.1. It is also clear from this figure that by demanding at least eight charged tracks, these contributions are eliminated and the overall agreement between data and simulation is good other the full measured range.

The polar angle of the thrust axis is used to suppress events, which are located primarily in the forward region of the detector. Since the reconstruction efficiency is considerably worse for very small polar angles, a cut on the polar angle of the thrust reduces the systematic uncertainty on the overall reconstruction. For $q\overline{q}$ events, which are two jet-like in their great majority, the thrust axis is to a good approximation to the event axis. This cut has been invariably $30^\circ \leq \theta_{\text{thrust}} \leq 150^\circ$ at all energies.

As has been mentioned above, a cut on the total hadronic energy, whose distribution is shown in Figure 5.2, reduces the contribution from double ISR events. It also further reduces the number of events which have large missing or leptonic energy, like leptonic W and Z^0 decays. This cut is usually applied in the form of demanding a hadronic energy greater than a certain fraction of the nominal centre-of-mass energy. In this analysis this cut is usually set to $E_{\text{tot}} \geq 50\% E_{\text{cms}}$.

In the following the specific selections at the various centre-of-mass energies are described. The event selection is then summarised in table 5.3.

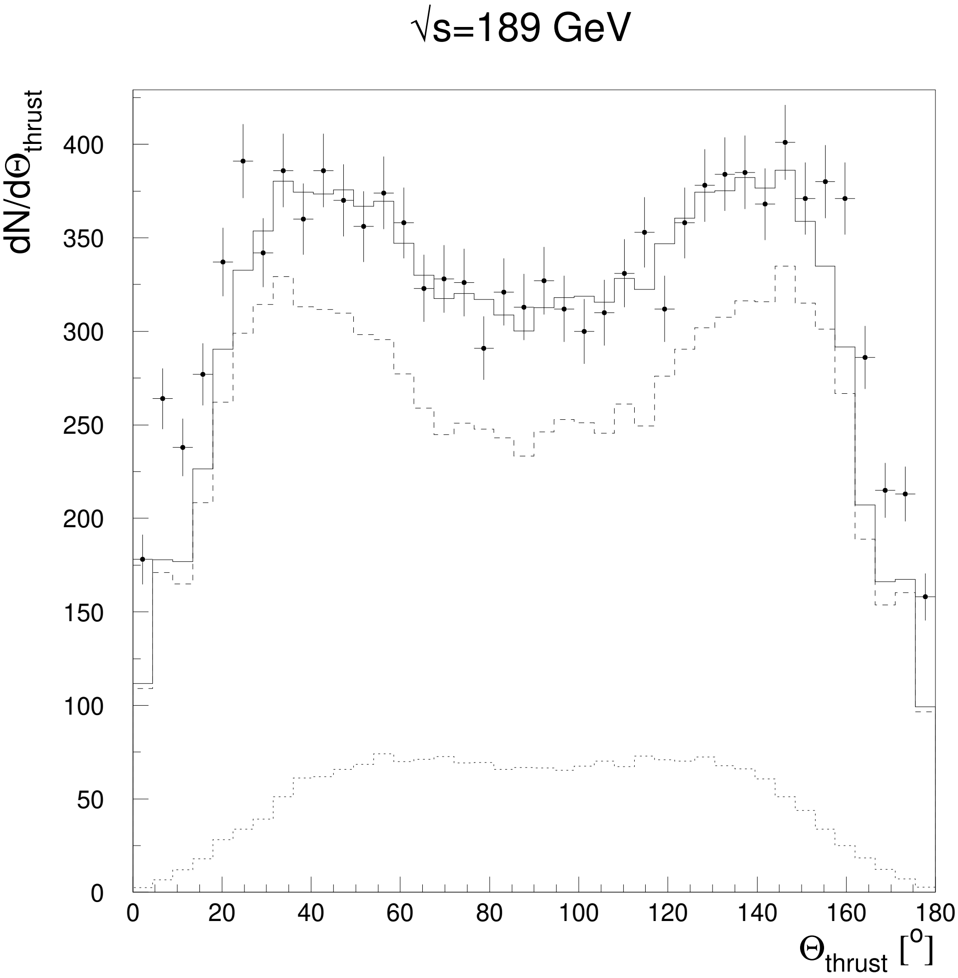

Figure 5.5: Polar angle of the thrust axis in hadronic events at 189 GeV. Dots are data, dashed line is the simulation of the signal, dashed dotted line is the simulation of the background and the solid line is the sum of both. For two-jet events the majority of particles lies around this axis.

5.1.1 Event selection at 130 and 136 GeV

After the hadronic preselection described above, events with a reconstructed effective centre of mass energy, $\sqrt{s'}$, of at least 85% of the nominal centre-of-mass energy have been used for further analysis.

Data recorded at these two energies have been combined and are referred to as the 133 GeV sample. The total of $\sim$ 12 pb^{-1} recorded by DELPHI yields 1387 events while 1406 are expected from simulation.

5.1.2 Event selection at 161 GeV

Selected events must have a minimum of 8 and a maximum of 40 charged tracks, a reconstructed centre of mass energy of at least 85% of $\sqrt{s}$ and a visible energy of at least 50% of $\sqrt{s}$. A cut is imposed on the polar angle θ of the thrust axis to select events well within the acceptance of the detector. Since this energy is above the threshold for W^+W^- production these events have also to be removed. It has been found that a selection based on the *minimal (or narrow) hemisphere broadening*, $B_{\min}$, is effective and minimises the bias introduced on the remaining event sample.

At threshold one expects ~ 30 W^+W^- events. Selecting events with $B_{\min} \leq 0.12$, reduces the background by 50%.

Using this selection 342 events are expected from simulation, while 357 were selected from the data, with an estimated remaining WW background of 15 events.

5.1.3 Event selection at 172 GeV

In addition to the criteria described so far an event has been selected if it had at most 38 charged tracks and a $B_{\min} \leq 0.1$. This leads to 267 selected events, with 264 expected from simulation out of which 36 are WW background.

5.1.4 Event selection at 183 and 189 GeV

Events at 183 (189) GeV with $\sqrt{s'}/\sqrt{s}$ above 0.9 were used. The WW background was suppressed by demanding $B_{\min} \leq 0.1(0.08)$, more than 9(8) charged particles with $p \geq 200$ MeV/c. An additional background process, Z^0Z^0pair production has to be taken into account. Since its cross-section is small further attempt has been made to reduce it and its contribution has been estimated using simulation*. A total of 3617(1122) were selected with an expected background from Z^0Z^0 and WW of 789(146) events. The distribution of the selecting variable $B_{\min}$ at 189 GeV is shown in Figure 5.6.

5.1.5 Selection of charged tracks for identification

Charged tracks must be carefully selected to ensure a reliable identification. A track was accepted if it had momentum $p > 200$ MeV/c, a relative error on the reconstructed momentum $\delta p/p$ of less than one, a reconstructed track

*However the cut on the total charged multiplicity reduces the contribution from these events.

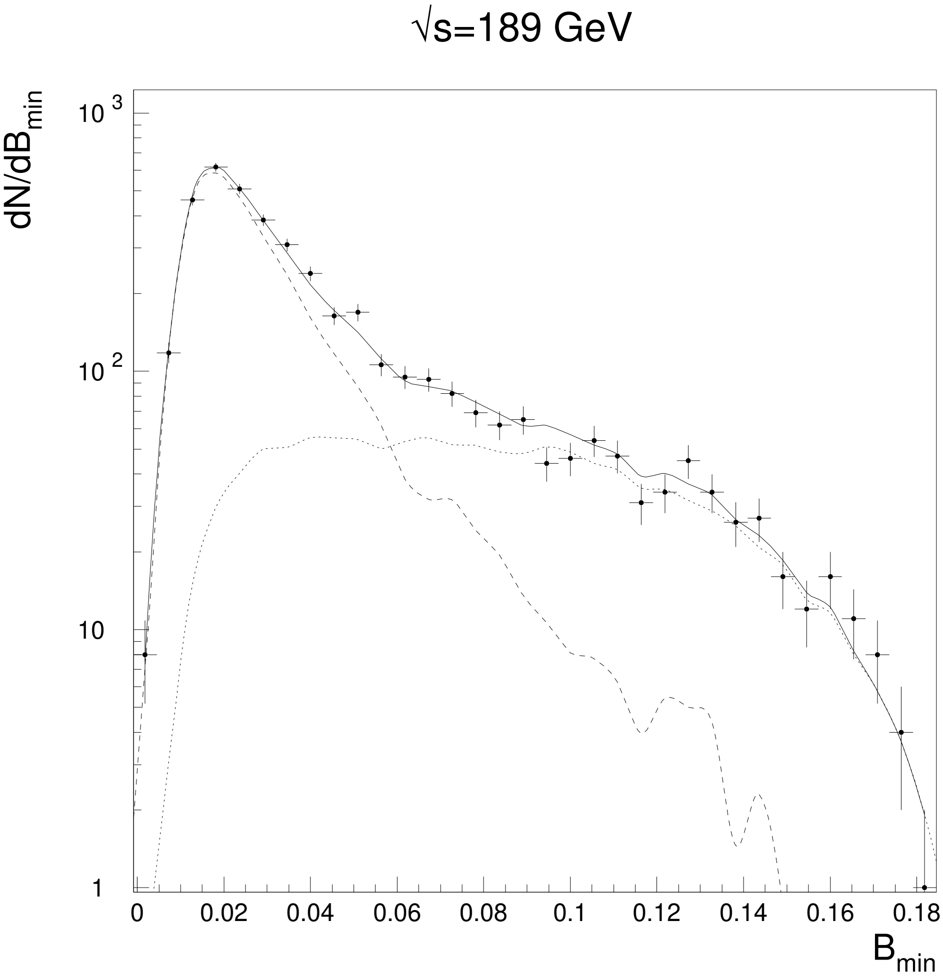

Figure 5.6: Separating variable $B_{\rm min}$ at 189 GeV. The dashed line corresponds to expected signal simulation using JETSET, the dotted line to expected WW background from PYTHIA, the solid line to the sum of both. Points are DELPHI data. It can be seen that WW events are typically broader in the sense of this variable, which helps in separating them from the $q\overline{q}$ signal.

length of at least 30 cm[†] and impact parameters in $R\phi$ and z of maximally 1 and 2 cm respectively. Two different momentum regions are considered, above and below 700 MeV, which correspond to the separation of samples

[†]This is equivalent of demanding the TPC and at least one other tracking detector to have participated in the reconstruction.

161 GeV	172 GeV	183 GeV	189
$8 \leq N_{charged} \leq 40$	$8 \leq N_{charged} \leq 38$	$8 \leq N_{charged} \leq 38$	$8 \leq N_{charged} \leq 38$
$\sqrt{s'} \geq 85\% E_{cms}$			$\sqrt{s'} \geq 90\% E_{cms}$
$30 \leq \theta_{thrust} \leq 150$			
$E_{\rm vis} \geq 50\% \sqrt{s}$			
$B_{min} \leq 0.12$	$B_{min} \leq 0.1$	$B_{min} \leq 0.08$	$B_{\rm min} \leq 0.1$

Table 5.3: Selection criteria for hadronic events above the W threshold.

identified solely by the ionization loss in the Time Projection Chamber (TPC) and by RICHes and TPC together respectively. Below 700 MeV tighter cuts are applied, namely to eliminate secondary protons. There had to be at least 30 wire hits in the TPC associated with the track and the measured track length had be to larger than 100 cm. In addition at least two associated VD layer hits in $r\phi$ are required and an impact parameter in the $r\phi$ plane of less then 0.1 cm. If there are less then two associated layers in z the corresponding impact parameter has to be less than 1 cm, else less then 0.1 cm. Tracks above 0.7 GeV/c are required to have a measured track length bigger than 30 cm and good RICH quality, e.g. presence of primary ionization in the veto regions[‡]. Only tracks which are contained in the barrel region of DELPHI ($| \cos(\theta) | \leq 0.7$) are accepted.

5.2 Analysis

To maximise the efficiency of identification of charged particles over the full momentum region information from the ionization loss in the TPC ("dE/dX") and information from the DELPHI RICH-detectors has been combined in the manner explained before. Throughout this analysis leptons have not been discerned from pions. There contribution to the pion sample has been subtracted using simulation. Charged tracks are assigned tags as explained in chapter, section .

A matrix inversion formalism [51] is used to calculate the true particle rates in the detector from the tagged rates. The 3×3 efficiency matrix is defined by

$$\mathcal{E}_{xx}^{yy} = \frac{Number\ of\ xx\ tagged\ as\ yy}{Number\ of\ xx} \tag{5.1}$$

[‡]Charged tracks traversing the TPCs of the RICHes cause a big ionization cloud, which is a nuisance for particle identification. On the other hand this is a simple and effective criterion to check whether a specific chamber of the RICH was functional. This is important to avoid a misidentification due to a fake veto decision.

It establishes the connection between the true particles in the RICH/TPC and the tagged ones:

$$\begin{pmatrix} N_\pi^{meas} \\ N_K^{meas} \\ N_p^{meas} \end{pmatrix} = \mathcal{E} \begin{pmatrix} N_\pi^{true} \\ N_K^{true} \\ N_p^{true} \end{pmatrix} \tag{5.2}$$

The inverse of the efficiency matrix works on the three classes of tagged particles in two ways. First a particle can have multiple tags, that means the information from the tagging is ambiguous; for example it is compatible with a kaon as well as with being a proton. This is not unlikely because in this analysis one is forced by the low statistics of the data samples to apply rather loose selection criteria. Secondly a particle can escape identification. Both effects can be corrected by this method. The particle identification efficiency and hence also the matrix are strongly dependent on the momentum of the particle, because different physical effects are used for identification in different regions. Figure 5.7 shows the efficiency matrix for data at 183 GeV. As one can see it is mostly populated in the diagonal, as is expected from a method with reasonable efficiency and purity. In addition the momentum dependence of the identification efficiency and the probability for misidentification are visible.

Before it is can be used on the data, the matrix has to be calibrated to the ture detector response as described in the appendix, section A.1.

5.2.1 Fractions and normalised production rates of identified particles

After the calibration described in the last section the efficiency matrix is inverted and applied to the tag rates of charged particles at high energies from which the remaining background has been subtracted beforehand.

Due to the correlations induced by the classification of particles into three classes a careful statistical treatment is necessary to derive proper estimates of the statistical uncertainties of the unfolded fractions.

The full covariance matrix is calculated for the tag rates using multinomial statistics. It is then propagated to the true rates using also the same unfolding matrix. The off diagonal elements after this procedure have been found to be very small. The diagonal elements of the covariance matrix are taken as the new statistical errors for the 3 rates. The tagging rates from simulation are propagated in the same way. This allows one to compare them with the original true rates in the simulation, this is a trivial but important cross-check.

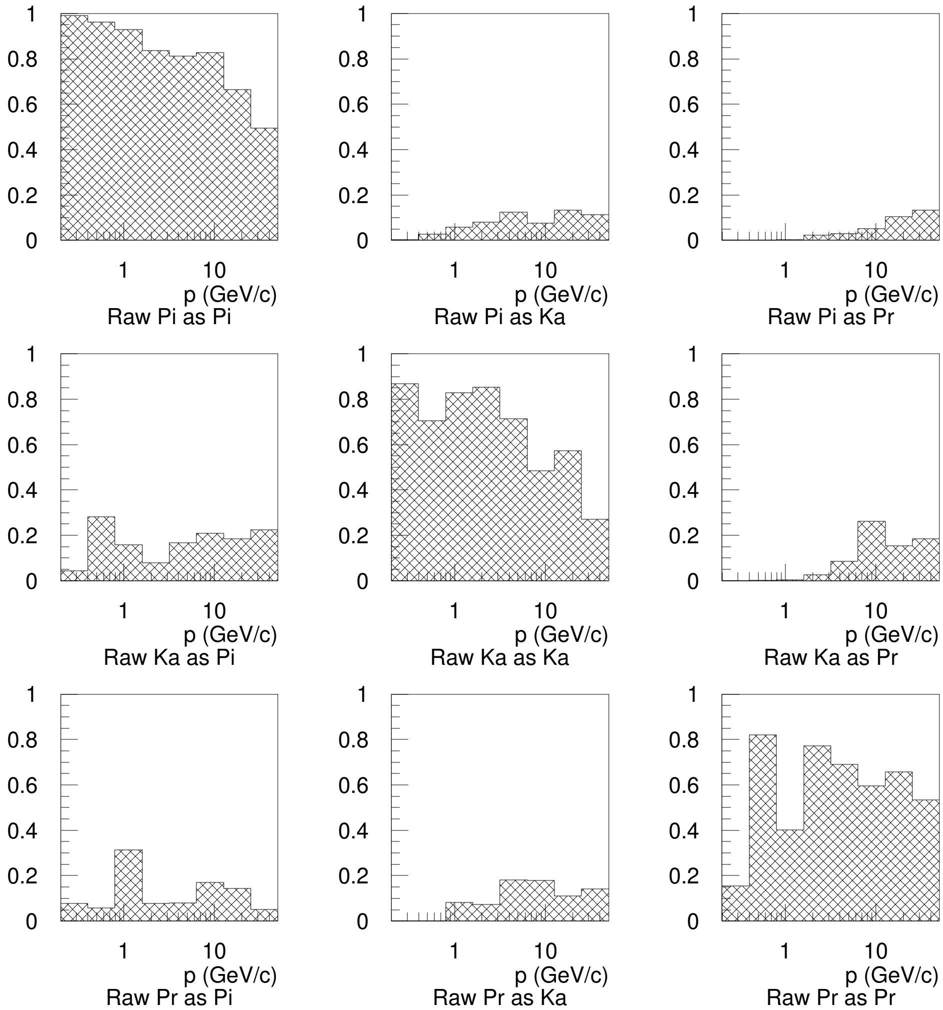

Figure 5.7: Efficiency matrix for data at 183 GeV. The picture indicates the momentum dependence of efficiency and purity of the tagged samples.

First results which can be derived at these stage, are the normalised production rates which correspond to differential production cross sections. This is shown in Figs. 5.8, 5.9, 5.10, 5.11 and 5.12 for all energies and compared to the JETSET generator.

5.2.2 ξ_p distributions and average multiplicities

After background subtraction the tagged particle fractions have been unfolded using the calibrated matrix. The full covariance matrix has been calculated for the tag rates using multinomial statistics. It has then been propagated to the true rates of identified particles using the unfolding matrix. As a first result normalised production rates can be derived, which correspond to differential production cross sections. An example is shown in Figure A.1.

For the purpose of better comparison with the analytical calculations the momentum spectra are then converted to ξ_p spectra using the formula $\xi_p = \ln \sqrt{s/2}/2p$.

The ξ_p distribution is corrected bin by bin (for detector acceptance and selection efficiency) using the full detector simulation (DELSIM and JETSET). The corrected ξ_p distributions for $\pi^{\pm}, \mathrm{K}^{\pm}$ and $\mathrm{p}(\overline{\mathrm{p}})$ are shown in figs. 5.13, 5.14, 5.15 and 5.16. respectively. In the figures the predictions from the DELPHI tuned versions of the JETSET 7.4, HERWIG 5.8 and ARIADNE 4.8 as well as a fit to expression 1.21 are also shown. Within the statistics of the data samples analysed, the shape of the ξ_p distributions is well described by the generators.

The multiplicity of the identified final states per hadronic event was obtained by integration of the corresponding ξ_p distributions. The results are shown in table 5.4. The numbers given for charged identified hadrons include decay products from particles with a lifetime $\tau < 10^{-9}$ s. These numbers are compared with the predictions from JETSET 7.4, HERWIG 5.8 and ARIADNE 4.8.

The following sources of systematic uncertainties are taken into account.

- Uncertainties due to particle identification.

  They are mainly due to the uncertainties in the modelling of the detector response. In addition there are time dependent effects such as variations of the drift velocity in the RICHes.

  The unfolding matrix has been adjusted using the Z^0-calibration data recorded in the beginning of data taking in 1996 and 1997, as well as from the peak period in 1995. This is described as explained in section A.1. For 1997 and 1998 data also radiative return Z^0-events have been used. These are better suited as they have been recorded under the same conditions as the signal events.

  Spectra have been obtained using the original and the adjusted matrices. The difference between the results obtained has been taken as the corresponding systematic uncertainty.

- Size of the subtracted WW and Z^0Z^0 background (where applicable).

  Variation of the selection criteria results in a 10% uncertainty on the fraction of the W contamination in the $q\overline{q}$ sample. This corresponds to a 5% uncertainty in the W cross section and the size of the W background has been varied accordingly. The maximal variation observed in the distributions has been taken as the corresponding systematic uncertainty.

- Particles with momenta below 0.2 GeV/c or above 50 GeV/c have not been identified. Their contribution is taken from the simulation.

  For the invisible momentum region the predictions from each of the 3 generators for each particle species are compared. The maximal difference is added in quadrature to the uncertainty of each particle type.

- For the pions this analysis relies on a subtraction of the lepton contamination using simulation.

  An extra uncertainty of 10% of the JETSET prediction for the total number of leptons is added.

5.2.3 ξ^* and its evolution

An interesting aspect of the ξ_p-distribution is the evolution of its peak position ξ^* with increasing centre-of-mass energy. It is determined by fitting a parametrisation of the distribution to the peak region.

A possible such parametrisation is the distorted Gaussian in eq. (1.21).

Another parametrisation is a standard Gaussian distribution. While being a more crude approximation, it facilitates the analysis in the case of limited statistics. This simpler parametrisation was used as well The fitted mean has been identified with the peak position with the statistical uncertainty taken from the fit.

Since eq. (1.21) is expected to describe well only the peak region, the fit range has to be carefully chosen around the peak. Unfortunately the fit sometimes fails due to limited statistics. Table 5.5 shows the results with fit range and statistical as well as systematic uncertainties.

The systematic uncertainty has the following contributions which are added in quadrature to the statistical uncertainty of either fit. The procedure is the same for the Gaussian and distorted Gaussian fit.

- Uncertain size of the background subtracted (above the W threshold).

$\sqrt{s}$ [GeV]	Particle	$< n >$			
		JETSET 7.4	HERWIG 5.8	ARIADNE 4.8	Data
133	$\pi^{\pm}$	19.90	19.99	19.64	$19.84 \pm 0.29 \pm 0.08$
	$\mathrm{K}^{\pm}$	2.37	2.31	2.30	$2.60 \pm 0.26 \pm 0.13$
	$\mathrm{p}(\overline{\mathrm{p}})$	1.11	1.09	1.29	$1.56 \pm 0.25 \pm 0.09$
161	$\pi^{\pm}$	21.24	12.76	21.12	$20.75 \pm 0.58 \pm 0.24$
	$\mathrm{K}^{\pm}$	2.63	2.44	2.44	$2.87 \pm 0.55 \pm 0.16$
	$\mathrm{p}(\overline{\mathrm{p}})$	1.26	0.96	1.40	$1.21 \pm 0.48 \pm 0.01$
172	$\pi^{\pm}$	21.77	22.31	21.68	$21.79 \pm 0.68 \pm 0.16$
	$\mathrm{K}^{\pm}$	2.68	2.48	2.50	$2.09 \pm 0.74 \pm 0.29$
	$\mathrm{p}(\overline{\mathrm{p}})$	1.30	0.99	1.45	$1.78 \pm 0.73 \pm 0.25$
183	$\pi^{\pm}$	22.28	22.82	21.18	$21.79 \pm 0.36 \pm 0.13$
	$\mathrm{K}^{\pm}$	2.74	2.53	2.55	$2.83 \pm 0.37 \pm 0.03$
	$\mathrm{p}(\overline{\mathrm{p}})$	1.33	1.00	1.48	$1.32 \pm 0.34 \pm 0.01$
189	$\pi^{\pm}$	22.56	23.10		$22.19 \pm 0.24 \pm 0.12$
	$\mathrm{K}^{\pm}$	2.77	2.55		$3.15 \pm 0.21 \pm 0.04$
	$\mathrm{p}(\overline{\mathrm{p}})$	1.35	1.02		$1.19 \pm 0.17 \pm 0.01$

Table 5.4: Average multiplicities of charged particles and $\pi^{\pm}, \mathrm{K}^{\pm}$ and $\mathrm{p}(\overline{\mathrm{p}})$ at 133, 161, 172, 183 and 189 GeV. The first uncertainty is statistical the second systematic.

By the same argument as for the estimation of the uncertainty for the multiplicities the maximal difference obtained by a variation of the WW background cross-section is added to the systematic uncertainty.

- Uncertainty due to the particle identification.

  The fit is repeated using the calibrated matrices as described for the measurement of average multiplicities the maximal difference obtains thus is added in quadrature

- Stability of the fit within limited statistics and dependence on fit range.

  Finally there is an uncertainty which arises from the combination of the limited statistics, the resulting need to choose a coarse binning, and the choice of the fit range. To estimate this effect systematic shifts have been imposed on the data by variation within the statistical uncertainty. One standard deviation has been added to the values left of the peak and one standard deviation has been subtracted form the values to its right and vice versa. The maximum variation is taken as the contribution to the systematic uncertainty.

  The maximal difference obtained in this way has again been added in quadrature

Figure 7.1 shows the fitted ξ^* values as a function of the centre-of-mass energy. As discussed in chapter 1, eq. 1.25, this has been predicted [17, 21] to be

$$\xi^* = Y(\frac{1}{2} + a\sqrt{\frac{\alpha_s(Y)}{32N_c\pi}} - a^2\frac{\alpha_s(Y)}{32N_c\pi} + F_h(\lambda)), \tag{5.3}$$

where

$$Y = \ln E_{beam}/\Lambda, E_{beam} = E_{cms}/2, \alpha_s(Y) = \frac{1}{b_0 Y}, \tag{5.4}$$

$$a = \frac{11}{3}N_c + \frac{2n_f}{3N_c^2}, b_0 = \frac{11N_c - 2n_f}{12\pi}. \tag{5.5}$$

Setting N_c, n_f to 3 one left with Λ_{eff} and F_h as only free parameters. Due to uncertainties from higher order corrections Λ_{eff} cannot be identified with $\Lambda_{\overline{MS}}$. $F_h = F_h(\lambda)$, $\lambda = \log\frac{Q_0}{\Lambda_{\text{eff}}}$, has been calculated [17]:

$$F_h(\lambda) = -1.46\lambda + 0.207\lambda^2 \pm 0.06. \tag{5.6}$$

$\sqrt{s}$		fit range		JETSET		HERWIG		ARIADNE		Data	
		Gauss.	dist. G.	Gauss.	dist. G.	Gauss.	dist. G.	Gauss.	dist. G.	Gauss.	dist. G.
133	$\pi^{\pm}$	[3.3 : 4.9]	[2.5 : 5.5]	3.9	4.11	3.9	4.12	4.00	4.15	4.04 ± 0.03	4.32 ± 0.37
	$K^{\pm}$	[2.1 : 3.3]	[2.2 : 3.2]	2.85	2.99	2.86	2.99	2.85	2.99	2.90 ± 0.3	-
	K^0	-	[0.6 : 5.4]		2.87		3.15				2.86 ± 0.43
	$p(\overline{p})$	[2.1 : 3.3]	[2.5 : 5.5]	3.04	3.09	3.04	3.10	3.04	3.04	2.74 ± 0.33	-
	Λ	-	[0.6 : 4.8]		2.79		2.99				2.81 ± 0.66
161	$\pi^{\pm}$	[3.5 : 5.1]	[2.6 : 4.5]	4.09	4.17	4.03	4.08	4.12	4.18	4.11 ± 0.05	4.14 ± 0.48
	$K^{\pm}$	[2.1 : 3.7]	[2.1 : 3.1]	2.99	2.98	3.00	3.00	3.01	2.98	3.16 ± 0.5	3.21 ± 2.25
	K^0										
	$p(\overline{p})$	[2.1 : 3.7]	[2.2 : 3.1]	3.01	3.14	3.2	-	3.14	3.06	3.08 ± 0.84	-
172	$\pi^{\pm}$	[3.5 : 5.1]	[2.6 : 4.5]	4.13	4.2	4.06	4.12	4.16	4.21	4.11 ± 0.03	4.45 ± 0.4
	$K^{\pm}$	[2.1 : 3.7]	[2.1 : 3.1]	3.04	3.02	3.03	3.01	3.05	3.01	2.98 ± 0.84	-
	K^0										
	$p(\overline{p})$	[2.1 : 3.7]	[2.2 : 3.1]	3.16	3.14	3.23	3.41	3.18	3.12	3.55 ± 1.1	-
183	$\pi^{\pm}$	[2.6 : 4.5]	[3.5 : 5.1]	4.16	4.43	4.10	4.3	4.19	4.44	4.23 ± 0.03	4.63 ± 0.2
	$K^{\pm}$	[2.1 : 3.1]	[2.1 : 3.7]	3.08	3.18	3.06	3.15	3.1	3.23	3.08 ± 0.29	-
	$p(\overline{p})$	[2.3 : 3.1]	[2.1 : 3.7]	3.21	3.32	3.31	-	3.21	3.39	3.29 ± 0.18	3.29 ± 0.52
189	$\pi^{\pm}$	[2.6 : 4.5]		4.22						4.18 ± 0.1	
	$K^{\pm}$	[2.4 : 4.8]	[1.2 : 6.0]	3.13	3.02					3.06 ± 0.14	3.31 ± 0.80
	$p(\overline{p})$	[2.3 : 3.1]		3.11						3.18 ± 0.12	

Table 5.5: Values of ξ^* for $\pi^{\pm}$, $K^{\pm}$ and $p(\overline{p})$ at 133, 161, 172, 183 and 189 GeV. The uncertainties include all contributions.

The results are somewhat limited by the small size of the data samples, nevertheless within their accuracy they are in good agreement with the expectations.

The comparison with eq. (1.25) and previous measurements taken from [21] is shown in Figure 7.1. The fit of the data points to expression 1.21 was used to extract the peak position of the ξ_p distribution, ξ^*.

In Figure 7.1 the evolution of ξ^* with the centre-of-mass energy is presented. The data up to centre-of-mass energies of 91 GeV were taken from previous measurements [21]. The fit to expression 1.25 is superimposed to the data points (solid line). Figure 7.1 shows that (within the statistics of the data samples analysed) the fitted functions follow the data points rather well. This suggests that MLLA+LPHD gives a good description of the observed particle spectra. From table 5.5 it is shown that there is fair agreement between the data and the predictions from the generator (JETSET 7.4).

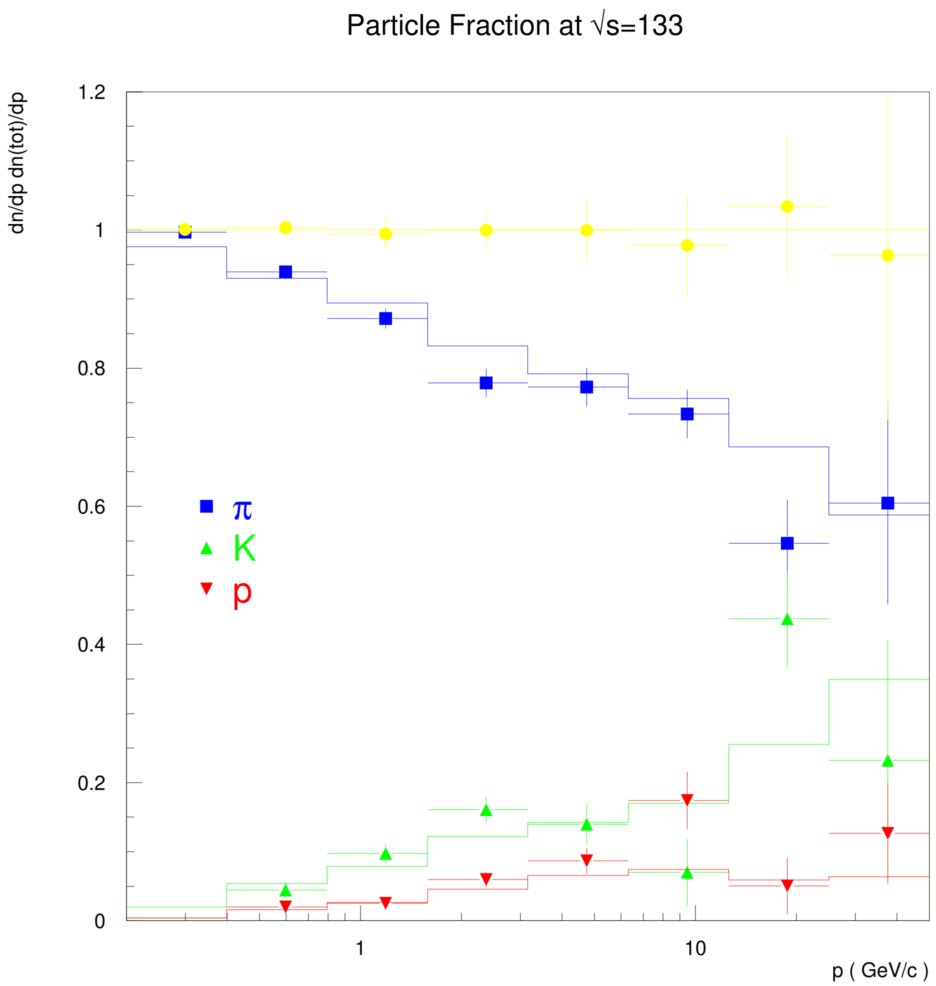

Figure 5.8: Fractions of identified hadrons at 133 GeV. Solid line corresponds to Pythia 5.7 with Delphi tuned Jetset 7.4, including full detector simulation.

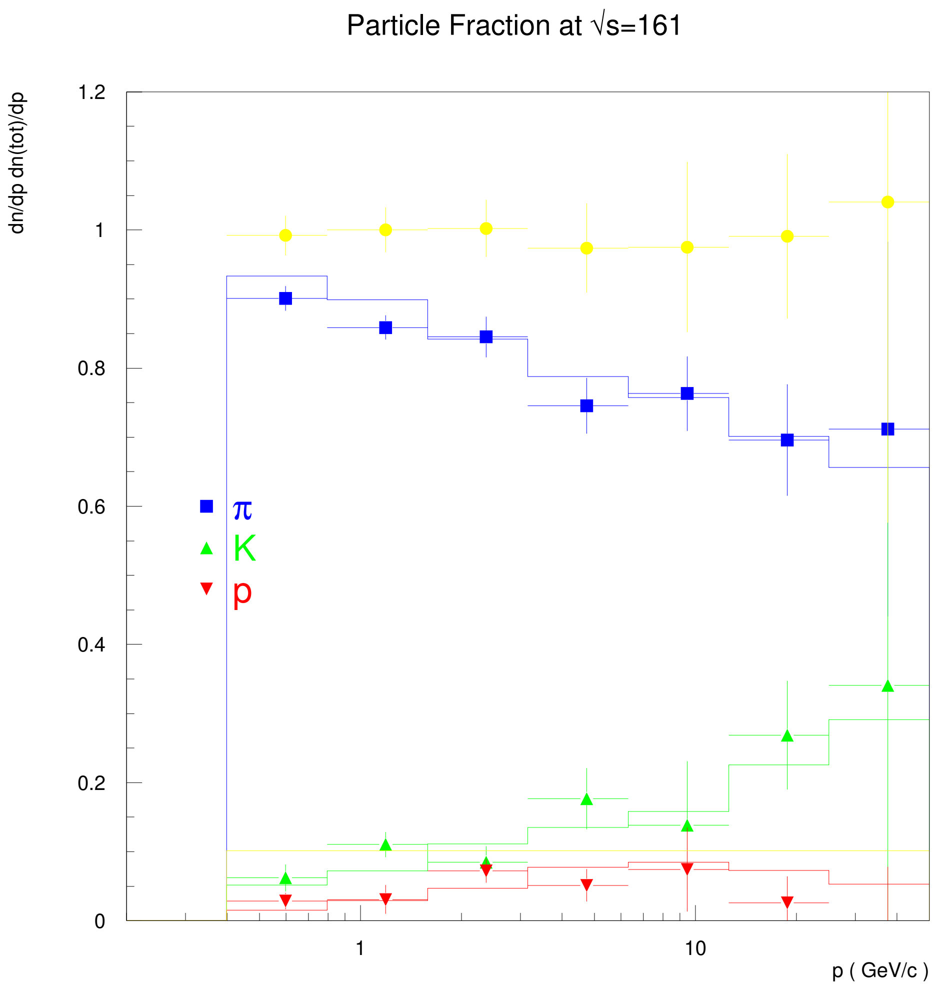

Figure 5.9: Fractions of identified hadrons at 133 GeV. Solid line corresponds to Pythia 5.7 with DELPHI tuned Jetset 7.4, including full detector simulation.

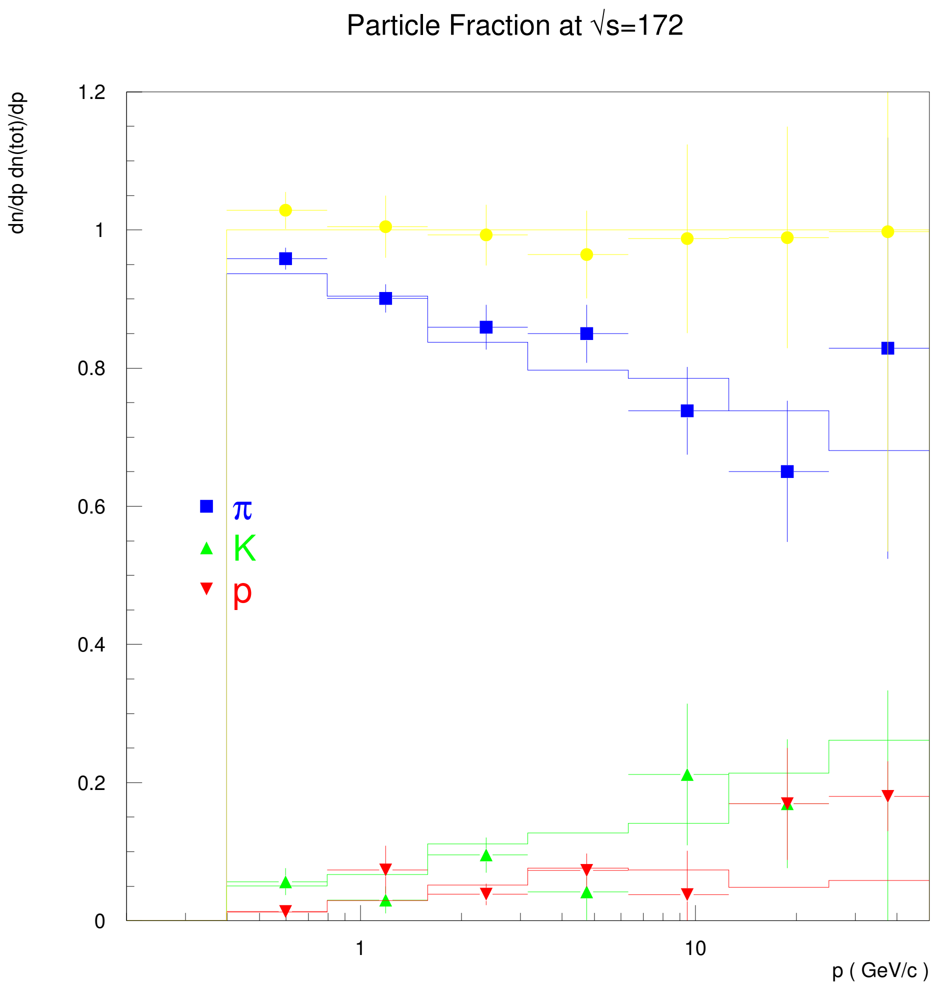

Figure 5.10: Fractions of identified hadrons at 133 GeV. Solid line corresponds to Pythia 5.7 with DELPHI tuned Jetset 7.4, including full detector simulation.

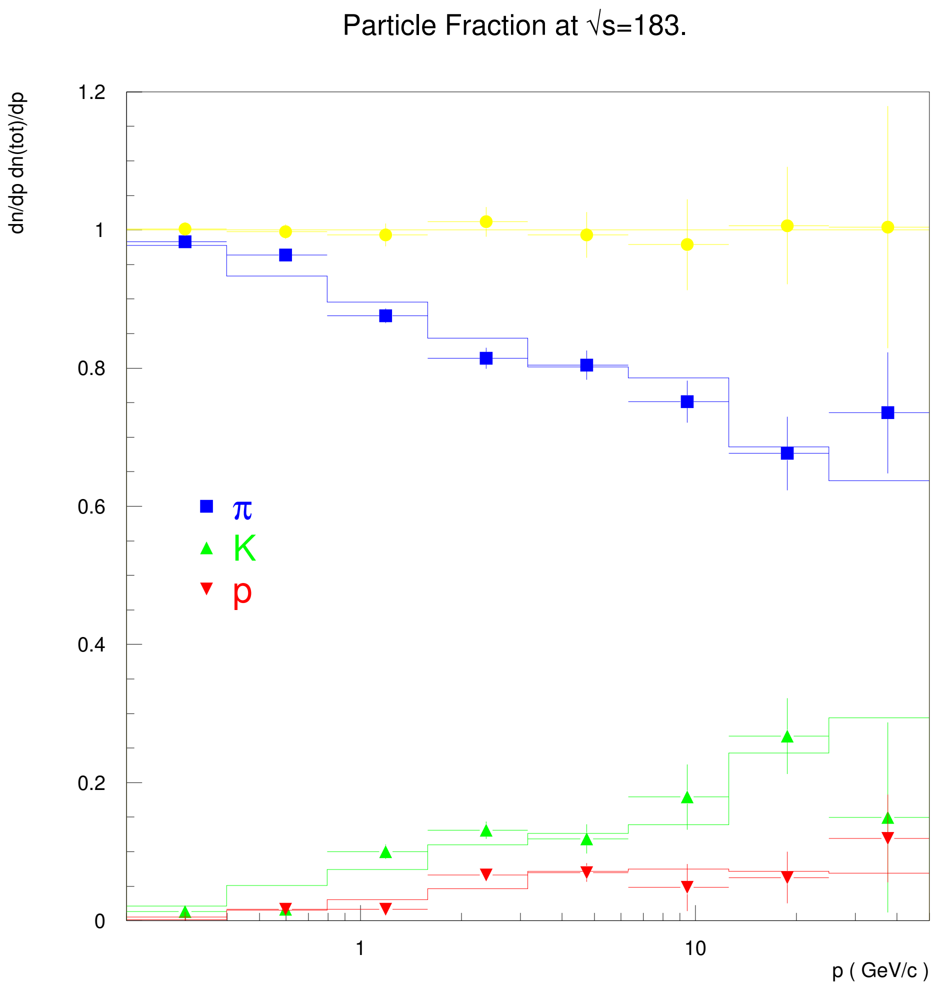

Figure 5.11: Fractions of identified hadrons at 183 GeV. Solid line corresponds to Pythia 5.7 with DELPHI tuned Jetset 7.4, including full detector simulation.

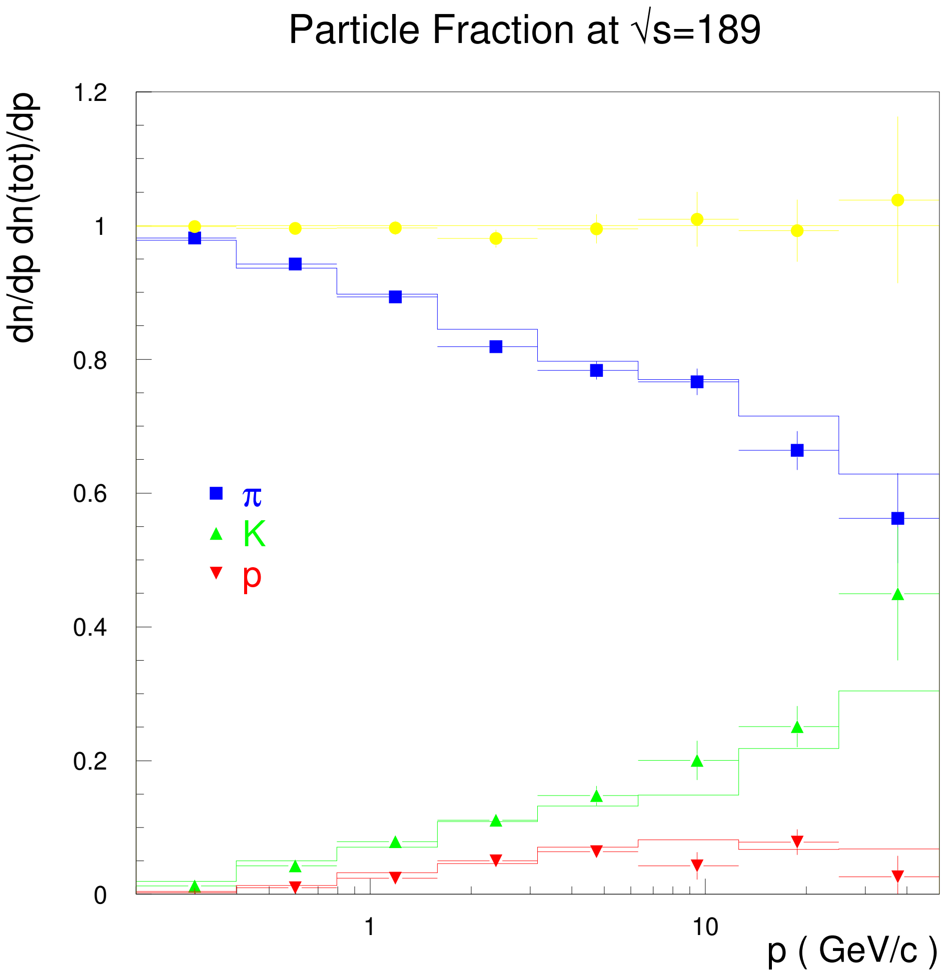

Figure 5.12: Fractions of identified hadrons at 189 GeV. Solid line corresponds to Pythia 5.7 with DELPHI tuned JETSET 7.4, including full detector simulation.

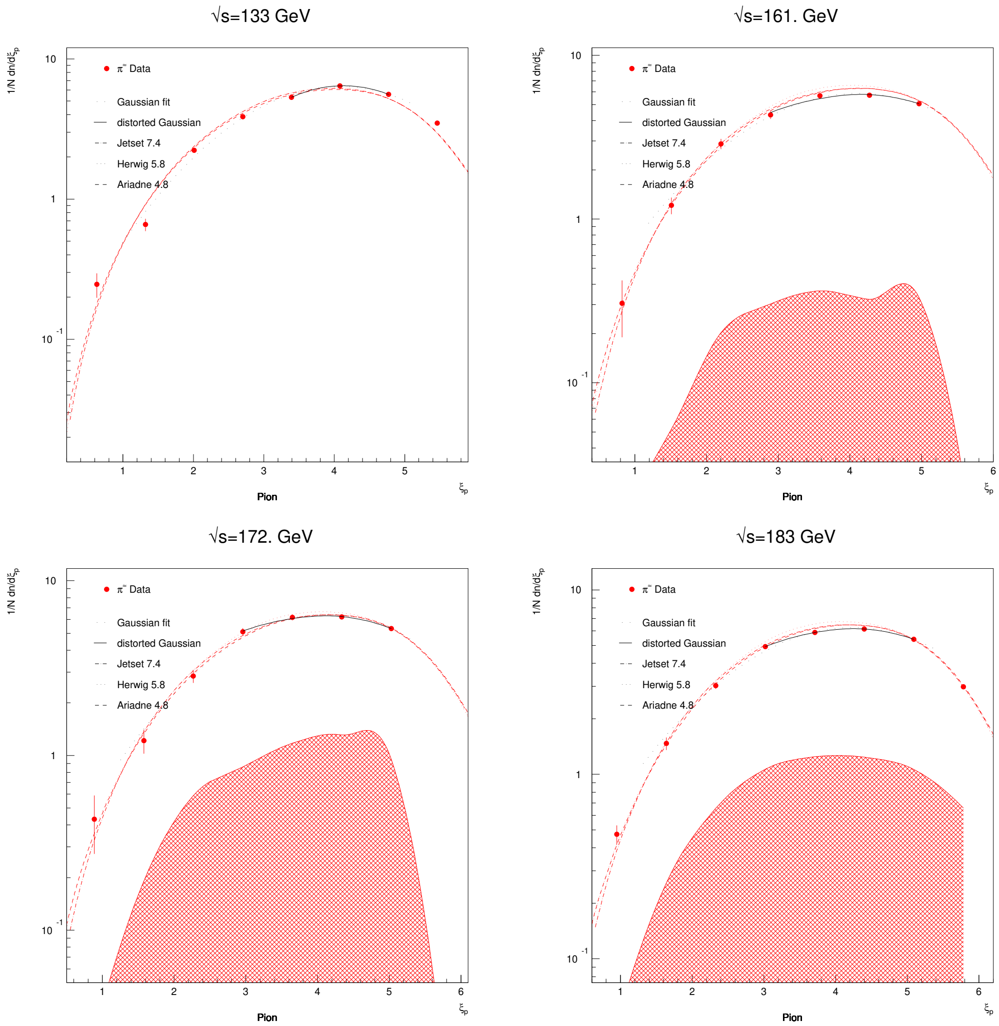

Figure 5.13: ξ_p distributions (fully corrected) for π at 133 GeV, 161 GeV, 172 GeV and 183 GeV: data (points), simulation using JETSET (dashed dotted line), HERWIG (dotted line), ARIADNE (dashed line). The full (dotted) curve shows a distorted Gaussian (Gaussian) fit to the data. The shaded area indicates the acceptance corrected background subtracted from the data.

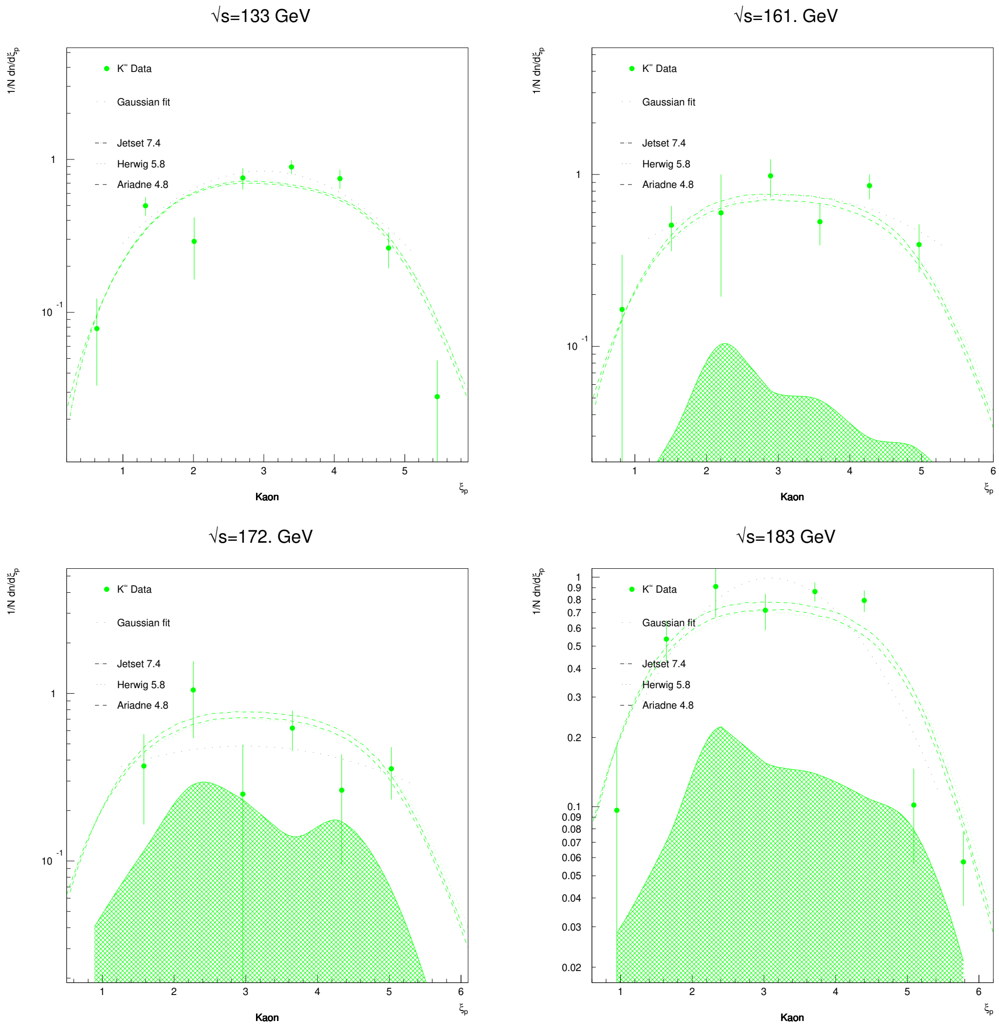

Figure 5.14: ξ_p distributions (fully corrected) for charged Kaons at 133 GeV, 161 GeV, 172 GeV and 183 GeV: data (points), simulation using JETSET (dashed dotted line), HERWIG (dotted line), ARIADNE (dashed line). The dotted curves show a Gaussian fit to the data. The shaded area indicates the acceptance corrected background subtracted from the data.

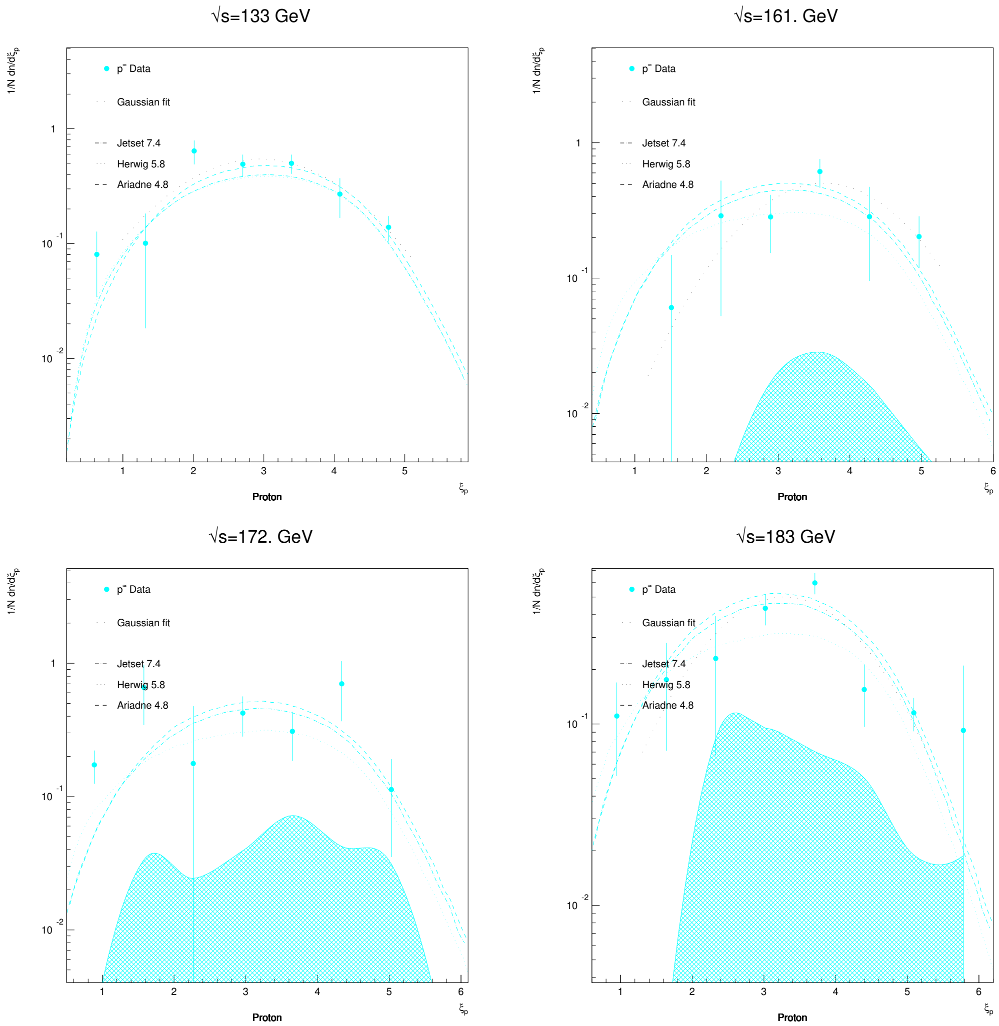

Figure 5.15: ξ_p distributions (fully corrected) for protons and anti-protons at 133 GeV, 161 GeV, 172 GeV and 183 GeV: data (points), simulation using Jetset (dashed dotted line), Herwig (dotted line), Ariadne (dashed line). The dotted curves show a Gaussian fit to the data. The shaded area indicates the acceptance corrected background subtracted from the data.

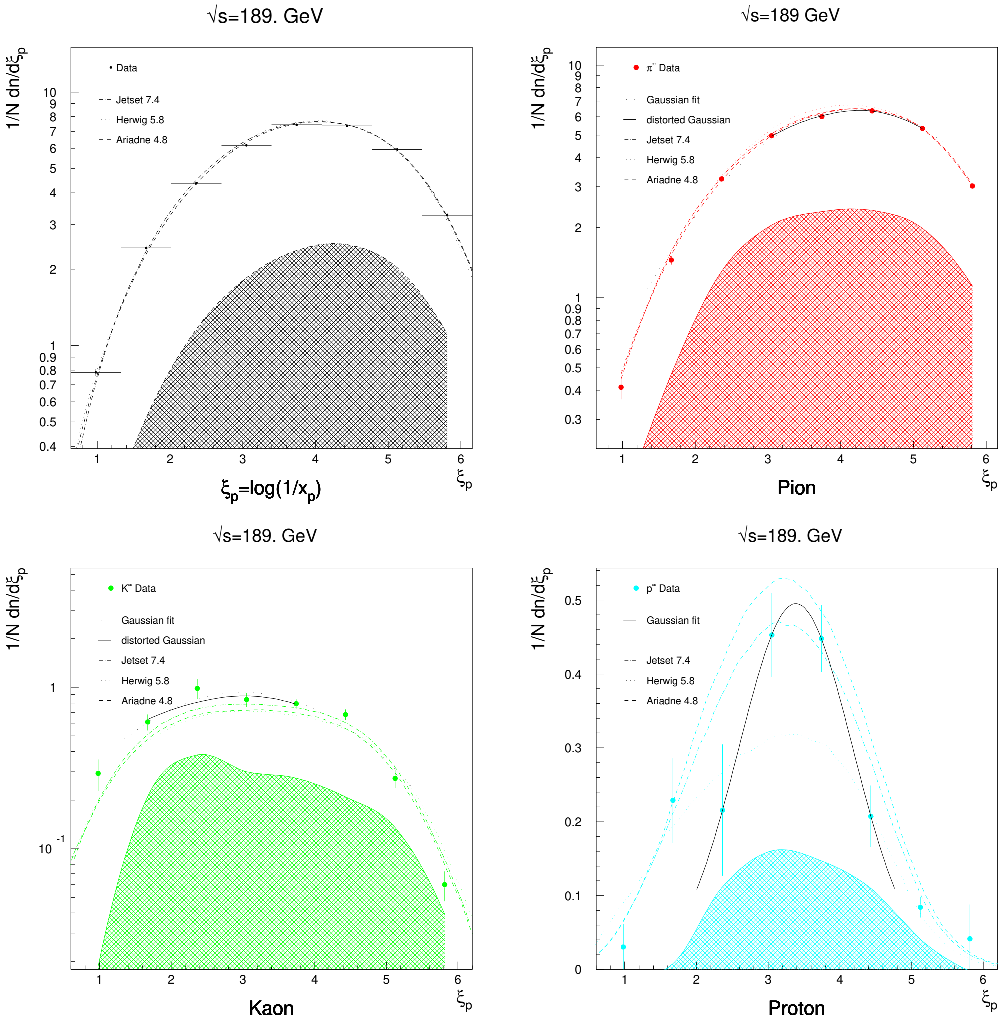

Figure 5.16: ξ_p distributions for (from top left to lower right) charged particles, $\pi^{\pm}$, $K^{\pm}$ and protons from $e^+e^-\rightarrow q\overline{q}$ events at 189 GeV. The shaded area depicts the subtracted background, scaled by the accpetance correction, the dots are DELPHI data (only the statistical errors are shown here) compared to the prediction by JETSET (dashed dotted line), HERWIG (dotted line), ARIADNE (dashed line). The dotted curves show a fit of the peak region of the data to a Gaussian.

Chapter 6

Identified hadrons in $e^+e^-\rightarrow WW$ events

Pair production of W bosons is one of the most interesting and most studied processes at LEP 2. The mass of the W boson, the production cross section and the gauge couplings are measured with previously unmatched precision. From the QCD point of view the production of charged hadrons should be the same as for particles produced at the Z^0 resonance except of a different, lower, energy scale given by the mass of the W. At LEP 2 W's are discerned by their decay.

First, there is the case where both W's decay hadronically. They will do this in 45.57% of the cases with equal probability into a $c\bar{s}$ quark pair or into a $u\bar{d}$ pair. These decays are often referred to as fully hadronic or four jet events. Second, one of them can decay hadronically, and the other into a lepton and neutrino. This will happen in 43.87% of the cases and - assuming lepton universality of the couplings - will happen with a probability of one third into either generation of leptons. These events are often called two jet or semi-leptonic events.

The third process where both W's decay into leptons is of no interest in the context of this study.

It should be mentioned that there is a small cross section for t-channel mediated single W production. These very few events do usually not pass the event selection described later on and their possible contribution is ignored.

The two possible event configurations require a very different event selection and thus have different systematic uncertainties. The analysis of particle production will be presented separately for both of them.

6.1 Identified hadrons from fully hadronic W decays

The events for this channel are exactly those which constituted the main background in the analysis of $q\overline{q}$ event described so far.

6.1.1 Event selection of fully hadronic events

A feed forward neural net improves the separation of $e^+e^- \rightarrow W^+W^- \rightarrow q\overline{q}Q\bar{Q}$ from 2-fermion (mainly $Z^{0*}/\gamma^* \rightarrow q\overline{q}(g)$) and 4-fermion background (mainly $Z^0Z^0 \rightarrow$ anything).

The network is based on the JETNET package, uses the back-propagation algorithm and consists of three layers with 13 input, 7 hidden and one output node. The input variables are different jet and event observables like thrust, oblateness, y_{cut} values and some others more. They are described in detail in [52].

The samples for training and testing the feed forward net consist of PYTHIA simulation and real data. The training is performed with 3500 events from signal and Z^0/γ simulation. Afterwards the network output is calculated for other independent samples of WW Z^0/γ and Z^0Z^0 simulation and all real data as test samples. The selection efficiency and the remaining background are determined from the simulation. The efficiency is found to be $89.0 \pm 0.16(\mathrm{stat})\%$.

6.1.2 Average multiplicity in WW$\rightarrow$ 4 jets

After event selection the analysis proceeds exactly along the same lines as described for the $q\overline{q}$ analysis. An efficiency matrix calibrated to the Z^0 calibration data is used to extract the true particle rates from the tag rates. Again a first result are particle fractions, or equivalently normalised average production rates as shown in Figure 6.1.

The statistical and systematic uncertainties are again calculated using multinomial statistics and by varying the various selection criteria.

Afterwards the momentum spectra are converted into ξ_p space and the final acceptance corrections are performed.

Fully corrected ξ_p-distributions are obtained and afterwards integrated to calculate the multiplicity. The results for the average multiplicity are shown in table 6.1 and they are compared to the predictions from JETSET 7.4 and HERWIG 5.8.

6.2 Identified hadrons from semi-leptonic W decays

Events in which one W decays into lepton plus neutrino and the other one into quarks are characterised by two hadronic jets, one energetic isolated charged lepton, and missing momentum resulting from the neutrino. The main backgrounds to these events are radiative $q\overline{q}$ production and four-fermion final states containing two quarks and two oppositely charged leptons of the same flavour.

6.2.1 Event selection for WW→2 jets $\ell\nu$

Events were selected by requiring seven or more charged particles, with a total energy (charged plus neutral) above $0.2\sqrt{s}$ and a missing momentum larger than $0.1\sqrt{s}$. Events in the $q\bar{q}\gamma$ final state with ISR photons at small polar angles, which would be lost inside the beam pipe, were suppressed by requiring the polar angle of the missing momentum vector to satisfy $|\cos\theta_{miss}| < 0.94$.

Including the missing momentum as an additional massless neutral particle (the candidate neutrino), the particles in the event were forced to 4 jets using the Durham algorithm. The jet for which the fractional jet energy carried by the highest momentum charged particle was greatest was considered as the "lepton jet". The most energetic charged particle in the lepton jet was considered the lepton candidate, and the event was rejected if its momentum was smaller than 10 GeV/c. or greater than 65 GeV/c. The "neutrino jet" was considered the jet clustered around the missing momentum. The event was discarded if the invariant mass of the event (excluding the lepton candidates) was smaller than 20 GeV/c^2 or larger than 110 GeV/c^2.

At this point three alternative topologies were considered:

- Muon sample: when the lepton candidate was tagged as a muon and its isolation angle, with respect to other charged particles above 1 GeV/c, was above 10°, the event was accepted either if the lepton momentum was greater than 20 GeV/c, or if it was greater than 10 GeV/c and the value of the y_{cut} parameter required by the Durham algorithm to force the event from a 3-jet to a 4-jet configuration was greater than 0.003.

- Electron sample: when the lepton candidate had associated electromagnetic energy deposited in the calorimeters larger than 20 GeV, and isolation angle (defined as above) greater than 10 degrees, the event was accepted if the required value of y_{cut} was greater than 0.003.

- Inclusive sample: the events were also accepted if the "lepton" momentum was larger than 20 GeV/c and greater than half of the jet energy, the missing momentum was larger than $0.1\sqrt{s}$, the required value of y_{cut} was greater than 0.003, and no other charged particle above 1 GeV/c existed in the lepton jet.

The purity and the efficiency of the selected data sample from the 189 (183) GeV data were estimated using simulation to be about 88% and 55% (87% and 56%) respectively. The data sample consists of 701 (267) events, where 710 (245) were expected from the simulation. The expected background was subtracted bin by bin from the observed distributions, which were then corrected bin by bin using scaling factors computed from the simulation.

6.2.2 Average multiplicity in WW→ 2 jets $\ell\nu$

After the event selection the analysis proceeds again along the same lines as described in the previous sections. Particle fractions are calculated using the calibrated inverted efficiency matrix. Then the momentum spectra of the particles are converted into ξ_p spectra and the final acceptance correction is performed.

The semi-leptonic sample is very pure. Due to its very clear signature, with the large missing momentum and the highly unbalanced four momentum of the event, it is not likely that Z^0Z^0 or normal $q\overline{q}$ events are selected. The small remaining background is in part due to badly reconstructed events. Because of this the systematic contribution from the uncertainty in the background size is small.

There is however a problem which is unique to this sample. The high momentum lepton is indistinguishable from a pion, or in the case of an original τ lepton, most likely it *is* the pion from the single prong decay. So there is a rather big extra contribution to the high momentum pion bins, which is not there in the calibration sample. If one would simply ignore this, it spoils the unfolding because it leads to an unphysical violation of the unitarity of the fractions. In other words: after unfolding the fractions do not sum up to one any more. These high energy leptons have to be rejected. This is done by rejecting tracks which are isolated in a cone of 10° around their momentum axis. Isolation means that there is no particle with momentum greater than 1 GeV in this cone. This cuts away most of the leptons while it has only a small probability of erroneously rejecting a kaon or proton.

Having done this, the method proceeds as before and after integration of the ξ_p distributions the multiplicities as shown in table 6.1 are obtained.

event type	Particle	$< n >$ (Data)	JETSET 7.4	HERWIG 5.8
WW $\rightarrow q\bar{q}q\bar{q}$	$\pi^{\pm}$	$31.65 \pm 0.48 \pm 0.19$	31.74	31.55
	$K^{\pm}$	$4.38 \pm 0.42 \pm 0.12$	4.05	3.63
	$p(\overline{p})$	$1.82 \pm 0.29 \pm 0.16$	1.89	1.66
WW $\rightarrow q\bar{q}l\nu$	$\pi^{\pm}$	$15.51 \pm 0.38 \pm 0.16$	15.90	16.08
	$K^{\pm}$	$2.23 \pm 0.32 \pm 0.17$	2.02	1.82
	$p(\overline{p})$	$0.94 \pm 0.23 \pm 0.06$	0.95	0.83

Table 6.1: Average multiplicity for $\pi^{\pm}$, $K^{\pm}$ and protons for semi-leptonic and fully hadronic WW events at 189 GeV. In the data the first uncertainty is statistical, the second is systematic.

6.2.3 ξ_p distributions for identified particles at M_W

For comparisons of the data to the data obtained at the Z^0 pole, it is more meaningful to use the ξ_p distributions from W decays and their peak positions when the spectra have been boosted back to the rest frame of the W. The mass of the W boson is the relevant energy scale which enters in the ξ_p variable. The additional momentum which the particle have due to to the boost of their original mother particle is of no interest to the QCD dynamics. One of the most interesting aspects of the studies presented here, the energy evolution of the peak, can of course only be studied using the relevant energy scale.

The details of how to obtain the spectra in the rest frame of the W boson are described in the appendix, section A.2.

Figure 6.2 shows the ξ_p distributions obtained from semi-leptonic W events. As is pointed out in the appendix, the boosting procedure relies on the simulation for the part of the spectrum which was not accessible before the boosting. The boosted distributions themselves do thus contain more information from the simulation than the original un-boosted ξ_p spectra.

Nevertheless this does not affect so much the peak region of the distributions and allows to extract ξ^*reliably. This is done as before using a Gaussian fit to the peak region. The systematic error is calculated by adding in quadrature the following contributions:

1. The variation of the background size
2. The contribution of the invisible region

Particle	ξ^*		
	JETSET	data	fit range
$\pi^{\pm}$	3.66	$3.65 \pm 0.02 \pm 0.24$	[2.7 : 4.5]
$K^{\pm}$	2.70	$2.61 \pm 0.09 \pm 0.33$	[1.10 : 3.86]
$p(\overline{p})$	2.73	$2.86 \pm 0.11 \pm 0.44$	[1.10 : 3.86]

Table 6.2: Values for ξ^* for $\pi^{\pm}$, $K^{\pm}$ and protons from a Gaussian fit in the indicated range. The fit was done on the spectra which have been boosted back in the case of the data. The first uncertainty is statistical the second systematic.

3. The dependence of the peak position on a variation of the values of the bins in the peak region by two standard deviations

4. The difference of the value for the peak to the one obtained by using a fit to the distorted Gaussian, eq. (1.21).

Table 6.2 shows the values of ξ^* in the rest frame of the W boson. Data from semi-leptonic W decays at 189 GeV were used. They are compared to the JETSETprediction. The ξ^* value was obtained by a Gaussian fit in the indicated region. The systematic uncertainties were obtained by varying the the bins in the fit range within two times their statistical uncertainty and by adding the difference between the value as obtained by a distorted and an undistorted Gaussian fit. Within the limited statistics of this sample the data are in good agreement with the generator prediction as well as with the prediction from MLLA eq. (1.25).

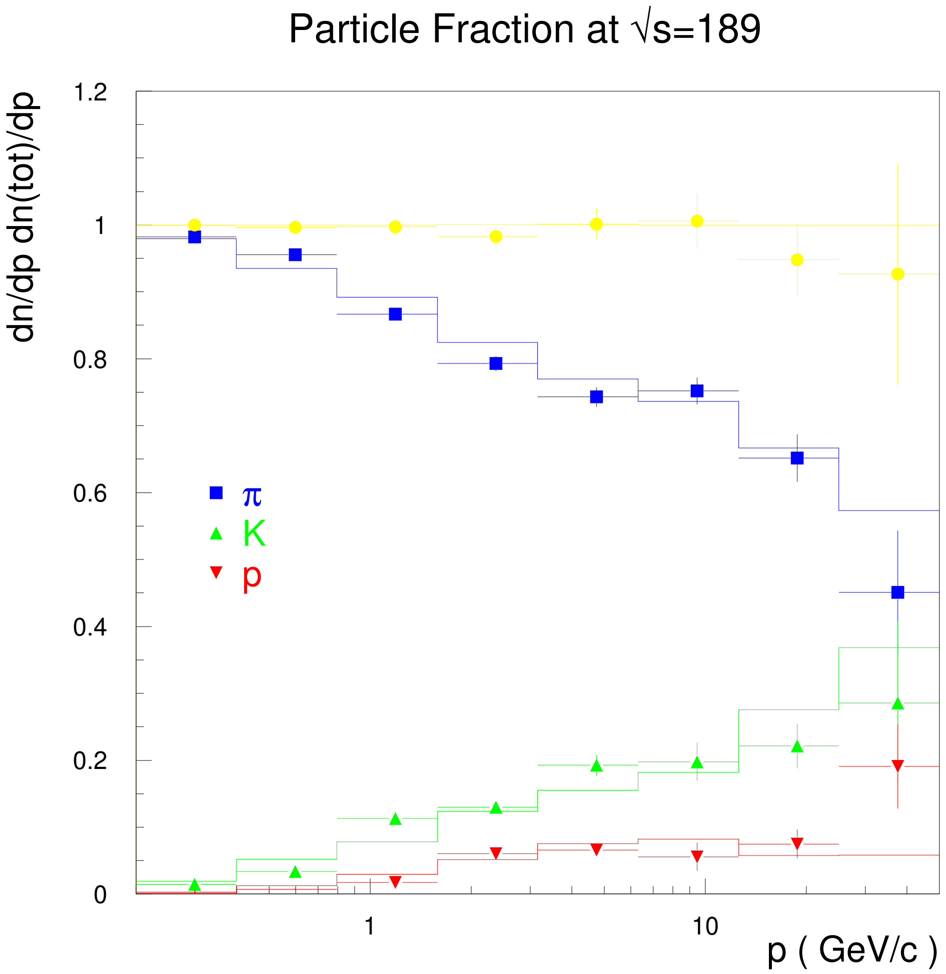

Figure 6.1: Fractions of identified hadrons at 189 GeV from fully hadronic WW decays. Solid line corresponds to Pythia 5.7 with DELPHI tuned JETSET 7.4, including full detector simulation.

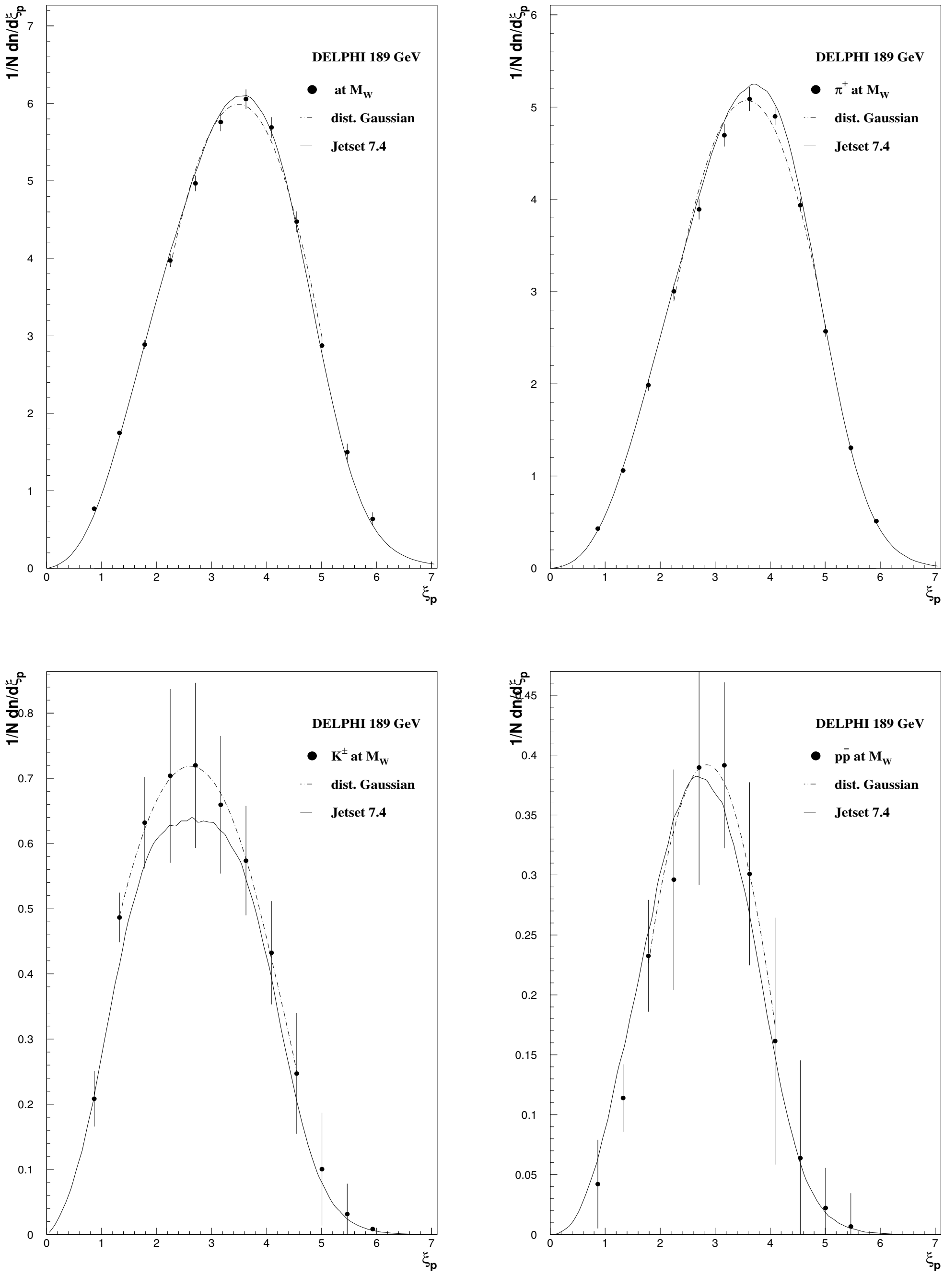

Figure 6.2: ξ_p distribtions (efficiency corrected) for charged particles, pions, kaons and protons in semileptonic WW events at 189 GeV. Data (points) which have been boosted back to the W rest-frame, compared to the prediction from JETSET(solid line). Only the statistical uncertainties are shown. The dashed dotted line shows a fit to eq. (1.21).

Chapter 7

Discussion

From a purely experimental point of view the topic of this work is the study of the production $\pi^{\pm}, \mathrm{K}^{\pm}$ and $\mathrm{p}(\overline{\mathrm{p}})$ in $\mathrm{q}\overline{\mathrm{q}}$ and WW events at LEP 2 centre of mass energies ranging from 130 up to 189 GeV.

The main challenge lies then in the efficient identification of charged hadrons. Since in high energy physics one is usually not at liberty to choose the first experiment one is taking part in, it is very fortunate that I have become member of the DELPHI collaboration. DELPHI is especially well equipped for this kind of study. The RICH detectors are an outstanding tool for particle identification at almost the whole momentum range. As has become clear in the previous chapter the RICH detectors are very complex devices, and many physical effects influence the data. To understand all these effects, judge their relevance and tailor the analysis accordingly has been one of the major parts of this work.

Many parameters of the particle identification have a strong momentum dependence as has been explained earlier. It is therefore natural to study the particle production in terms of momentum spectra. The measured spectra have to be related to the true spectra of particles in the detector. As in any analysis the understanding of the detector necessitates the use of a detailed simulation. In this analysis the simulation enters in two stages.

First the observed rates are unfolded using the efficiency matrix which is constructed from the simulated data. The efficiency matrix simplifies the proper statistical treatment of the problem and the incorporation of the momentum dependencies. The observed rates of $\pi^{\pm}, \mathrm{K}^{\pm}$ and $\mathrm{p}(\overline{\mathrm{p}})$ are of course not statistically independent, first of all due to (trivial) energy-momentum conservation, secondly, and more important due to misidentification which mixes the three species. The matrix allows to disentangle the three types of particles and it allows also the propagation of the correct statistical error, which is trinomial, since three types of particles are in the game. This proper treatment is one of the strong points of this work.

The second way simulation enters is more trivial. There has to be a correction for the inefficiency of the detection of charged particles in general. The angular coverage of DELPHI is not complete and particle below a certain momentum ($\sim$ 200 MeV) can not be reliably identified. These effects are also momentum dependent, it is assumed that the angular distributions of particles are not correlated with the momentum. In this way global correction factors are calculated using simulation.

The simulation of the particle identification can not be perfect. It does not, or only partially, take into account varying efficiencies, geometrical effects, malfunctioning parts of the detectors or the time dependence of detector effects, such as changes in drift velocity, or different pedestals. The matrix has to be calibrated using real data. Usually analyses at LEP 2 are calibrated using the calibration data at the Z^0 pole taken at the beginning of each year. The results can be compared to the precision results obtained at LEP 1, where the statistical accuracy is much higher than would be ever possible at LEP 2. This analysis goes one step further. Since time dependence is very important a data sample is used, which is recorded at the same time as the signal data. Radiative Z^0 are produced in sufficient numbers to estimate the remaining influence of detector effects. After all corrections have been applied figures like Figure A.1 on page 87 demonstrate the very good understanding of the detector achieved in this work.

The unfolded particle fractions are already interesting measurements since they can be directly compared to measurements at different centre-of-mass energies [51, 53].

Since the production of these particles is described by QCD it is most interesting to compare it to the theoretical predictions. This can be done in two ways.

First there are a lot of QCD inspired Monte Carlo programs, which in one way or the other try to implement a physical picture of a hadronic event, as it is predicted by QCD. These models have a number of free parameters which have to be adjusted to the experimental data. All observables studied in this work have also been studied on a sample of 1000000 events generated with the most popular generators for QCD studies at LEP, JETSET, HERWIG and ARIADNE. The tuning of these programs, which has been done by DELPHI at the Z^0 pole is used.

All generators describe the data remarkably well. This can be interpreted as demonstration of the good data description by the models and as an indication of the universality of the perturbative QCD picture, which has been discussed in chapter 1.

Of course these models are *not* QCD. They are QCD spirited. So a real test of QCD has to compare measurements to analytical ab initio calculations. What is behind these calculations and how they are related to observables using Local Parton Hadron Duality is also discussed in chapter 1. For the purposes of comparison with theory, the momentum spectra have to be converted to a different variable, ξ_p. The theory predicts for example the shape of the ξ_p distributions of different hadrons, eq. (1.20), page 10. In principle this could be a very stringent test, but even when using the simplifications of this expression, like the distorted Gaussian eq.(1.21), the very limited statistics at LEP 2 and the need for a rather coarse binning, limit the power of these results. Nevertheless as can be seen in figures 5.13, 5.14 and 5.15, the agreement is quite good.

However, the different energies probed at LEP 2 open up the possibility for an equally interesting test. The evolution of the peak of the ξ_p distribution. This is also a rigorous, non-trivial result from perturbative QCD. Eq. 1.25 has not many free parameters. Using the high precision measurements at the Z^0 pole and some lower energy results, completely fixes the prediction.

It is, in the opinion of the author, an impressive success of perturbative QCD, that this work shows that the measurements spanning over 90 GeV in centre-of-mass energy, are in very good agreement with this prediction, as can be seen if Figure 7.1.

To test universality further it is interesting study also a different electroweak process, which should be the same from the point of view of QCD. LEP 2 offers WW pair production and in this work the detailed decay properties of W bosons into $\pi^{\pm}, \mathrm{K}^{\pm}$ and $\mathrm{p}(\overline{\mathrm{p}})$ are presented for the first time. The ξ_p distributions may be compared to similar measurements at the Z^0 pole, which are nearest in the relevant energy scale. To achieve this comparison the irrelevant boost of the spectra due to the boost of the original W bosons has to be subtracted. A method also based on a matrix has been developed of this thesis which achieves this, as is described in section A.2,on page 88. The peak value of the ξ_p distribution inserted at the correct corresponding energy scale, M_{W} is also in very good agreement with the theoretical expectation.

Summarising the merit of this thesis, it seems fair to say that this work adds to the success of perturbative QCD and it improves, with more detail, our understanding of the decay properties of the W boson.

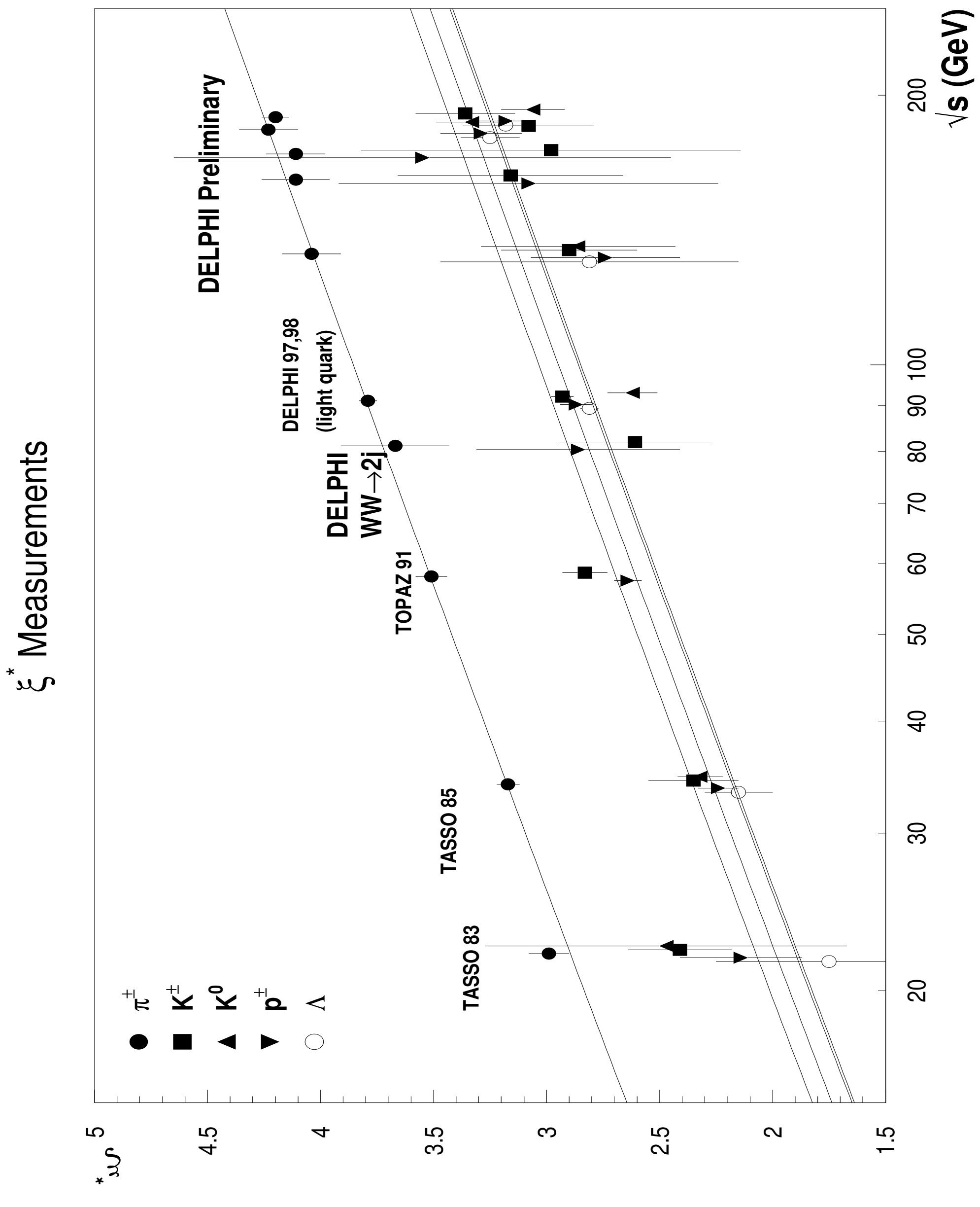

Figure 7.1: Evolution of ξ^* in $e^+e^- \rightarrow q\bar{q}$ with increasing center of mass energy. DELPHI results from this work are compared to previous measurements from DELPHI (ref. [51]) and lower energy experiments (from ref. [21]). The measurement using WW pairs has been added at the corresponding energy scale, M_{W}. The solid line is a fit to eq. (1.25). For better legibility the data points have been shifted from the nominal energy.

Appendix A

Technical aspects

A.1 Calibration of the efficiency matrix using Z^0 data

For a precise control of the detector response it is necessary to calibrate the efficiency matrix. The Z^0 calibration data recorded during each year have been used to tune the matrix described in 5.2 before applying it to high energy data.

This is made possible by the careful studies of the spectra done at the Z^0 pole [51] The previous DELPHI measurement at the Z^0 pole has established that the exclusive particle spectra are well reproduced by the DELPHI tuning of the generators with. Therefore deviations of the rates of tagged particles between data and simulation, exceeding the minimal deviations achieved after tuning, can be interpreted as pure detector effects.

Comparison of the tag rates allows a validation of the efficiency matrix. The method used in this work is different from the one used at the Z^0-pole [51] where the ample statistics collected allowed to use very pure samples of charged particles originating from Λ's and K^0's to measure the efficiency matrix properly.

Unfortunately this is not possible with the limited data samples at LEP 2. The assumption here is that the simulation describes the calibration samples correctly. The matrix is then corrected so that it reproduces the simulated rates, assuming that the correction factors are linear. The discrepancies have been found to be smaller than 4%. This is taken into account when calculating the systematic uncertainties.

As the high energy events are recorded over a long time period, stability of the identification devices becomes a major concern. Variations in the refractive index or the drift velocity in the Riches, may significantly change the performance of the identification. This variations can not be taken into account by the alignment and fixing procedure which are done using the calibration sample at the Z^0 pole which is recorded in 2 weeks at the very beginning of the data taking. To estimate the effect of these variations on the measurement the radiative Z^0's are very well suited, because they are distributed over the whole year like the signal events.

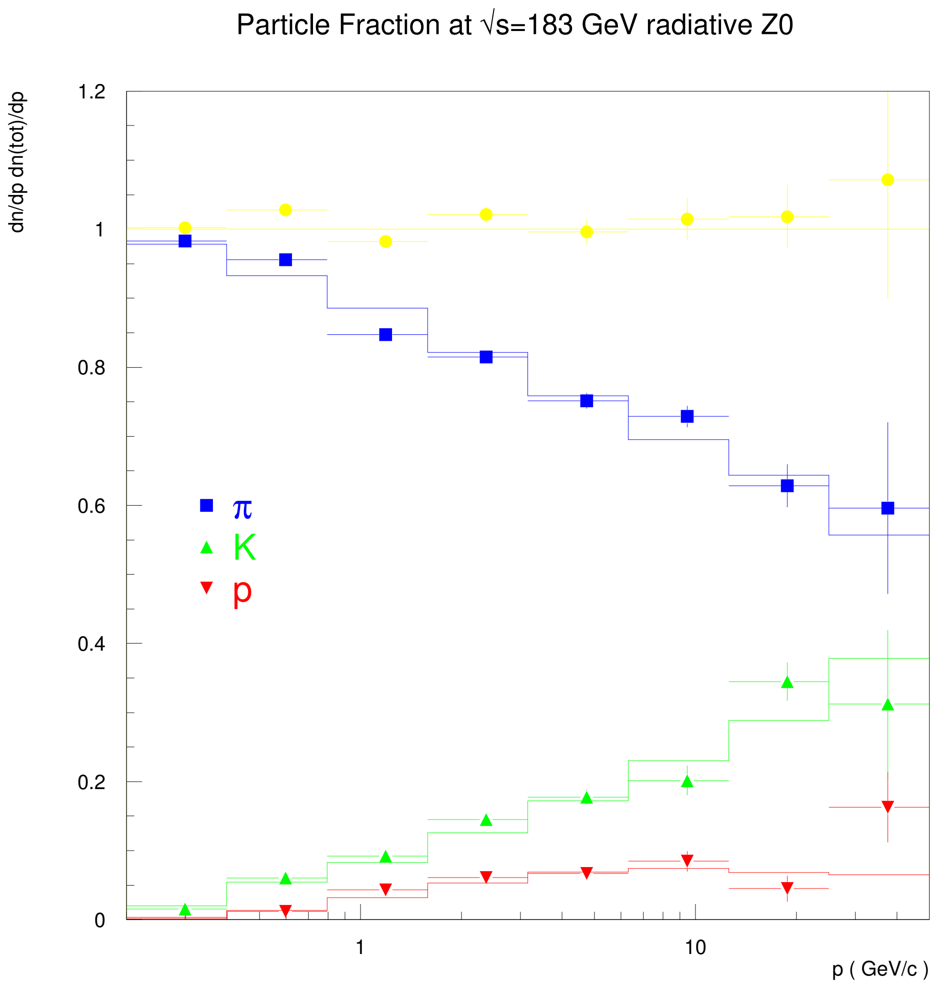

Figure A.1: Fractions of identified particles in radiative Z^0 events from 183 GeV data. The data have been taken under the same conditions as the signal data. The data are in good agreement with the measurements from the Z^0 pole over the full momentum range.

They have been selected in the following way. Events which passed the hadronic preselection were required in addition to contain at least 8 charged tracks, a reconstructed effective centre-of-mass energy below 130 GeV, and a total energy transversal with respect to the thrust axis of more than 30 GeV. Figure A.1 shows the good agreement for differential cross sections (or particle fractions) for this event sample which may be taken as an indication of the stability of the detector during the whole year. From this figure the instabilities can be shown to be at the few percent level.

A.2 Boosting the ξ_p spectrum into the W rest-frame

In the decay of an on-shell W boson the relevant energy scale for the start of the parton cascade is the mass of the W. The fact that the W's from the pair production at LEP are boosted just results in an additional boost which all hadrons from one W get. For a meaningful comparison of the ξ_p spectra from W decays to the spectra from the Z^0 or lower energies, it is therefore necessary to transform them back into the rest-frame of the W. The boost of the W is given by the electro-weak production cross section. The latter follows a relativistic Breit-Wigner distribution,

$$\sigma \propto \frac{s}{\pi} \frac{m_{\mathrm{W}} \Gamma_{\mathrm{W}}}{(s\tau - m_{\mathrm{W}}^2)^2 + m_{\mathrm{W}}^2 \Gamma_{\mathrm{W}}^2} \tag{A.1}$$

which is shown in figure A.2.

It is not very practical to extract the boost of each W produced, for two reasons. First there is an error of a few GeV/c in each event on the reconstructed mass, and in the four quark channel there is the additional problem of the jet assignment; second the unfolding mechanism works on integrated averaged spectra, and not on a event by event basis. Second, and even more important is that the efficiencies of the particle identification are of course functions of the true momenta. The solution chosen for this analysis was to use again a matrix to relate the boosted spectra to the spectra in the rest frame. This matrix can be calculated with high statistics on the generator level, by generating a W, storing its boost and true mass, decaying and fragmenting it, and then boosting the stable hadrons back into the rest frame of the W. Then one stores for each particle species the momentum before and after the boost. With a sufficient number of W this is a good approximation, what is lost, is the angular distribution of the Ws, but these dependencies should be negligible in the fully corrected spectra. Figure A.3

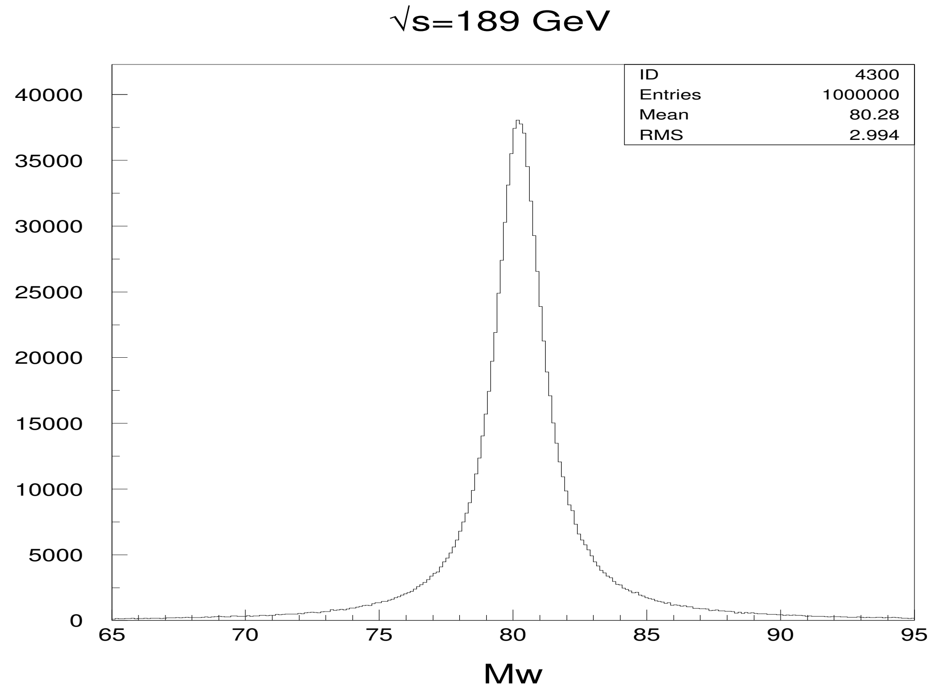

Figure A.2: Distribution of generated values of the W mass from 1000000 events, generated with PYTHIA at 189 GeV.

shows the boost-matrix for W's produced at 189 GeV. The momenta have been rewritten in terms of ξ_p. The energy scale s in $\xi_p = -\ln 2p/s$ is chosen to be 189 GeV for the boosted spectra, and the actually generated M_W for the spectra in the rest frame. The figure shows also that most of the particles are shifted to the right side which corresponds to increasing ξ_p or decreasing momentum.

The whole procedure allows then also to fit the peak of the ξ_p distribution and to interpret it as a measurement performed at $\sqrt{s} = M_\mathrm{W}$.

Unfortunately the matrix transfers part of the non-measurable spectrum, of either too high or too low momentum to the measured part of the spectrum. This does not affect the position of the peak, but it would introduce additional systematic uncertainties for the multiplicity measurement. So the integration and the estimation of the systematic uncertainties is done with the ξ_p spectra in the laboratory frame.

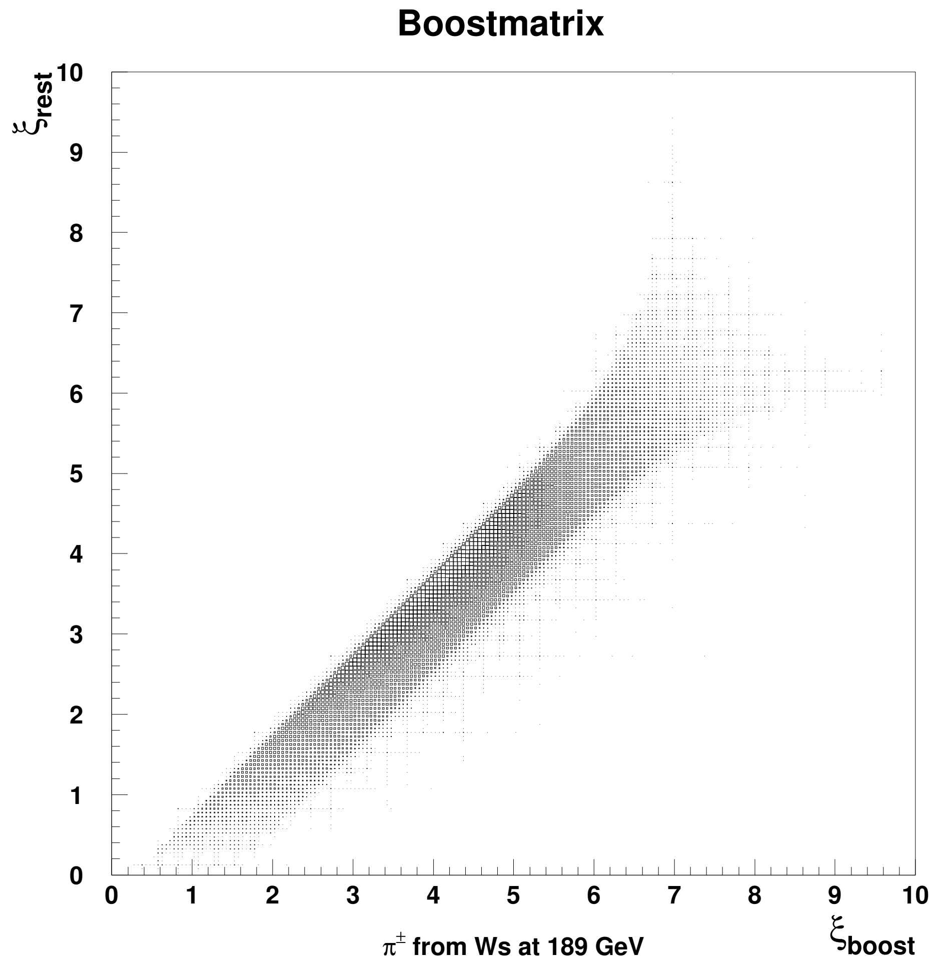

Figure A.3: Boostmatrix at 189 GeVfor charged pions from W decays. Spectra in the laboratory frame (x-axis) versus spectra in the rest frame of the W (y-axis). This figure has been produced using 1000000 generated W events with PYTHIA and JETSET. See also the explanations in the text.

Bibliography

[1] N. Neufeld, Identified Particles at LEP II, in *Proceedings of the Thirteenth Lake Louise Winter Institute, Quantum Chromodynamics*, edited by A. Astbury, B. A. Campbell, F. C. Khanna, J. L. Pinfold, and M. Vetterli, pp. 458–465, World Scientific, 1999.

[2] N. Neufeld, Studies of Identified Hadrons in $q\overline{q}$ events at LEPI, in WWand $q\overline{q}$ events at LEPII and search for stable and long-lived heavy charged particles , in *Proceedings of the 3rd International Workshop on RICH Detectors, RICH98*, edited by A. Breskin *et al.*, 1999, to appear in Nucl. Instr. Meth. **A**.

[3] DELPHI Coll., P. Abreu *et al.*, Charged and Identified Particles from the hadronic decay of W bosons and in $e^+e^- \to q\bar{q}$ from 130 to 189 GeV, 1999.

[4] DELPHI Coll., P. Abreu *et al.*, Charged and Identified Particles from the hadronic decay of W bosons and in $e^+e^- \to q\bar{q}$ from 130 to 189 GeV, Paper submitted to HEP'99, Tampere, # 229 PA 1,6, Pl 1,6, 1999.

[5] M. L. Mangano, Introduction to QCD, http://home.cern.ch /mlm/ talks/ cern98.ps.gz, 1998, Lectures given at the 1998 CERN School of High Energy Physics, St. Andrews, United Kingdom.

[6] R. K. Ellis, W. J. Stirling, and B. R. Webber, *QCD and Collider Physics* (Cambrige University Press, 1996).

[7] Y. Dokshitzer, A. Müller, V. Khoze, and S. Troyan, *Basics of Perturbative QCD* (Editons Frontieres, 1991).

[8] V. A. Khoze, S. Lupia, and W. Ochs, Eur. Phys. J. **C5**, 77 (1998).

[9] AMY Coll., H. Zheng *et al.*, Phys. Rev. **D42**, 737 (1990).

[10] HRS Coll., M. Derrick *et al.*, Phys. Rev. **D34**, 3304 (1987).

[11] TASSO Coll., W. Braunschweig *et al.*, Z. Phys. **45**, 193 (1989).

[12] MARK II Coll., Phys. Rev. Lett. **54**, 2580 (1985).

[13] JADE Coll., Z. Phys. **C20**, 187 (1983).

[14] PLUTO Coll., Phys. Lett. **95B**, 313 (1980).

[15] Y. I. Azimov, Y. L. Dokshitzer, V. A. Khoze, and S. I. Troyan, Z. Phys. **C27**, 65 (1985).

[16] Y. I. Azimov, Y. L. Dokshitzer, V. A. Khoze, and S. I. Troyan, Z. Phys. **C31**, 213 (1986).

[17] V. A. Khoze and W. Ochs, Int. J. Mod. Phys. **A 12**, 2949 (1997).

[18] C. P. Fong and B. R. Webber, Phys. Lett. **B229** (1989).

[19] Y. L. Dokshitzer, V. A. Khoze, C. P. Fong, and B. R. Webber, Phys. Lett. **B273**, 319 (1991).

[20] Y. L. Dokshitzer, V. A. Khoze, and S. Troyan, Int. J. Mod. Phys. **A7**, 1875 (1992).

[21] N. Brümmer, Z. Phys. **C66** (1995).

[22] I. G. Knowles and G. D. Lafferty, J. Phys. G: Nucl. Part. Phys. **23**, 731 (1997).

[23] ALEPH Coll., R. Barate *et al.*, Phys. Rept. **294**, 1 (1998).

[24] R. D. Field and R. P. Feynman, Phys. Rev. **D15**, 2590 (1977).

[25] X. Artru and G. Mennessier, Nucl. Phys. **B70**, 93 (1974).

[26] M. G. Bowler, Z. Phys. **C11**, 169 (1981).

[27] B. Andersson, G. Gustafson, and B. Söderberg, ZPH **C20**, 317 (1983).

[28] B. Andersson, G. Gustafson, and B. Söderberg, Nucl. Phys. **B264**, 29 (1986).

[29] T. Sjöstrand, Computer Physics Commun. **82** (1994).

[30] L. Lönnblad, Computer Physics Commun. **71** (1992).

[31] G. Marchesini *et al.*, Computer Physics Commun. **67** (1992).

[32] L. D. Landau and E. M. Lifschitz, *Elektrodynamik der Kontinua* Lehrbuch der Theoretischen Physik (Akademie Verlag, Berlin, 1990), chap. XIV, p. 489.

[33] W. Blum and L. Rolandi, *Particle Detection with Drift Chambers* (Springer, 1994).

[34] W. W. M. Allison and J. H. Cobb, Ann. Rev. Nucl. Part. Sci. **30**, 253 (1980).

[35] H. A. Bethe, Ann. Phys. **5**, 325 (1930).

[36] E. Fermi, Phys. Rev. **57**, 485.

[37] U. Fano, Ann. Rev. Nucl. Part. Sci. **13**, 1 (1963).

[38] C. Caso *et al.*, Eur. Phys. J. **C3**, 1 (1998).

[39] E. J. Williams, Proc. R. Soc. **Ser. A 125**, 420 (1929).

[40] H. A. Bichsel and R. P. Saxon, Phys. Rev. **A 11**, 1286 (1975).

[41] L. D. Landau, J. Phys. USSR **8**, 201 (1944).

[42] M. Regler and R. Frühwirth, editors, *Data analysis techniques for high-energy physics experiments* , Third ed. (Cambridge University Press), forthcoming.

[43] DELPHI Coll., P. Abreu *et al.*, Nucl. Instr. Methods **A378**, 57 (1996).

[44] E. Albrecht *et al.*, Operation, Optimisation and Performance of the DELPHI RICH Detectors, in *Proceedings of the 3rd International Workshop on RICH Detectors, RICH98*, edited by A. Breskin *et al.*, Elsevier, 1999.

[45] G. Borisov and C. Mariotti, Tuning of the Track Impact Parameters, DELPHI Internal note, 1997, DELPHI 97-95 PHYS 717.

[46] R. Forty and O. Schneider, LHCb Internal Note, 1998.

[47] M. Battaglia and P. M. Kluit, Particle Identification using the DELPHI RICH Detectors, in *Proceedings of the 3rd International Workshop on RICH Detectors, RICH98*, 1999.

[48] DELPHI Coll., P. Abreu *et al.*, Z. Phys. **C77**, 11 (1996).

[49] DELPHI Coll., P. Abreu *et al.*, Phys. Lett. **B372**, 172 (1996).

[50] S. Bethke *et al.*, Nucl. Phys. **B370**, 310 (1992).

[51] DELPHI Coll., P. Abreu *et al.*, Eur. Phys. J. **C5**, 585 (1998).

[52] P. Buschmann *et al.*, Measurement of the W-pair Production Cross-section at $\sqrt{s} = 183$ GeV, 1998, DELPHI 98-20.

[53] SLD Coll., K. Abe *et al.*, Phys. Rev. **D59** (1999).

Curriculum Vitae

Niko Neufeld

Ad personam

Name	Dipl. Ing. Niko Neufeld
Geboren	14. Februar 1972
Geburtsort	Graz, Steiermark
Vater	Dr. med. Fritz Neufeld
Mutter	Vida Neufeld
Familienstand	verheiratet
Ehefrau	Dr. iur. Inge Nora Neufeld

Ausbildung

1978-82	Volksschule, Klagenfurt
1982-90	Ingeborg Bachmann Gymnasium, Klagenfurt
Juni 1990	Matura, mit gutem Erfolg
1990-1995	Studium der Technischen Physik, TU-Wien
1994-1995	Diplomarbeit: „Tests von Siliziumstreifendetektoren für den Very Forward Tracker in DELPHI“
Jänner 1996	Graduierung zum Diplom Ingenieur
1997-1999	Doktoratsstudium der Technischen Physik, TU-Wien

Bisherige Tätigkeiten

1994-96	Tutor am Institut für Computersprachen, TU-Wien
1994-96	Mitarbeit am Institut für Hochenergiephysik, Österreichische Akadmie der Wissenschaften
1997-99	Doktorat am CERN, Genf durch Stipendium des Wissenschaftsministeriums
seit 1. August 1999	Mitarbeiter am Institut für Hochenergiephysik der ÖAW